Titre: Title:	Fundamentals and Applications of On-Chip Interferometers Based on Deep-Etched Silicon-Air Multilayer Reflectors
Auteur: Author:	Raphaël St-Gelais
Date:	2012
Type:	Mémoire ou thèse / Dissertation or Thesis
Référence: Citation:	St-Gelais, R. (2012). Fundamentals and Applications of On-Chip Interferometers Based on Deep-Etched Silicon-Air Multilayer Reflectors [Thèse de doctorat, École Polytechnique de Montréal]. PolyPublie. https://publications.polymtl.ca/1024/

URL de PolyPublie: PolyPublie URL:	https://publications.polymtl.ca/1024/
Directeurs de recherche: Advisors:	Yves-Alain Peter
Programme: Program:	Génie physique

UNIVERSITÉ DE MONTRÉAL

FUNDAMENTALS AND APPLICATIONS OF ON-CHIP INTERFEROMETERS BASED ON DEEP-ETCHED SILICON-AIR MULTILAYER REFLECTORS

RAPHAËL ST-GELAIS

DÉPARTEMENT DE GÉNIE PHYSIQUE

ÉCOLE POLYTECHNIQUE DE MONTRÉAL

THÈSE PRÉSENTÉE EN VUE DE L'OBTENTION

DU DIPLÔME DE PHILOSOPHIAE DOCTOR

(GÉNIE PHYSIQUE)

DÉCEMBRE 2012

UNIVERSITÉ DE MONTRÉAL

ÉCOLE POLYTECHNIQUE DE MONTRÉAL

Cette thèse intitulée:

FUNDAMENTALS AND APPLICATIONS OF ON-CHIP INTERFEROMETERS BASED ON DEEP-ETCHED SILICON-AIR MULTILAYER REFLECTORS

présentée par : ST-GELAIS Raphaël

en vue de l'obtention du diplôme de : Philosophiae Doctor

a été dûment acceptée par le jury d'examen constitué de :

M. GODBOUT Nicolas, Ph. D., président

M. PETER Yves-Alain, Dr. Sc., membre et directeur de recherche

M. FRANCOEUR Sébastien, Ph. D., membre

Mme LAROCHELLE Sophie, Ph. D., membre

DEDICACE

À mes parents, à Catherine et à Maude

To my parents, and to Catherine and Maude

REMERCIEMENTS

J'aimerais avant tout remercier mon directeur de recherche, Yves-Alain Peter, pour m'avoir généreusement accompagné tout au long de ce travail, me fournissant sans compter disponibilités, moyens techniques et financiers, ainsi qu'opportunités d'assistance à divers colloques et rendez-vous scientifiques. J'estime qu'il a parfaitement su canaliser mes énergies en m'accordant un équilibre idéal entre liberté, supervision, et responsabilités diverses au sein du laboratoire. Je souhaite par le fait même remercier tous les membres passés et présents du laboratoire de microphotonique, desquels j'aurai énormément appris et que j'aurai eu le plus grand plaisir à côtoyer. Je remercie plus spécifiquement mes collègues Jonathan Masson, Alexandre Poulin et Antoine Leblanc-Hotte, avec qui j'ai collaboré plus étroitement, et qui ont grandement contribué à l'obtention et à la mise en valeur des résultats présentés dans cette thèse. Je souhaite également souligner la contribution de tous les stagiaires ayant travaillé sous ma supervision. Patrick Daoust, Thomas Kerrien et Hubert Camirand n'ont ménagé aucun effort et ont tous contribué significativement à l'avancement de nos travaux. Je remercie d'autre part mes collègues du département de chimie de l'université Queen's, avec qui nos travaux portant sur les capteurs de gaz ont été menés. Cette collaboration interdisciplinaire à certainement été l'un des moments les plus instructifs et les plus enrichissants de mes études doctorales.

J'aimerais remercier également le département de génie physique, au sein duquel j'aurai passé près de dix ans, et qui a su me fournir l'environnement idéal à mon épanouissement personnel et scientifique. Je suis particulièrement reconnaissant envers le personnel du laboratoire de microfabrication, endroit où la totalité des dispositifs présentés dans cette thèse ont été fabriqués. Il est primordial de reconnaître que, comme chercheurs, nous pouvons aller aussi loin que ce que nos moyens techniques nous permettent. En ce sens, j'estime que le laboratoire de microfabrication travaille chaque jour à repousser la limite des possibilités offertes à ses usagés.

Je remercie également les membres de mon jury de thèse qui ont généreusement accepté d'évaluer ce travail. J'ai la plus haute estime pour les compétences scientifiques de chacun d'entre eux et je suis donc très reconnaissant de l'apport qu'ils auront à ce travail.

Je remercie finalement les organismes subventionnaires sans qui ce travail n'aurait été possible, en particulier le conseil de recherche et sciences naturelles et en génie du Canada (CRSNG), qui a fourni l'essentiel du financement de ce projet de recherche, en plus de m'octroyer une généreuse bourse doctorale. Je souhaite souligner par le fait même le travail de l'équipe d'Univalor qui, via ses démarches de valorisation de nos technologies, a organisé au fil des ans plusieurs rencontres des plus intéressantes et des plus instructives avec nombre d'industries d'importance.

ACKNOWLEDGEMENTS

I would first like to thank my advisor, Yves-Alain Peter, for generously accompanying me throughout this work, and for providing me countless availabilities, technical and financial means, and opportunities of assistance to various conferences and scientific meetings. I consider that he was perfectly able to channel my energies by providing be the ideal combination of liberty, supervision, and responsibilities within the laboratory. I thereby thank all past and present members of the microphotonics laboratory, from whom I have learned so much and with whom I had so much fun. I specifically thank my colleagues Jonathan Masson, Alexandre Poulin and Antoine Leblanc-Hotte, with whom I worked more closely, and that significantly contributed to the achievements presented in this thesis. I also wish to acknowledge the contributions of all the interns that worked under my supervision. Patrick Daoust, Hubert Camirand and Thomas Kerrien spared no efforts and greatly contributed to the progress of our work. I also thank my colleagues from the Department of Chemistry at Queen's University, with whom the work on gas sensors was carried. This interdisciplinary collaboration was certainly one of the most informative and rewarding of my doctoral studies.

I also thank the Department of Engineering Physics, within which I have spent nearly ten years, and that provided me the ideal environment for my personal and scientific development. I am particularly grateful to the laboratory of microfabrication, where all the devices presented in this thesis were fabricated. We have to recognize, as researchers, that we can go as far as allowed by our technical means. In that sense, I believe that the microfabrication laboratory works every day to push the limits of the possibilities offered to its users.

I also thank the members of my thesis committee, whom generously agreed to evaluate this work. I have the highest consideration for their scientific expertise I am very grateful for the contribution they will have to this work.

I finally thank the funding agencies without which this work would not have been possible, in particular the Natural Sciences and Engineering Research Council of Canada (NSERC), who provided most of the funding for this research project, in addition to grant me a generous doctoral scholarship. I also wish to acknowledge the work of the Univalor team which, through their technology transfer efforts, organized highly informative and productive meetings with several important industries.

RÉSUMÉ

Les technologies de gravure profonde de silicium par plasma peuvent être utilisées pour la fabrication de miroirs verticaux à alternance de couches de silicium et d'air. Comparativement aux miroirs hors-plan fabriquées par déposition de couches minces, ces miroirs verticaux peuvent être intégrés, de façon simple et monolithique, à une importante variété de dispositifs tels que des tranchées pour l'alignement passif de fibres optiques, des systèmes microfluidiques, des guides d'ondes et des microsystèmes d'actionnement électromécaniques (MEMS). Par contre, tous les dispositifs rapportés à ce jour se sont montrés affectés par d'importantes pertes d'insertion (> 10 dB) lesquelles se sont traduites, dans la majorité des cas, par de faibles capacités de confinement de la lumière (ex: faibles finesses dans le cas d'interféromètres Fabry-Pérot). Le premier objectif de ce travail est donc d'identifier les sources de pertes et les limites technologiques affectant les interféromètres à miroirs multicouches verticaux. Des modèles théoriques permettant la prédiction de pertes—dues à la divergence angulaire du faisceau Gaussien incident, à la rugosité de surface aux interfaces silicium-air, à la verticalité imparfaite des profils de gravure et aux erreurs d'alignement entre les fibres optiques de couplage—sont fournis. Il est démontré que les trois premières de ces quatre sources de pertes sont généralement significatives. Par contre, pour ce qui est des dispositifs présentés dans cette thèse, il est démontré que l'erreur sur la verticalité des profils de gravures (~ 0.04°) est négligeable comparativement aux pertes causées par la rugosité de surface (30 nm RMS) et par la divergence du faisceau Gaussien incident. Il est finalement démontré que la quatrième source de perte (erreur d'alignement entre fibres optiques) peut être négligée dans pratiquement tous les cas. Puisque ces modèles correspondent remarquablement bien à nos résultats expérimentaux, nous sommes en mesure d'établir des limites claires quant aux possibilités des interféromètres à multicouches silicium-air fabriqués par gravure profonde. À l'intérieur de ces limites, trois nouveaux dispositifs—pour des applications potentielles comme capteurs biomédicaux, capteurs chimiques ou comme composants pour réseaux de télécommunication par fibre optique—sont proposés.

Premièrement, un interféromètre Fabry-Pérot est intégré à un réseau microfluidique de silicium et est utilisé pour mesurer l'indice de réfraction de liquides. La sensibilité à l'indice de réfraction obtenue (907 nm/RIU) est considérablement élevée et, fait important, est indépendante

des pertes d'insertion subies à l'intérieur de l'interféromètre. Une résolution parmi les plus élevées rapportées à ce jour (pour une mesure volumétrique d'indice à l'intérieur d'un réseau microfluidique) est conséquemment obtenue (1.7×10^{-5} RIU), malgré des pertes d'insertion élevées (~ 25 dB) et une faible finesse (< 10). Le volume de mesure de ce capteur (~ pL) est similaire à celui de cellules vivantes individuelles. Puisque ce capteur permet également une grande flexibilité lors de la conception du système microfluidique intégré, une de ses applications principales attendues est la caractérisation de cellules individuelles en flux, sur puce.

Deuxièmement, des interféromètres de Fabry-Pérot, similaires à ceux utilisés comme capteurs d'indice de réfraction, sont fonctionnalisés par des polymères à base de PDMS (polydiméthylsiloxane) et sont utilisés comme détecteurs de composés organiques volatiles (VOCs). Dans ce cas, suite à l'absorption de VOCs, les polymères se dilatent et déforment l'interféromètre, ce qui constitue le mécanisme de détection principal. Des variations d'indice de réfraction à l'intérieur des polymères, suite à l'absorption de VOCs, contribuent également à la sensibilité mais à une échelle beaucoup moins importante (10 fois moindre que la réponse due aux déformations mécaniques). Une limite de détection de 1.6 ppm est atteinte lors de la détection de méta-xylène en phase gazeuse à l'aide d'un interféromètre fonctionnalisé par un polymère de phényle-PDMS. Cette limite de détection est similaire à celles atteintes à l'aide d'autres capteurs micromécaniques utilisés au sein de systèmes commerciaux d'olfaction artificielle. Notre capteur—étant compatible avec une éventuelle production de masse, simple à fabriquer (deux étapes de photolithographie conventionnelles), et simple à encapsuler (tranchées d'alignement passif pour fibres optiques)—pourrait donc potentiellement rivaliser avec ces technologies. Un de ses principaux avantages compétitifs serait la possibilité d'interroger notre capteur à distance uniquement par fibre optique, alors que la majorité des autres technologies requièrent une alimentation électrique locale pour chaque capteur.

Finalement, des interféromètres de Gires-Tournois (GTIs) ont été, pour la première fois, intégrés à un guide d'onde dans une configuration planaire sur puce. Ces interféromètres présentent des pertes d'insertion inférieure à 2 dB aux longueurs d'ondes hors résonance, ce qui constitue une amélioration considérable par rapport aux pertes d'insertion typiques des interféromètres de Fabry-Pérot fabriqués par gravure verticale (> 10 dB). Aux longueurs d'ondes de résonance, par contre, les pertes d'insertion demeurent élevées (10 - 15 dB). Ces pertes sont causées par une interaction toujours trop importante de la lumière avec la rugosité de surface

affectant les miroirs multicouches. Les interféromètres proposés pourraient conséquemment être utilisés au sein de réseaux de télécommunication par fibre optique, mais seulement à l'intérieur de dispositifs, tels que les entrelaceurs ("interleavers") Michelson-GTI, exploitant principalement la partie hors résonance de leur spectre. Dans ce cas particulier, la configuration planaire des dispositifs proposés pourrait s'avérer utile comparativement aux précédents dispositifs hors plan sur puce. Par exemple, cette configuration planaire permet la conception d'interféromètres de longueur supérieure à 800 μm. De telles longueurs sont nécessaires à l'obtention d'intervalles spectrales libres (FSR) correspondant aux espacements intercanaux de 25 et 50 GHz des réseaux de télécommunications optiques multiplexés en longueur d'onde (DWDM). Les dispositifs hors plan sur puce sont généralement limités par l'épaisseur du substrat de silicium (500 - 600 μm) et ne permettent donc pas de longueurs supérieures à 800 μm. Des calculs démontrent que des entrelaceurs de Michelson-GTI basés sur les dispositifs rapportés pourraient permettre des pertes d'insertion inférieures à 2 dB et une isolation intercanal de l'ordre de 20 dB.

ABSTRACT

Deep reactive ion etching (DRIE) of silicon can be used to fabricate vertical (i.e. in-plane) silicon-air multilayer mirrors. In comparison with out-of-plane reflectors fabricated by thin film deposition, in-plane multilayer assemblies can be monolithically integrated with a variety of useful structures such as passive optical fiber alignment grooves, microfluidic systems, waveguides, and microelectromechanical (MEMS) actuators. However, all previously reported devices suffered from high insertion losses (> 10 dB) which translated, in most cases, in weak light confinement abilities (e.g. low finesses in the case of Fabry-Perot cavities). The first objective of this work is therefore to investigate the sources of loss and the technological limitations that affect interferometers based on deep-etched multilayer reflectors. Theoretical models for the prediction of losses—due to Gaussian beam divergence, surface roughness at silicon-air material interfaces, imperfect verticality of the etch profiles, and misalignment between input and output coupling optical fibers—are provided. Of these four loss mechanisms, the first three are demonstrated to be generally significant. For the devices presented in the current thesis, however, verticality deviation of the etch profiles (etch angle error ~ 0.04°) is found to be negligible compared with the measured contributions of surface roughness (30 nm RMS) and Gaussian beam divergence. The fourth loss mechanism (fiber misalignment) is found to be essentially negligible in all cases. These theoretical models are demonstrated to correspond remarkably well with our experimental results, such that we are able to state clear boundaries on the possibilities and limitations of interferometers based on deep-etched silicon-air multilayer reflectors. Within these boundaries, three new devices—with potential applications in biomedical sensing, chemical sensing, and optical fiber telecommunications—are investigated.

Firstly, a deep-etched Fabry-Perot interferometer is monolithically integrated with a silicon microfluidic system and is used to measure the refractive index of homogenous liquids. The refractive index sensitivity of this interferometer (907 nm/RIU) is found to be considerably high and, interestingly, to be independent of insertion losses. A refractive index resolution among the highest reported, for volumetric sensing in microfluidic systems, is consequently achieved (1.7×10^{-5} RIU), even if high insertion losses (~ 25 dB) and low resonance finesse (< 10) affect the interferometer. This sensor performs measurements in volumes (~ pL) similar to those of single living cells, and allows great flexibility in the design of monolithically integrated

microfluidic systems. One of its main expected applications is consequently in-flow characterization of cell populations on-chip.

Secondly, Fabry-Perot interferometers, similar to those used as refractive index sensors, are functionalized with polydimethylsiloxane (PDMS) based polymers and are used to detect two different volatile organic compounds (VOCs), i.e. m-xylene and cyclohexane. In this case, mechanical deformation of the interferometers, induced by polymer swelling upon VOCs absorption, is found to be the main sensing mechanism. Refractive index variations inside the polymers also contribute to the sensitivity, but more modestly, yielding a 10 times lower sensitivity than mechanical deformations. A 1.6 ppm resolution is reached when detecting m-xylene vapor using phenyl-doped PDMS as the absorbent polymer. This limit of detection is similar to what was achieved with other micromechanical sensors that currently find applications in artificial olfaction systems. Our proposed sensor—being mass producible, simple to fabricate (two conventional photolithography steps), and simple to package (integrated optical alignment features)—could therefore potentially compete with these technologies. One of its main competitive advantages would be passive remote interrogation using only conventional optical fibers, while other technologies usually require on-site electrical power supply for each sensor head.

Finally, Gires-Tournois interferometers (GTIs) are, for the first time, implemented in an in-plane waveguided configuration. These interferometers reach insertion losses below 2 dB at off-resonance wavelengths, which is significantly better, for example, than the typical insertion losses achieved with deep-etched Fabry-Perot filters (> 10 dB). At resonance wavelengths, however, insertion losses remain high (10 - 15 dB) due to a still too strong interaction of light with surface roughness in the cavity back mirror. The proposed Gires-Tournois could therefore find applications in optical fiber telecommunications but only in devices, such as Michelson-GTI interleavers, that exploit primarily the off-resonance part of the GTI spectra. In this particular case, the proposed in-plane configuration could be advantageous compared with out-of-plane designs. For example, in-plane implementation allows interferometer lengths greater than 800 μm, which are required for free spectral ranges that match the 25 or 50 GHz channel spacing of dense wavelength multiplexed (DWDM) networks. Such lengths are not typically achievable using out-of-plane devices that are limited by their silicon substrate thickness (~ 500 - 600 μm).

Calculations show that Michelson-GTI interleavers based on the reported GTIs could yield insertion losses below 2 dB and channel isolation in the order of 20 dB.

TABLE OF CONTENTS

LIST OF TABLES

LIST OF FIGURES

LIST OF ACRONYMS AND SYMBOLS

B	Bulk modulus
BPM	Beam propagation method
BTEX	Benzene, toluene, ethylbenzene, xylene
c	Speed of light in vacuum
CCP	Capacitively coupled plasma
CY	Cyclohexane
DWDM	Dense wavelength division multiplexing
E	Electric field of light
$\tilde{E}$	Fourier transformed electric field of light (k_t space)
FPI	Fabry-Perot interferometer
FSR	Free spectral range
GD	Group delay
GDD	Group delay dispersion
GTI	Gires-Tournois interferometer
HF	Hydrofluoric acid
IAD	Ion angular distribution
IF	Image field
$K_{p\text{-}a}$	Partitioning coefficient
k_t	Transverse wave vector magnitude
L	Distance between two mirrors of an interferometer
LC	Liquid chromatography
MEMS	Microelectromechanical system
MGTI	Michelson-Gires-Tournois interferometer

m_{Si}; m_{Air}; m_{Gap}	Integer layer order for silicon, air and gap layers in deep-etched interferometers
n	Refractive index
n_{eff}	Waveguide effective index
n_g	Group index
NA	Numerical aperture
P	Spatial period of a multilayer reflector
PDL	Polarization dependant losses
PDMS	Polydimethylsiloxane
PDPS	Polydiphenylsiloxane
PMD	Polarization mode dispersion
QCM	Quartz crystal microbalance
r	Amplitude reflection coefficient
R	Intensity reflection coefficient
RF	Radio frequency
RI	Refractive index
RIU	Refractive index unit
RMS	Root mean square
RPM	Rotation per minute
SAW	Surface acoustic wave
SEM	Scanning electron microscope
SPR	Surface plasmon resonance
std	Standard deviation
t	Amplitude transmission coefficient
T	Intensity transmission coefficient

T_m	Surface roughness harmonics
TOL	Toluene
V	Volume
VOC	Volatile organic compound
XYL	Xylene
δ	Solubility parameter
ϕ	Phase of light
ϕ_a	Volume fraction of analyte in an absorbent polymer
$\mathfrak{F}$	Finesse
Γ_ϕ	Resonance wavelength sensitivity to an absorbed volume fraction of analyte (ϕ_a)
φ	Etch angle error
λ	Wavelength of light
λ_0	Wavelength of light in vacuum
λ_c	Central wavelength of operation (e.g. wavelength of peak reflectivity for a multilayer reflector)
λ_{Res}	Resonance wavelength
ν	Poisson's ratio
ω	Angular frequency of light
ω_0	Gaussian beam waist

LIST OF APPENDICES

CHAPTER 1 INTRODUCTION

Optical devices based on deep-etched silicon-air multilayer assemblies attracted considerable attention during the past few years. The reasons for this are numerous. First, silicon is essentially transparent at wavelength ranging from 1.2 μm to 8 μm [1], making it an ideal material for devices operating in the main optical fiber telecommunication windows (centered at 1310 nm and 1550 nm). Optical devices operating at these wavelengths find applications in optical telecommunications, of course, but also in fields such as chemical and physical sensing, which benefit from the great variety of optical equipments (e.g. sources, detectors) dedicated to the telecommunication industry. Moreover, the wide availability of silicon substrates and of silicon processing equipments, strongly driven by microelectronics and microsystems manufacturers, makes silicon a platform of choice for the development of new technologies.

Secondly, in this transparency window, the refractive index of silicon (n_{Si}) is very high (3.47772 at $\lambda = 1550$ nm [2]) compared with the refractive index of air (1.00027 at room temperature and pressure [3]). As will be discussed in Chapter 2, this very high refractive index contrast allows silicon-air multilayer reflector to reach very high reflectivities for very few silicon-air periods. In turn, such high reflectivity mirrors can be used to build compact optical cavities—such as Fabry-Perot interferometers—with strong light confinement abilities.

Thirdly, and perhaps more importantly, fabrication of silicon-air multilayer by deep silicon etching yields optical axis that are parallel to the silicon substrate. Throughout the current work, we will refer to this configuration as being "in-plane" with the substrate, as opposed to interferometers relying on thin film deposition, which yield "out-of-plane" devices. In-plane configurations greatly facilitate monolithic integration of deep-etched interferometers with electrical, micromechanical, and microfluidic features.

1.1 Literature review

Etching of one-dimensional periodic reflectors in semiconductor platforms was proposed more than 30 years ago [4] and was later used, in particular, for the fabrication of in-plane lasers in III-IV semiconductors [5, 6]. In silicon, however, the first reports of deep-etched silicon-air multilayer structure were published only in 1999 [7, 8], which coincides with the development of Bosch deep reactive ion etching (DRIE), in the middle of the 90's decade [9]. These reports [7, 8]

did not target a specific application, but focused mainly on the new possibilities of DRIE for silicon photonics. A few years later, Barrios et al. [10, 11] reported an in-plane, waveguided silicon-on-insulator Fabry-Perot cavity (see Figure 1.1) for signal modulation and tunable filtering applications. Electro-optic tuning of the Fabry-Perot resonance wavelength, for both signal modulation and tunable filtering applications, was achieved through integration of a p-i-n junction across the waveguided cavity. A 11.2 finesse, 50% modulation depth, and 1 ms response time were achieved. The device response time and insertion losses (e.g. -10 dB for fiber-waveguide coupling only) would most likely need significant improvement to comply with optical fiber telecommunications requirements. The level of integration achieved experimentally (silicon-air Bragg mirror, rib waveguide, p-i-n junction) is however considerable, making this work an important original accomplishment.

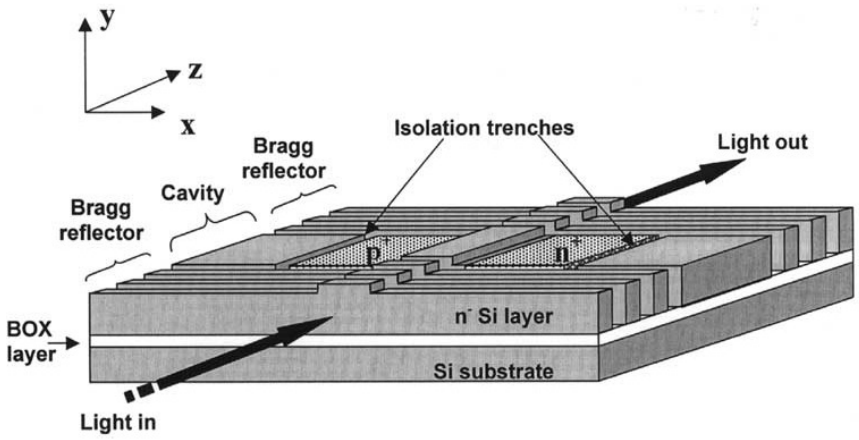

Figure 1.1: Schematic representation of a deep-etched Fabry-Perot cavity. A p-i-n junction is used to change the waveguide effective index for signal modulation and tunable filtering applications. Reproduced from ref. [11].

The same year, Yun et al. [12] reported a thermally tunable deep-etched Fabry-Perot interferometer. In this case, grooves for optical fiber passive alignment were etched simultaneously with a free-space (i.e.: no waveguide) interferometer. Thermo-optic tuning of the Fabry-Perot resonance wavelength was achieved using an integrated electric micro-heater. An almost 10 nm tuning range was achieved. No transmission measurements were however reported, which do not allow further comments on the device performances.

An important difference between the original works of Barrios et al [10]. and Yun et al. [12] is the use of a waveguided optical cavity, in the first case, and of an unguided (i.e. free-space) optical cavity in the latter case. These two designs each present significant advantages and drawbacks, depending of the targeted application. We will therefore clearly distinguish these two types of interferometer for the remainder of the current section.

1.1.1 Waveguided interferometers

To the best of the author's knowledges, following the work of Barrios et al. [10, 11], only one group continued to work on in-plane waveguided silicon-air multilayer interferometers. Their contribution to the field is however substantial, comprising, for example, plasma etching process development, chemical sensors, and fundamental work on opto-mechanical phenomena. Pruessner et al. reported, in 2006 [13], a cryogenic temperature plasma etching process for the fabrication of high surface quality silicon multilayer structures. This work was followed, shortly after, by a report of waveguided Fabry-Perot cavites with finesses reaching nearly 500 [14]. Such achievement is significant, considering that to date, no other deep-etched multilayer cavity was able to reach finesses above 50 (e.g. see Chapter 4, Table 4.1).

As will be discussed in Chapter 3 (section 3.1.1), finesse is proportional to the number of round trips that photons undergo before exiting an optical cavity. In other words, finesse is an indication of the light confinement ability of an optical cavity. Resonators with high finesses can therefore be used to enhance the interaction of light with, for example, micromechanical structures for studies of opto-mechanical coupling phenomena. High finesses also yield narrow optical resonance peaks, which can consequently be located more precisely in interferometric sensing applications.

Pruessner et al. exploited these advantages of high finesses by integrating their optical cavity with an important variety of devices. In [15], an electromechanical actuator was integrated with one of the two cavity mirrors, allowing mechanical adjustments of the cavity length for tunable filtering applications (see Figure 1.2). A considerable spectral tuning range was achieved (> 30 nm) with relatively narrow resonance peaks (< 0.5 nm). Mechanical deformations of the actuated Bragg mirror however induced asymmetries in the reflectivity of the cavity mirrors (see Figure 1.2 (c, d)), which translated in 20 dB insertion losses upon tuning. These losses, added to

fiber-waveguide coupling losses (10 dB) and intrinsic cavity losses (6 dB), would most likely be too important for most filtering applications (e.g. in optical fiber telecommunication networks).

A completely different application of the same devices was also reported in [15]. Instead of being tuned, the cavity resonance was tracked over time to measure the thermal-mechanical (Brownian) noise spectrum of the electromechanical actuator. Although mostly conceptual, this work outlined the potential of deep-etched Fabry-Perot interferometers as integrated readouts for resonant mechanical sensors, as would be demonstrated shortly after in [16].

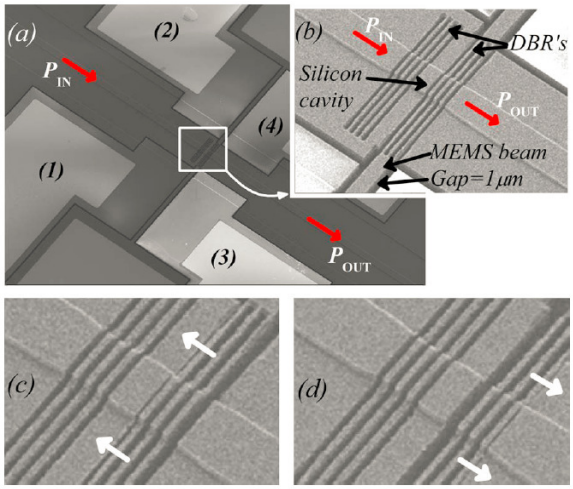

Figure 1.2: (a, b) Scanning electron microscopy image of a waveguided Fabry-Perot cavity integrated with a micro-electromechanical actuator. For waveguided interferometers, mechanical actuation (c, d) affects the mirrors symmetry. Reproduced from ref. [15].

In [16], MEMS actuators, similar to those presented in Figure 1.2, were coated with gas absorbent polymers. Gas absorption in the polymers changed the actuators effective masses, inducing a shift of their mechanical resonance frequency. These shifts were monitored, as in [15], by tracking the position of the Fabry-Perot optical resonance wavelength over time. A limit of detection (LOD) of 68 parts per million (ppm) water vapor was achieved experimentally.

Observations of opto-mechanical coupling phenomena were also reported using high finesse Fabry-Perot resonators in [17]. Detuning the wavelength of a laser pump from the cavity optical resonance condition was demonstrated to induce damping, or amplification, of the

actuator mechanical resonance. The authors argue that such mechanical resonance amplification could be used for passive remote interrogation of their resonant chemical sensors [16], avoiding the need for an on-site electrical power supply.

1.1.2 Free-Space interferometers

Following the work of Yun et al. [12], four other groups (including the author's affiliation) realized free-space tunable Fabry-Perot filters based on deep-etched silicon-air multilayer mirrors [18-22]. In all these cases, spectral tuning was achieved by displacing one of the Fabry-Perot mirrors using a monolithically integrated MEMS actuator (see Figure 1.3).

Interestingly, for free-space Fabry-Perot filters, tuning by mechanical deformation does not affect symmetry of the interferometer mirrors (as was the case for waveguided designs in e.g. Figure 1.2 (c, d)). Large spectral tuning ranges with limited losses due to asymmetric mirror reflectivities are therefore potentially achievable. Another advantage, compared with waveguided designs, is the lack of losses caused by fiber-waveguide coupling. As shown in Figure 1.3, free-space Fabry-Perot are coupled directly with optical fibers, which are passively aligned, next to the interferometer, in monolithically integrated fiber grooves.

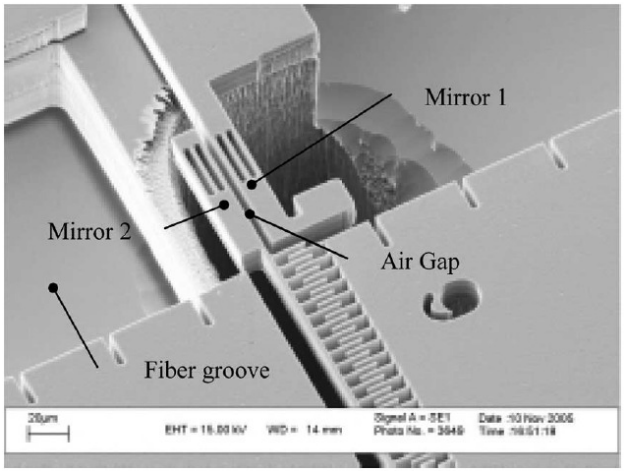

Figure 1.3: Scanning electron microscopy image of a free-space Fabry-Perot tunable filter integrated with a micro-electromechanical actuator. Reproduced from ref. [19].

Despite these advantages, the performances of reported deep-etched tunable filters are still relatively poor compared with other commercially available technologies (e.g.: Micron Optics,

Inc. FFP-TF tunable filter [23]), which provide insertion losses smaller than 3 dB, finesses up to 4000, and scan rates of a few KHz over wavelength ranges up to 200 nm. MEMS based silicon-air filters can easily compete with such scan rate and ranges (e.g. see [21]). However, as outlined also in Chapter 4, Table 4.1, their insertion losses reach, in the best case [19], 10 dB, while their finesse never exceeds 50. In an attempt to identify the causes of such high insertion losses and finesse reduction, Lipson et al. [24] provided optical simulation algorithms that account for Gaussian beam divergence[1] at the output of the coupling optical fibers, and for imperfect verticality of the multilayer etch profiles. Both sources of loss were found to be significant. On the other hand, the effect of other sources of losses—such as surface roughness at silicon-air material interfaces, or misalignment between the input and output coupling optical fibers—remains to be explored.

Deep-etched silicon filters still have a potential significant advantage in term of mass producibility (hundreds of tunable silicon filters can easily be fabricated simultaneously on a single silicon wafer). In comparison, commercially available tunable optical fiber filters [23] rely on thin film multilayers deposited on the tip of cleaved optical fibers, which are then displaced using a piezoelectric actuator to achieve tuning. However, as will be described in greater details in Chapter 2, section 2.3.2, plasma etching of free-space interferometers [18-22] produces silicon-air optical layers with unpredictable dimensions [19]. This unpredictability requires all the fabricated filters to be characterized individually to discard malfunctioning devices; a task that is typically not compatible with mass production.

Free-space Fabry-Perot interferometers were not only used as tunable filters, but also as integrated readouts for micromechanical accelerometers [25] and displacement sensors [26]. Optical readout of an accelerometer response, rather than the usual capacitive measurement, is expected to provide greater stability in strongly irradiated environments, such as outer space. In [25], a 400 μg resolution (i.e. 400×10^{-6} times the earth gravitational constant "g") and a 2.5 nm/g sensitivity were achieved experimentally. In [26], a deep-etched Fabry-Perot cavity allowed

---

[1] This formalism will be revisited in Chapter 4, where a mistake in Lipson and Yeatman model will be demonstrated to underestimate losses due to Gaussian beam divergence. However, the originality of the proposed calculation method must, of course, still be credited to these authors.

characterization of a new type of MEMS motion translation system. Vertical to horizontal motion translation by the micro system was successfully monitored using the integrated Fabry-Perot interferometer.

The above-mentioned works on free-space Fabry-Perot filters [18-22] and displacement sensors [25, 26] all have in common the use of planar mirrors. As will be described in Chapter 4, with planar mirrors, losses caused by Gaussian beam divergence typically prevent the design of free-space interferometers with very long path lengths (i.e. large distance between the interferometer mirrors). Malak et. al [27] proposed a solution to this limitation by designing cylindrical mirrors (to confine light horizontally) and by including a fiber rod lens (to confine light vertically) between the cavity mirrors. The finesse of proposed interferometers reached 20, which is not higher than what was obtained with planar mirrors (see also Chapter 4, Table 4.1). The proposed devices however allow greater design flexibility for applications that would require longer path length (i.e. smaller free spectral range).

Deep-etched silicon-air multilayer assemblies were also used to create one-dimensional photonic crystals [28, 29]. These photonic crystals were later infiltrated with liquids for sensing [30, 31] and tunable filtering [32] applications. As for tunable Fabry-Perot filters, the optical resonances obtained experimentally were always found to be much broader than what could be expected from basic, ideal-case simulations.

Spectral tuning was achieved by filling the multilayer assembly with a liquid crystal solution, in which molecules rearranged (changing the liquid refractive index) upon exposition to an electric field [32]. Spectral shift of 1.6% and 30 ms response time were obtained experimentally. For comparison, tunable Fabry-Perot filters based on electromechanical actuators [21] achieved a 104 nm tuning range at 1550 nm (6.7%) and a 14.4 KHz mechanical resonance frequency (i.e. response time < 1 ms).

Refractive index sensing was achieved by infiltrating liquids to be characterized in the air layers of the photonic crystal [30]. Liquid injection in the photonic crystal would later be facilitated by the use of a monolithically integrated microfluidic system [31]. In the latter case, a 670 nm/RIU (refractive index units) resonance wavelength sensitivity to refractive index changes, and a 10^{-3} RIU resolution were reached.

1.2 Problem statement and objectives

The results presented above in the literature review can be summarized as follow:

- Interferometers based on deep-etched multilayer resonators present the important advantage of being integrable with a great variety of devices. More specifically, integration of deep-etched silicon-air multilayer with the following features was demonstrated experimentally:
    - Waveguides
    - Passive alignment grooves for optical fibers
    - Microfluidic channels and reservoirs
    - Liquid samples
    - Microelectromechanical (MEMS) actuators
    - Micromechanical accelerometers
    - Electric micro-heater
    - Liquid crystals
    - p-i-n junctions
    - Cylindrical micro lenses.
- However, in all cases, insertion losses are always very high (>10 dB). Finesses also never exceeds 50 (except for the notable exception of Pruessner et al. work [14]).
- For free-space interferometers, unpredictability of the fabricated silicon-air layer dimensions produces devices with random optical behaviors (for more details on this phenomenon, please see Chapter 2, section 2.3.2). Such unpredictability would not allow an eventual industrial production to reach acceptable yields, even for applications that could tolerate high insertion losses and low finesses.

Objective 1: Fundamentals of deep-etched multilayer optical interferometers

Sub-objective 1.1: Sources of loss affecting deep-etched multilayer optical interferometers

The first objective of this work is to provide a better understanding of the sources of loss affecting deep-etched silicon-air multilayer resonators. More specifically, we aim to provide models for the following loss mechanisms:

- Gaussian beam divergence in free-space propagation regions of the interferometers
- Surface roughness at silicon-air material interfaces
- Imperfect verticality of the multilayer etch profiles
- Misalignments between the input and output coupling optical fibers (for free-space interferometers working in transmission).

Sub-objective 1.2: Design methods for improvements of fabrication predictability

We also aim to provide a design and fabrication method that will improve the predictability of the etched devices dimensions, avoiding random optical behavior to occur.

Objective 2: Development of new applications

Even if deep-etched multilayer interferometers were already integrated with a great variety of devices (see listing at the beginning of the current section), the number of groups that focused on this subject (10) is relatively small compared with other technologies, such as whispering gallery mode resonators, that attracted the attention of several dozens of groups over the years [33]. We therefore aim to continue the development of new applications of interferometers based on deep-etched silicon-air multilayer interferometers.

Two approaches will be used to avoid the limitations imposed by the typically high insertion losses and low finesses of previously reported devices. We will first target sensing applications, for which high insertion losses and low finesses are not a critical problem. Indeed, losing more than 90% signal intensity in a sensor is not as critical as in telecommunication

applications, as long as the sensor still yields a strong response to variations in the targeted analyte. More specifically, the two following types of sensors will be demonstrated:

Sub-objective 2.1: Development of a refractive index sensor for silicon microfluidic systems.

Sub-objective 2.2: Development of a gas sensor.

Secondly, we will investigate Gires-Tournois interferometers (GTI). GTIs have never been implemented in planar lightwave circuits and, compared with Fabry-Perot interferometers, have the potential to be less affected by fabrication imperfections. Indeed, as will be described in Chapter 3, section 3.2.1, a GTI typically includes a low reflectivity mirror, and is therefore a weak light confinement interferometer. We hypothesize that such weak confinement will lead to weaker interactions of light with fabrication imperfections, which will in turn lead to less important insertion losses than with Fabry-Perot interferometers.

Sub-objective 2.3: Development of Gires-Tournois interferometers for optical fiber telecommunication applications.

1.3 Thesis organization

The next two chapters present the ideal properties of silicon-air multilayer reflectors (Chapter 2), and of the two types of interferometers—free-space Fabry-Perot and waveguided Gires-Tournois—that will be investigated in this thesis (Chapter 3). Chapter 2 also presents the main characteristics of inductively coupled plasma (ICP) etching technology, which will be used to fabricate all the devices presented in the current work. Chapter 4 - Chapter 7 present articles that are either published or submitted to peer reviewed journals.

Chapter 4 addresses the first objective of this work by presenting models for the main sources of loss affecting deep-etched multilayer optical resonators. A design and fabrication method to improve dimension predictability, upon fabrication, is also reported. Chapter 5 and Chapter 6 present sensing applications of deep-etched free-space Fabry-Perot interferometers. In Chapter 5, a Fabry-Perot sensor is integrated with a silicon microfluidic system to perform refractive index measurement of homogenous liquids. In Chapter 6, similar interferometers are

functionalized with absorbent polymers to create a gas sensor. Finally, Chapter 7 presents experimental results on waveguided Gires-Tournois interferometers.

Of course, each of the three articles that target new applications (refractive index sensing, gas sensing, Gires-Tournois interferometer) also include literature reviews on other type of devices that targeted the same applications. The cited references were not repeated above in the literature review to avoid duplications.

It should also be noted that the journal articles are not ordered chronologically. The results presented in Chapter 5 were obtained and published prior to the development of the modeling, design, and fabrication methods presented in Chapter 4. Therefore, the results presented in Chapter 5 did not benefit from the design and fabrication methods presented in Chapter 4. A greater difference can consequently be observed between the experimental and simulated results in Chapter 5, compared with the following articles (Chapter 6, Chapter 7).

1.4 Author's contribution to co-authored articles

This section details the author's contribution to Chapter 4 to Chapter 7, which are articles co-authored by multiple collaborators.

The theoretical modeling presented in Chapter 4 was carried essentially by the author. Alexandre Poulin participated to the fabrication of the test structures that were used for surface roughness measurements.

The refractive index sensor presented in Chapter 5 was originally proposed by Yves-Alain Peter and Jonathan Masson. The design was later optimized by the author (e.g. effect of mirror separation, section 3.1.2). The final design, fabrication, experimental characterization, and theoretical modeling presented in Chapter 5 were all carried by the author.

The gas sensor presented in Chapter 6 is based on Fabry-Perot interferometers that were fabricated by the author. These interferometers were subsequently functionalized with polymers chosen (and synthesized, in the case of PDMS-PDPS) by the authors affiliated with Queen's University. Gas exposure experiments were all carried at Queen's University. The author was present for approximately half of these measurements. Interpretation of the experimental results, theoretical formulation, finite element modeling, and manuscript redaction were all carried by the author.

Finally, the Gires-Tournois interferometers presented in Chapter 7 were originally designed by the author. Thomas Kerrien and Alexandre Poulin participated to the development of the fabrication process, while Hubert Camirand carried finite element optimization of the waveguide dimensions to maximize fiber-waveguide coupling efficiency (e.g. see also Figure 3.9). Fabrication of the final devices, theoretical modeling, optical characterization, and manuscript redaction were all carried by the author.

CHAPTER 2 DEEP-ETCHED SILICON-AIR MULTILAYER REFLECTORS

Deep-etched silicon-air multilayer mirrors are the basic components of all the devices presented in this work. This chapter presents the ideal properties of these mirrors, followed by a description of their fabrication process by inductively coupled plasma (ICP) etching. The technological limitations of this fabrication process and their consequences on the mirror structures are also presented.

2.1 Ideal properties

Figure 2.1 presents multilayer mirrors based on 1.5 and 3.5 silicon-air periods. For these mirrors to have a high reflectivity at a given central wavelength (λ_c), the thickness of each layer of the assembly must equal an odd integer multiple of $\lambda_c/4$, normalised by the refractive index of the materials (see notation in Figure 2.1b). In this chapter will we refer to deep-etched mirrors using a notation based on the odd integer multiples of the silicon and air layer thicknesses: (m_{Si}, m_{Air}). As all the devices presented in this work operate around the conventional ("C" band) optical fiber communication wavelength range, λ_c = 1550 nm is always used for design purposes. In this case, the nominal thickness of each silicon layer must equal an odd integer multiple (m_{Si}) of 111 nm, while the nominal thickness of each air layer must equal and odd integer multiple (m_{Air}) of 388 nm.

The ideal reflection spectrum of any multilayer assembly (assuming that the material refractive indices are isotropic) can easily be simulated using the widely acknowledged transfer matrix formalism [34]. In Chapter 4, we will combine this formalism with models that account for the non-idealities of the fabricated devices (Gaussian beam divergence at the output of the optical fibers, surface roughness, imperfect verticality of the etched profiles, optical fiber misalignments). In the present case, however, we aim to describe the ideal properties of deep-etched silicon-air reflectors. We therefore neglect all these imperfections to consider only the reflection of a plane wave, at normal incidence, on a defectless multilayer assembly.

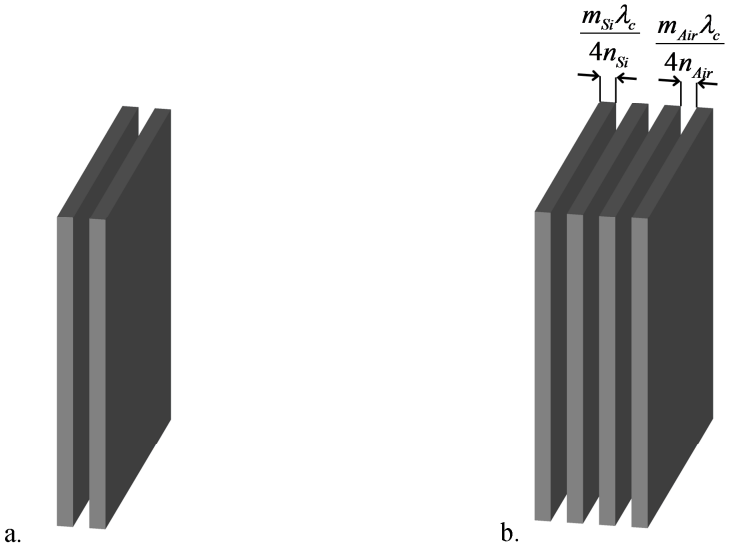

Figure 2.1: Schematic representation of 1.5 periods (a) and 3.5 periods (b) deep-etched silicon-air multilayer mirror. The nominal dimensions of the silicon and air layers are expressed by odd multiples (m_{Si}, m_{Air}) of quarters of the targeted central wavelength of operation (λ_c), over the refractive index of the materials (n_{Si} or n_{Air}).

Figure 2.2 presents the simulated reflection spectrum of a 2.5 silicon-air periods mirror having (m_{Si}, m_{Air}) = (17, 5) layer orders (which corresponds to typical silicon and air layer thicknesses ~ 2 μm). The peak reflectivity occurs at the central wavelength, which is set at λ_c = 1550 nm. We define the reflection bandwidth as the full width at -0.5 dB from peak reflectivity (i.e., full width at ~90% of peak reflectivity), as labelled in Figure 2.2. In Figure 2.2, the width at -0.5 dB is 100.9 nm and therefore largely covers, for example, the conventional (C) optical fiber telecommunication band (1530 nm - 1570 nm).

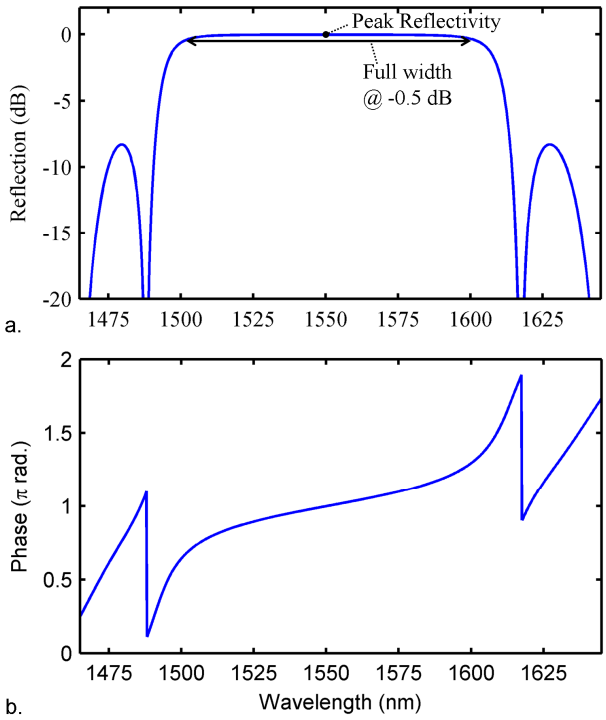

Figure 2.2: (a) Ideal intensity reflection spectrum of a (m_{Si}, m_{Air}) = (17, 5) deep-etched mirror of 2.5 silicon-air periods (P) centered on λ_c = 1550 nm. The peak reflectivity and -0.5 dB bandwidth are labelled. (b) Optical phase shift upon reflection on the same multilayer mirror.

The large bandwidth obtained in Figure 2.2 is due to the important refractive index contrast between silicon (n = 3.4787) [2] and air (n = 1.0003) [3], and is also function of the m_{Si} and m_{Air} layer orders. In Figure 2.3, the bandwidth of a 2.5 periods mirror is now calculated for all the possible combinations of m_{Si} layer orders from 1 to 35 (i.e. silicon layer thicknesses up to 3.9 μm) and m_{Air} layer orders from 1 to 11 (i.e. silicon layer thicknesses up to 4.3 μm). Lower layer orders are found to yield the largest bandwidths. In this work, we will therefore always design the lowest m_{Si} and m_{Air} layer orders permitted by our fabrication process, in order to reach the highest possible bandwidths.

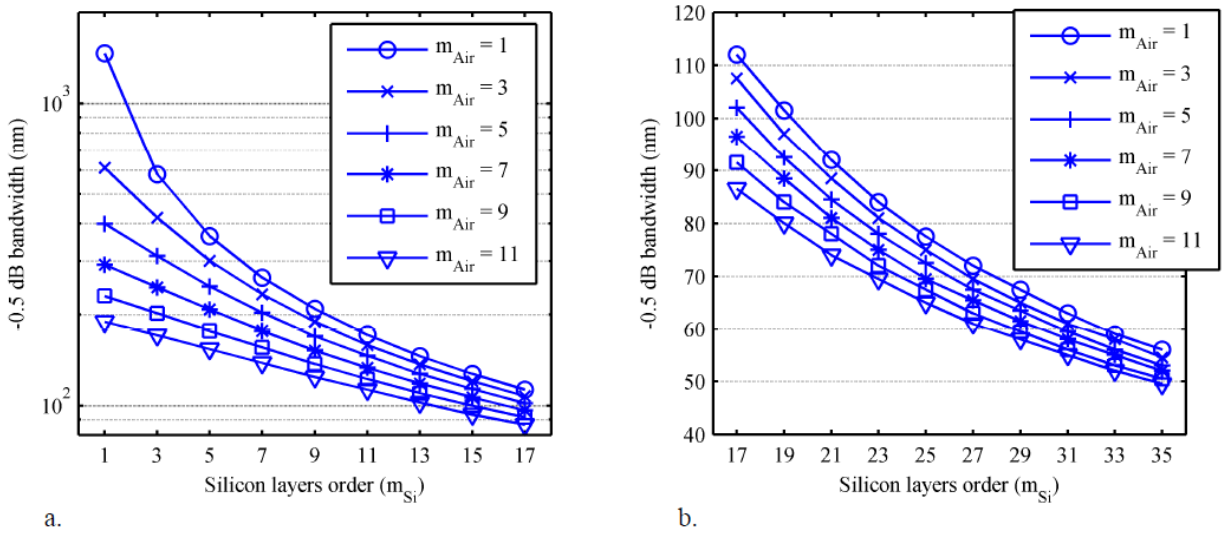

Figure 2.3: Reflection bandwidth (at -0.5 dB) as a function of the (m_{Si}, m_{Air}) dimension parameters and for 2.5 silicon-air Bragg periods. (a) m_{Si} orders from 1 to 17. (b) m_{Si} orders from 17 to 35.

The number of silicon-air periods (P) also influences, modestly, the mirrors reflection bandwidths. In Figure 2.4, the same reflectivity spectrum as in Figure 2.2 is reported again and is now compared with mirrors having 1.5 and 3.5 silicon-air periods. As the number of periods increases, the reflection band is more sharply defined, which yield slightly larger bandwidths. Mirrors having 1.5 or 3.5 silicon-air periods still respect, for any m_{Si} and m_{Air} layer orders, the relation presented in Figure 2.3. The values obtained from Figure 2.3 however need to be reduced by 11% for 1.5 periods mirrors, and increased by 2% for 3.5 periods mirrors.

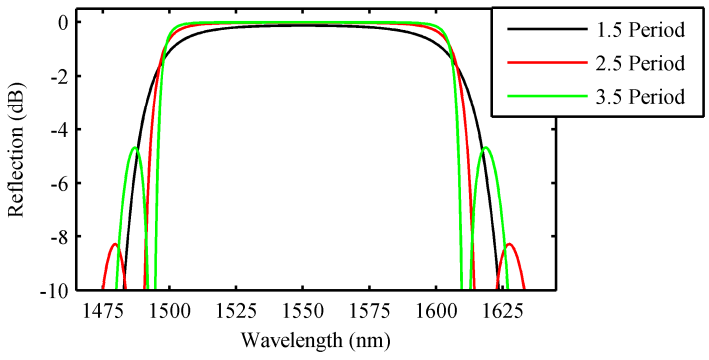

Figure 2.4: Ideal intensity reflection spectrum of a (m_{Si}, m_{Air}) = (17, 5) deep-etched mirror for various number of silicon-air periods (P).

Finally, the number of silicon-air periods also influences the peak reflectivity of the mirrors. Table 2.1 presents the peak reflectivity of silicon-air multilayer mirrors for various numbers of Bragg periods. Because of the high silicon-air refractive index contrast, mirrors having as few as 1.5 periods yield simulated reflectivity > 95%. This reflectivity rapidly increases to reach more than 99.9% for only 3.5 periods. Interestingly, peak reflectivity does not depend on the m_{Si} and m_{Air} dimension parameters, as long as these remain odd integers.

Table 2.1: Peak reflectivity vs. number of Bragg periods.

Number of Bragg periods (P)	Peak reflectivity (%)
1.5	97.3
2.5	99.77
3.5	99.981

2.2 Fabrication using time-multiplexed room temperature inductively coupled plasma etching

All the silicon-air multilayer reflectors used in this work are fabricated using room temperature[2] inductively coupled plasma (ICP) etching of silicon. This section presents briefly the operation principle of ICP reactors, followed by the influence of the main controllable process parameters. The technological limitations of the fabrication process used in the current work are then presented together with an overview of their consequences on the optical properties of silicon-air multilayer resonators.

For a review of silicon micromachining techniques, other than ICP etching, that have been used for the fabrication of vertical optical planes, please see Chapter 4, section 4.5.

2.2.1 Pattern definition using UV contact lithography

The features to be etched, on a given silicon wafer, must of course be defined by a physical mask prior to ICP etching. We use, for that purpose, conventional UV contact lithography, as schematized in Figure 2.5. A photoresist layer is first spin coated and baked on the surface of the silicon wafer. The wafer is then exposed to UV light through a photomask that consists of a UV transparent substrate (e.g. quartz) coated with a thin metal layer, which is patterned by laser writing or by electron beam lithography. This metal layer blocks UV light except in zones that are intended for subsequent plasma etching (in the case of positive photoresists). In these zones, UV radiation breaks molecular links within the resist, which then become soluble in a dedicated developer solution (again, this is valid for positive photoresist. For negative photoresists, UV exposition activates a molecular cross-linker, such that the exposed zones become insoluble, while the unexposed zones remain soluble. Negative photoresists therefore produce, for a given photomask, the exact opposite patterns as with positive photoresist).

---

[2] In fact, for the etching recipes used in this work, the process temperature is set between 0 °C and 40 °C. The term "room temperature" is used in opposition with "cryogenic" temperature etching, which rely on significantly different chemistries.

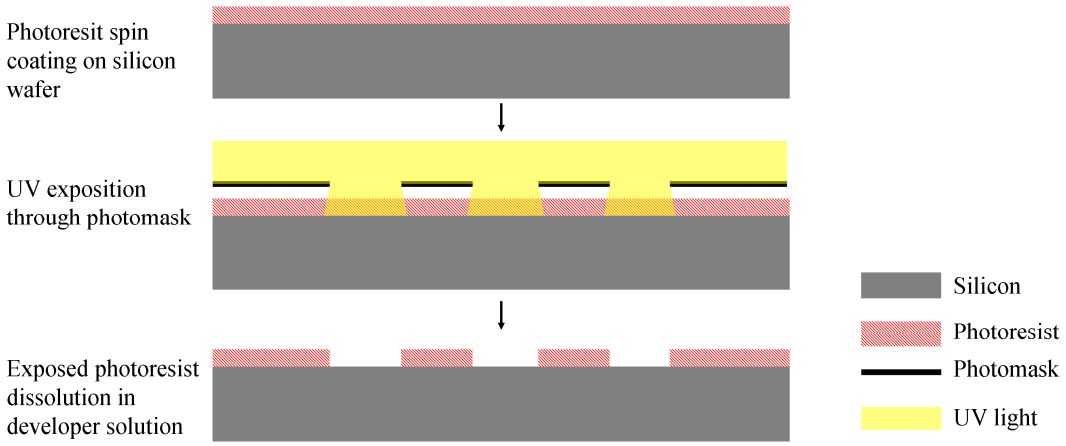

Figure 2.5: Schematic cross section view of a contact UV photolithography process performed with positive photoresist.

The smallest feature that can be defined using contact lithography is determined by optical diffraction and by the thickness of the photoresist film. In our case, UV radiation from a mercury lamp (λ ~ 400 nm) and film thicknesses between 1 µm (Shipley® S1813 positive photoresist) and 4 µm (Megaposit™ SPR 220 series positive photoresist) are used. In these conditions, resolutions between 1 µm (for ~ 1 µm thick films) and 1.5 - 2 µm (for ~ 4 µm thick films) are typically achievable using our photomask aligner (Karl Suss MA-4). Thinner films are indeed preferable for higher resolutions. However, as will be discussed in sections 2.2.2 - 2.2.5, ICP etching of silicon also erodes photoresist, such that thicker photoresist films are required when etching of deeper silicon features is intended (i.e. the photoresist-silicon etch selectivity is not infinite).

2.2.2 Inductively coupled plasma etching principle

In both industrial and academic environments, inductively coupled plasma etching is undoubtedly the method of choice for any application requiring high aspect ratio etching of silicon. As this technology is very mature, most technical developments are carried by equipment manufacturers, such that few recent academic publications address its fundamental aspects. Several publications report phenomenological optimization of fabrication recipes for specific applications [35-47]. However, as all ICP reactors differ considerably, these recipes are rarely transferable from one equipment to another. Fundamental—rather than phenomenological—

understanding of ICP etching is therefore highly desirable for the development of fabrication processes. For that purpose, ref. [48] is, in the author's opinion, certainly the most valuable source of information. The detailed influence of the main ICP process parameters given below is, in great part, a summary of the process guidelines given in this publication.

A schematic illustration of a typical ICP etching chamber is presented in Figure 2.6. Etching and passivation gases are admitted in the chamber—separately or simultaneously, depending on the recipe—at precise flows rate using mass flow controllers. For most silicon etching processes, and in the current work, SF_6 is the etching gas while C_4F_8 is used as the inhibitor. The pressure inside the chamber is controlled, usually in the 10 - 50 mTorr range, by adjusting the opening of a throttle valve leading to a turbo pump. In order to allow time-multiplexed processes, this pump must have a very high pumping capacity relative to the chamber volume, such that it is able to switch the chamber content in less than 1 second upon injection of a different gas mixture.

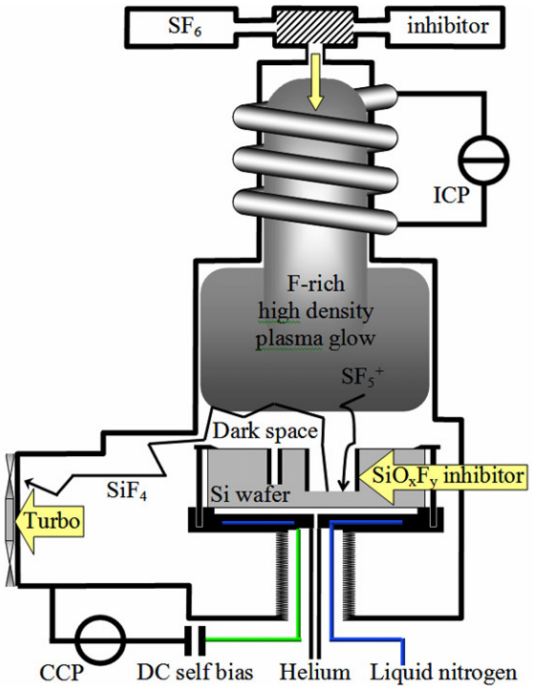

Figure 2.6: Schematic representation of an inductively coupled plasma (ICP) reactor. Reproduced from ref. [48].

Two radiofrequency (RF) sources are used to activate the etching and passivation plasmas. A solenoid coil around the top narrow part of the reaction chamber (see Figure 2.6) creates the inductively coupled plasma that dissociate the SF_6 and C_4F_8 gas precursors, creating SF_5 and CF_x free radicals. These free radicals are then directed towards the silicon substrate using a capacitive coupled plasma (CCP) formed between the wafer and the chamber itself (see Figure 2.6). This two-plasma sources configuration permits very high concentrations of free radicals through highly energetic ICP (ICP power is usually set between 500 W and 2000 W), while limiting ion bombardment on the substrate by using lower power CCP (usually around 10-25 W). Highly reactive plasmas (high ICP power) allows high silicon chemical etch rates while low CCP power limits physical erosion of the etch mask material. Very high etching selectivity between silicon and the etch mask can therefore be achieved (e.g., 100:1 for SiO_2 masks, 50:1 for photoresist masks). In turn, this high selectivity, combined with low pressure operation, allows etching of trenches having higher aspect ratio (typically 1:30) than with any other silicon etching technology.

As the SF_5^+ free radicals are created mostly in the top part of the etching chamber by the ICP plasma and are then impacted on the wafer using the CCP source, their angles of incidence on the substrate are mainly vertical. Such feature is essential for high aspect ratio etching but is not by itself sufficient to achieve near-perfectly vertical trenches. As shown in Figure 2.7, two phenomena prevent perfect verticality in the cases where no (or insufficient) inhibitor gas (C_4F_8) is used. Firstly, the SF_5^+ free radicals experience collisions on their path toward the substrate, such that the ions impacting the surface have a non-negligible ion angle distribution (IAD). IAD minimization can be achieved by increasing CCP power (to attract the ions more strongly toward the substrate) or by decreasing pressure to minimize the amount of collisions. However, at lower pressures, another phenomenon becomes dominant and causes verticality deviations. As the wafer is negatively charged by the CCP source, the trajectory of the positively charged SF_5^+ ions can be deflected by the trenches sidewalls. This phenomenon is usually referred to as the image force (IF) effect and is illustrated in Figure 2.7. For very narrow trenches, the forces from both sides of the trenches counteract each other, but not in wider openings.

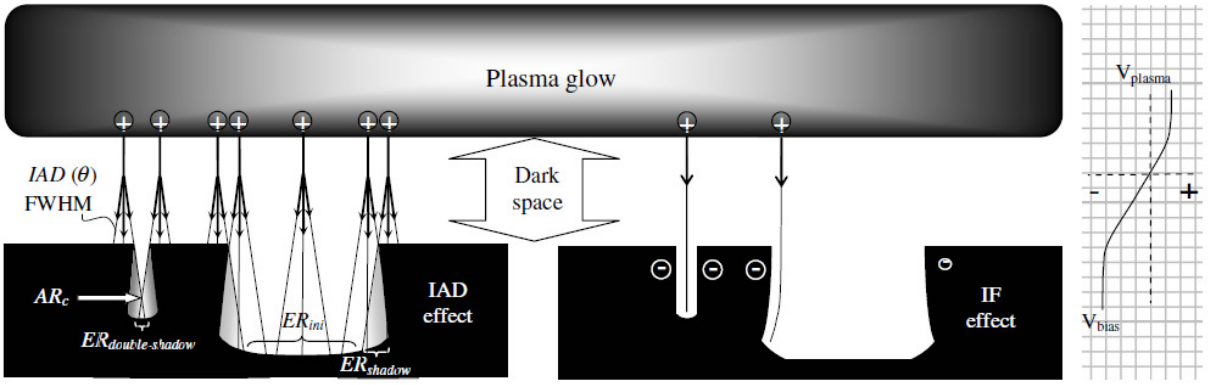

Figure 2.7: Schematic representation of the phenomena that affect verticality of the etch profiles during ICP deep etching. Ion angular distribution (IAD) is usually the dominant effect at higher pressures, while image force effect (IF) dominates at lower pressure. Reproduced from ref. [48].

In order to achieve nearly perfect verticality, an inhibitor gas (C_4F_8 in our case) must be used together with the SF_6 etching gas. Plasma dissociation of C_4F_8 creates CF_x radicals that deposit on the wafer, creating a fluorocarbon protective layer that prevents the IAD and IF effects. If C_4F_8 is used with SF_6, in well adjusted proportions, only the SF_5^+ ions that have an almost perfectly vertical trajectory will have enough energy to break the protective coating and reach silicon, thus preventing the IAD effect. Similarly, the protective fluorocarbon coating creates a charge barrier on the etched sidewalls, which prevents image force (IF) effect.

Although vertical profiles can be achieved through mixed processes that use simultaneously C_4F_8 and SF_6 in a continuous fashion, this approach is usually quite inefficient in terms of etch rate and mask selectivity. The continuous presence of C_4F_8 diminishes the etch rate of the process, which leaves more time for ion bombardment to physically erode the etch mask, thus decreasing the selectivity. This approach is therefore rarely used for etching of high aspect ratio features (e.g., silicon-air multilayer mirrors). However, for application requiring high surface quality and relatively small etch depths (e.g. silicon waveguides etching), mixed process can yield useful performances [44, 47].

For room temperature high aspect ratio etching of silicon with high mask selectivity, time-multiplexed processes, rather than mixed processes, are usually preferred. In this case, SF_6 and C_4F_8 plasmas are cycled inside the plasma chamber. Such cycling allows good etch rates during

the SF_6 plasma step, while applying optimal deposition conditions during the C_4F_8 plasma. A schematic illustration of a time-multiplexed process is presented in Figure 2.8. The etching steps use mainly SF_6 in order to reach high silicon etch rates, but also incorporate a small proportion (10 - 20%) of C_4F_8 inhibitor to limit IAD and IF effects as much as possible. Oxygen (5 - 10 %) can also be incorporated during the etch steps in order to facilitate passivation removal at the bottom of the etch trenches. The passivation steps use C_4F_8 only. As the aim of this step is to create a protective coating on the etched sidewalls, lower CCP power is used. Lower CCP power allows higher IAD of the CF_x free radicals, which can therefore impact and coat the trench sidewalls more efficiently.

As shown in Figure 2.8, alternating between etching and passivation steps creates rippled sidewalls, which phenomenon is usually referred to as "scalloping". Such surface roughness is of course not ideal for optical applications. However, the scalloping effect is strongly attenuated in high aspect ratio trenches such as deep etched multilayer mirrors [49]. In Chapter 4 (section 4.5.2), roughness profiles of typical deep etched trenches will be presented and will show that scalloping in not the dominant source of surface roughness for the devices presented in this work.

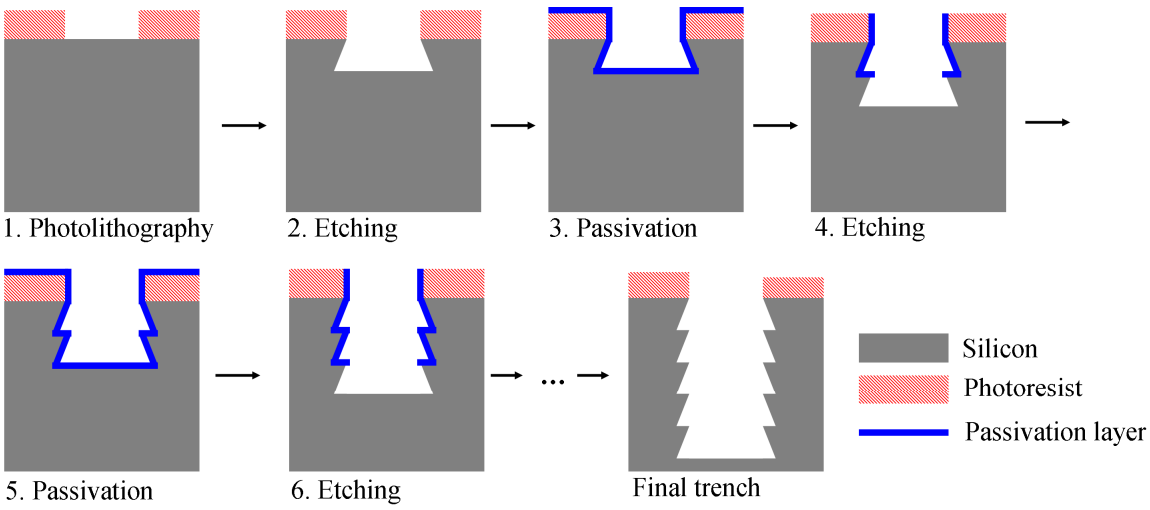

Figure 2.8: Schematic representation of a time multiplexed ICP etching process.

Adjusting the passivation and etch cycle times allows to reach the desired etch profiles (vertical in our case). If the etching step is too long compared with the passivation step, re-entrant profiles will be obtained. On the contrary, longer passivation steps will yield tapered profiles. Once the appropriate ratio of step times is determined, the etching and passivation steps are cycled up to a few hundred times until the desired etch depth is reached. For large openings, there is no etch depth limit (other than imposed by erosion of the etch mask) such that even through-wafer etching can be achieved. For smaller openings, reduced mass transport efficiency at the bottom of the etch trenches will eventually halt etching at aspect ratios around 1:30.

2.2.3 Baseline ICP recipe used in this work

All the devices presented in this work are etched in an Oxford Instruments (Oxfordshire, UK) ICP180-100 etcher available through the GCM (Groupes des Couches Minces, Polytechnique Montreal) microfabrication equipment pool. Unless otherwise noted, the standard recipe developed by the GCM staff is used. This recipe is presented in Table 2.2. The etching steps duration is usually adjusted between 4 and 6 seconds, which allow compensation for small variations from one wafer to another (for example, doping type and concentration [50] or the exposed silicon area [48] can influence the silicon etch rate, requiring more of less etch time).

Table 2.2: Baseline ICP etching recipe used in this work.

	Etching step	Passivation step
ICP Power (W)	450	450
CCP Power (W)	25	10
SF_6 flow rate (sccm)	65	0
C_4F_8 flow rate (sccm)	15	65
O_2 flow rate (sccm)	6.5	0
Temperature (°C)	20	20
Pressure (mTorr)	15	15
Step duration (s)	4-6	4

Typical trenches etched using the baseline recipe are presented in Figure 2.9. In Figure 2.9 (a), the wider (10 μm) opening has a 78 μm depth, which is representative of what will be used for, e.g., free space refractive index sensors in Chapter 5. The narrower (3 μm) openings

have a 64 μm depth. This lower depth is caused by the higher aspect ratios (1:20) in the narrower openings, which limit the amount of ions that reach the trenches bottom, and therefore reduces the etch rate. In Figure 2.9 (b), the trenches have an 11 μm depth, which is representative of the waveguided Gires-Tournois interferometer presented in Chapter 7. All the trenches presented in Figure 2.9—regardless of their width—yield nicely vertical profile, which are required for our optical applications.

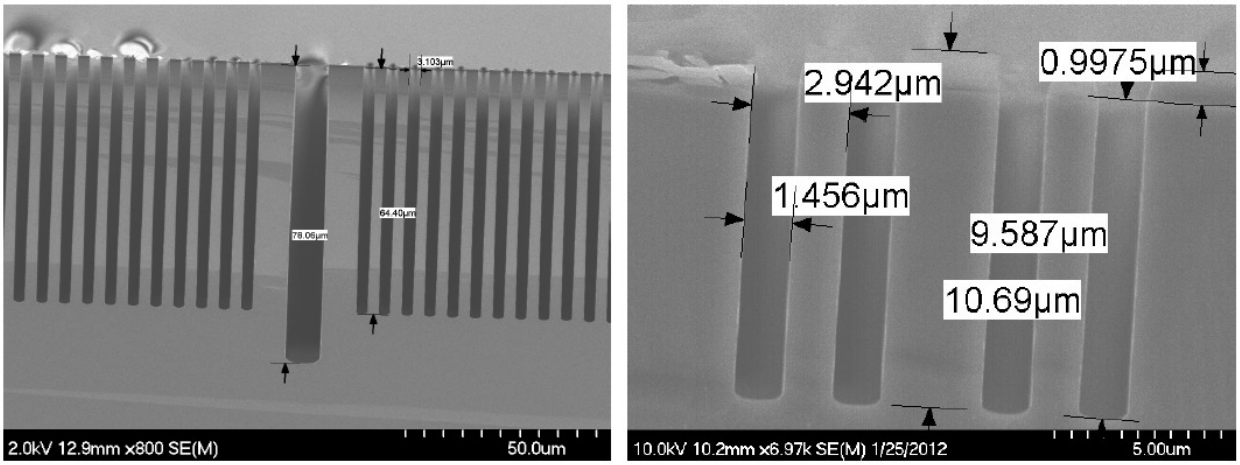

a. b.

Figure 2.9: Cross section view of test structures etched using the recipe reported in Table 2.2. (a) Trenches fabricated using 437 cycles with a 6 sec etching step and a 4 sec passivation step duration. (b) Trenches fabricated using 112 cycles with a 4 sec etching step and a 4 sec passivation step duration.

Both structures presented in Figure 2.9 used positive photoresist as the etch mask. In Figure 2.9 (b), as the targeted etch depth is small, a thin photoresist layer was used (Shipley S1813 spin coated at 4000 rpm for a layer thickness of approximately 1.5 μm). In Figure 2.9 (a), a thicker photoresist layer was used (Megaposit^{TM} SPR220 3.0 spin coated at 1000 rpm for a layer thickness of approximately 4.7 μm). In this case, reaching a 78 μm depth resulted in a 4 μm resist consumption, which yields a 1:20 photoresist-silicon etch selectivity. A similar selectivity was obtained also in Figure 2.9 (b).

The selectivity of this process is reported in Table 2.3, together with its etch rate per cycle. The etch rate of course depends on the etching steps duration (Figure 2.9 (a) yields 180 nm/cycle, while Figure 2.9 (b) yields only 100 nm/cycle). These etch rates would probably be too low for an industrial production environment, but are not problematic for an academic context such as ours. The photoresist-silicon selectivity is, however, particularly important for some of the applications reported in the following chapters. For example, the contour lithography fabrication technique (see section 4.6.1), which is used to fabricate the devices of Chapter 4 and Chapter 6, require high aspect ratio trenches (>1:20) having 80 μm depths. For that purpose, the selectivity of the baseline recipe would require resist thicknesses greater than 5 μm. With such thick photoresist layer, resolution of small (~ 1 μm) features during photolithography becomes highly challenging.

Table 2.3: Performances of the baseline etching recipe reported in Table 2.2.

Etch rate (nm/cycle)	100-180
Photoresist-silicon etch selectivity	1:20

We therefore attempted to optimize the baseline recipe reported in Table 2.2 to obtain a higher photoresist-silicon selectivity. This goal appeared particularly achievable since ICP equipment manufacturers, photoresist suppliers, and academic publications [46, 48] routinely report selectivities up to 1:50. In section 2.2.4, the main parameters of the basic recipe reported in Table 2.2 are explained, analysed, and varied in order to maximize selectivity.

2.2.4 Influence of the main process parameters

Operating pressure, ICP power, etching gas (SF_6) flow

These three parameters are correlated, in proportions that vary as a function of the etching chamber dimensions. For any chosen operation pressure, and for given chamber dimensions, there is an optimal ICP power and SF_6 gas flow. For initial process development, one usually chooses a desired operation pressures and then optimizes ICP power and SF_6 gas flow to reach

the highest possible etch rate. We assume that such optimization was carried properly, at 15 mTorr, for the process reported in Table 2.2.

15 mTorr is a relatively low pressure compared to what is typically reported [48] for ICP etching. Low pressure minimizes the amount of collisions that the free radicals undergo on their path toward the substrate. Less collisions yield ions of higher energy, which can increase etch mask erosion and decrease selectivity. However, lower pressure operation was also previously reported to allow very high aspect ratio etching by maximising mass transport at the bottom of very narrow trenches [37]. For this reason, we choose not to change the pressure and to target other parameters for the optimization of the etch mask selectivity.

Etching/passivation step time ratio

As discussed in section 2.2.3, the ratio between etching and passivation step durations affects the profile of the fabricated trenches. Longer etch durations, or smaller passivation durations, tend to produce re-entrant profiles (i.e., trenches having widths that increase as a function of depth). However, as aspect ratio increases, only ions with an almost perfect vertical trajectory reach the bottom of the trenches, which tends to make the profiles vertical again. This phenomenon is well illustrated in Figure 2.10, where the passivation step duration was decreased from 4 seconds (for the baseline recipe) to 3 seconds. The top part of the trenches (i.e.: the first ~10 μm) is re-entrant. However, at depths > 10 μm, the profile becomes vertical. For depth > 40 μm mass transport at the bottom of the trenches becomes very limited and the profile becomes tapered. Interestingly, the zone where the profile is vertical (10 μm < depth < 40 μm) corresponds to the zone of optical interaction for all the free-space interferometers presented in the next chapters (Chapter 4 - Chapter 6). Therefore, for high aspect ratio trenches, reducing passivation time yields trenches with acceptable profiles for our optical applications.

In Figure 2.10, decreasing passivation step duration from 4 to 3 seconds increased the etch rate from 180 nm/cycle to 220 nm/cycle compared to the original recipe. Etching more silicon per cycle, while decreasing the cycle duration by 1 second, decreased the overall process time and reduced physical erosion of the etch mask due to ion bombardment. Selectivity was consequently increased from 1:20 (Table 2.3) to 1:25. This improvement is however modest compared to our

goal to reach the typical selectivity (1:50) reported by equipment manufacturers. Further optimisation of other process parameters was therefore carried.

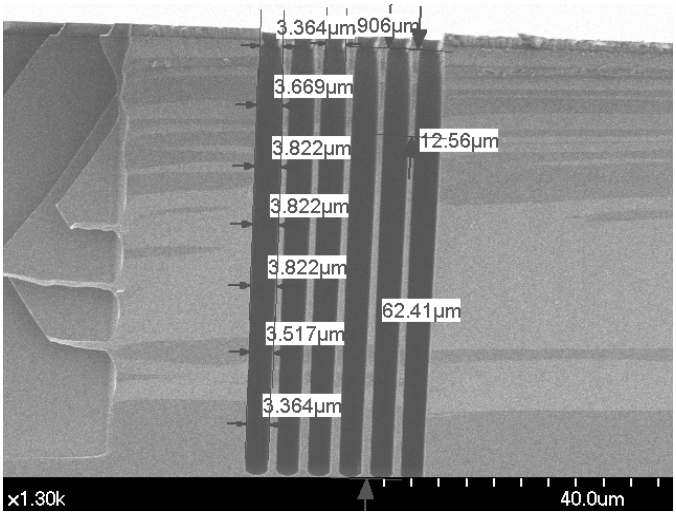

Figure 2.10: Cross section view of test structures etched using 410 cycles of the recipe reported in Table 2.2, but by reducing the passivation cycle time from 4 to 3 seconds. The top 10 µm of the profile is re-entrant but then becomes vertical at higher depths when the aspect ratio increases.

CCP power

As discussed in section 2.2.2, the power of the capacitive coupled plasma (CCP) is linked to the ion angular distribution (IAD) and the energy of the radicals impacting the substrate. Decreasing CCP power during the etch steps can therefore minimize physical erosion of the etch mask due to ion bombardment, thus increasing the etch selectivity. However, as CCP power decreases, the ion angular distribution gets wider, which can affect the verticality of the etched trenches. We therefore decreased CCP power to improve selectivity until the etch profile became unacceptably non-vertical.

In Figure 2.11, the photoresist-silicon etch selectivity and the silicon etch rate per cycle are reported as a function of CCP powers that range from the original value of Table 2.2 (25 W) down to 18 W. The etching and passivation step durations are respectively 6 and 3 seconds, as in Figure 2.10. Reducing CCP power down to 18 W allowed only a very modest increase of the

selectivity from 1:25 to 1:27.3, at the expense of a decreased etch rate (from 220 nm/cycle to 180 nm/cycle). Optimization of other process parameters therefore needs to be performed. Reducing CCP power below 18 W is not an option since, as shown in Figure 2.12, the portions of the trenches that present a vertical profile is now reduced to approximately 10 μm < depth < 30 μm. Reducing CCP power further would affect verticality even more importantly, which could significantly affect the targeted optical applications.

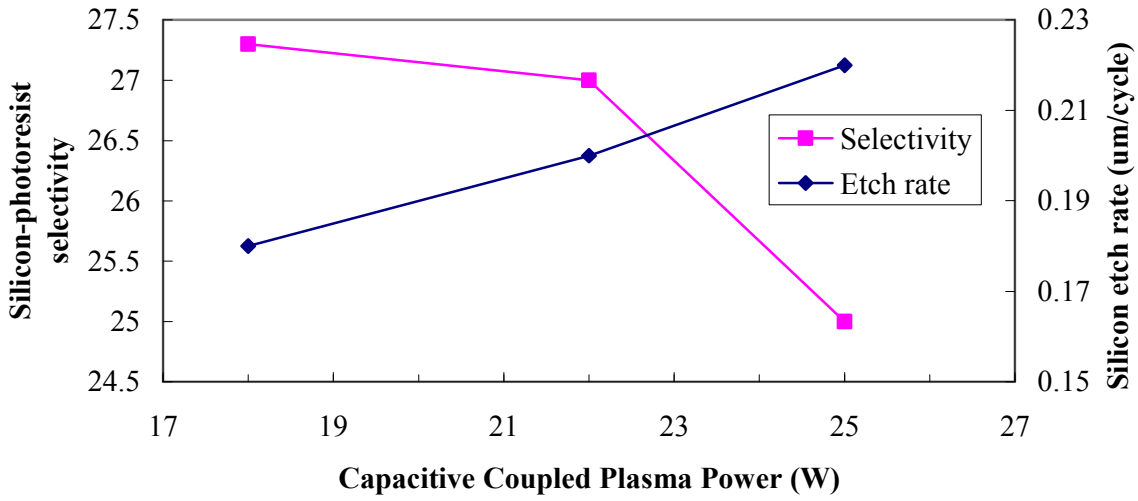

Figure 2.11: Silicon-photoresist etch selectivity and silicon etch rate per cycle as a function of the Capacitive Coupled Plasma (CCP) power. The other parameters are the same as in Table 2.2, except for the etching and passivation step durations (6 sec. and 3 sec., as in Figure 2.10).

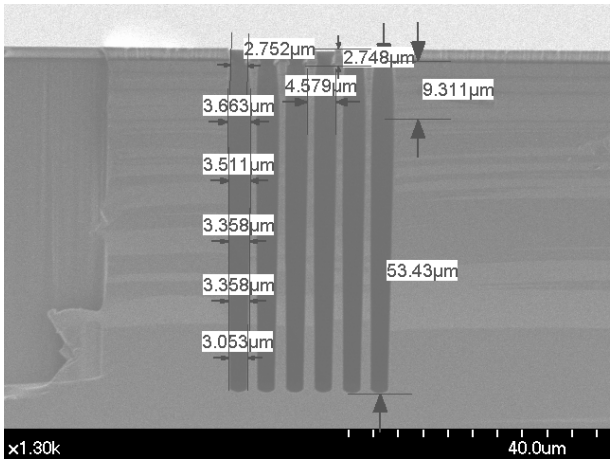

Figure 2.12: Cross section view of test structures etched using 350 cycles of the recipe reported in Table 2.2, but by reducing the passivation cycle time from 4 to 3 seconds and by reducing CCP power from 25 W to 18 W.

Substrate temperature

One of the main advantages of processes relying on C_4F_8 inhibitor (as opposed to cryogenic etching that rely on O_2) is that the etching and passivation chemistries are relatively insensitive to the substrate temperature [46]. Substrate temperature can therefore be varied without substantially affecting the etch rate and the trench profiles.

Decreasing substrate temperature can potentially benefit the photoresist-silicon selectivity. As reported in [48], lower temperatures tend to make photoresists more resistant to physical erosion due to ion bombardment. We therefore chose to decrease the original process (Table 2.2) temperature from 20 to 0 °C. The only drawback of such approach is the higher liquid nitrogen consumption required to keep the substrate at 0 °C during etching.

Inhibitor gas flow during the etch steps

As described in section 2.2.2, inhibitor gas (C_4F_8) is required—even during the etch steps of time multiplexed processes—in order to prevent IAD and IF effects (Figure 2.7). For example, as seen in Figure 2.13, removing C_4F_8 completely during the etch steps of the baseline recipe yields non-vertical trenches that are unusable for photonic applications. However, removing C_4F_8

completely during the etch steps also dramatically increased the etch rate to 540 nm/cycle (compared to 220 nm/cycle for the baseline recipe). This higher etch rate per cycle resulted in an even more dramatic improvement of the selectivity from 1:20 to 1:70.

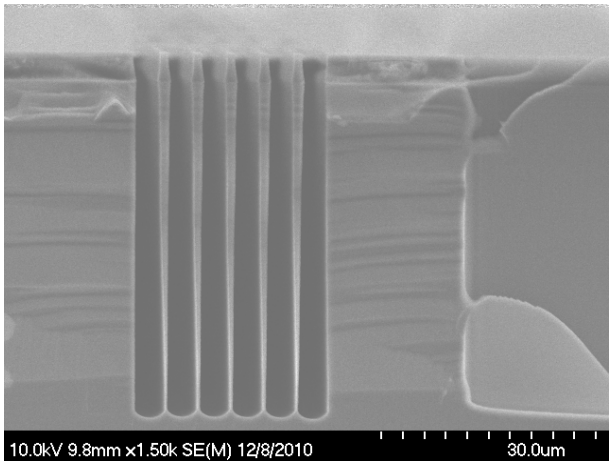

Figure 2.13: Cross section view of test structures etched using 160 cycles of the basic recipe reported in Table 2.2 (6 s etch, 4 s passivation), but by removing completely the inhibitor gas (0 sccm C_4F_8) during the etch steps. Strong IAD effect causes non-vertical profiles that are unusable for photonic application.

Reducing the C_4F_8 flow rate during the etch steps therefore appears as a promising avenue to improve the etch selectivity of our process. We kept the modification listed above for CCP power (18 W) and etch temperature (0 °C), and then reduced C_4F_8 flow rate as much as possible (i.e.: as long as the etch profile remained vertical). The best results were obtained with a C_4F_8 flow rate reduced from 15 to 4 sccm, and are presented in Figure 2.14. In this case, the etch rate increased to 283 nm/cycle while the photoresist-silicon etch selectivity reached 1:53.

2.2.5 Higher selectivity recipe for narrow, high aspect ratio trenches

The parameters of the optimized recipe developed in section 2.2.4 (and used in Figure 2.14) are reported in Table 2.4. This recipe allowed a significant increase of the photoresist-silicon selectivity from 1:20 (Table 2.3) to 1:53 (Table 2.5) while maintaining nicely vertical profiles in high aspect ratio trenches. The optimized recipe however has an important limitation compared to the baseline process. Selectivity improvement was achieved mainly by reducing the C_4F_8 inhibitor gas flow during the etch steps. Consequently, as shown in Figure 2.15, larger features suffer from important image force (IF) effect that make them unusable for photonic applications. This optimized recipe will therefore be used only for narrow trenches (i.e., deep-etched multilayer mirrors) that are fabricated separately from larger features (i.e., optical fiber alignment grooves, microfluidic systems). More specifically, the optimized recipe will be used for the devices presented in Chapter 4 and Chapter 6, while the baseline recipe will be used for the devices presented in Chapter 5 and Chapter 7.

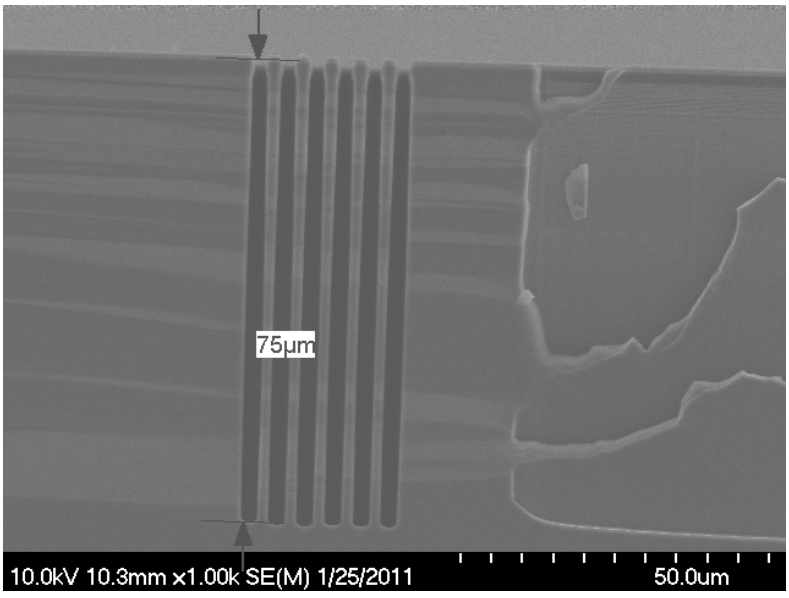

Figure 2.14: Cross section view of test structures etched using 425 cycles of the final recipe optimized for narrow high aspect ratio trenches (Table 2.4).

Table 2.4: High selectivity recipe for narrow high aspect ratio trenches.

	Etching step	Passivation step
ICP Power (W)	450	450
CCP Power (W)	18 (25*)	10
SF_6 flow rate (sccm)	65	0
C_4F_8 flow rate (sccm)	4 (15*)	65
O_2 flow rate (sccm)	6	0
Temperature (°C)	0 (20*)	0 (20*)
Pressure (mTorr)	15	15
Step time (s)	6	4 (3*)

*Original parameter of the baseline recipe (Table 2.2)

Table 2.5: Performances of the etch recipe reported in Table 2.4.

Etch rate (nm/cycle)	283
Photoresist-silicon etch selectivity	1:53

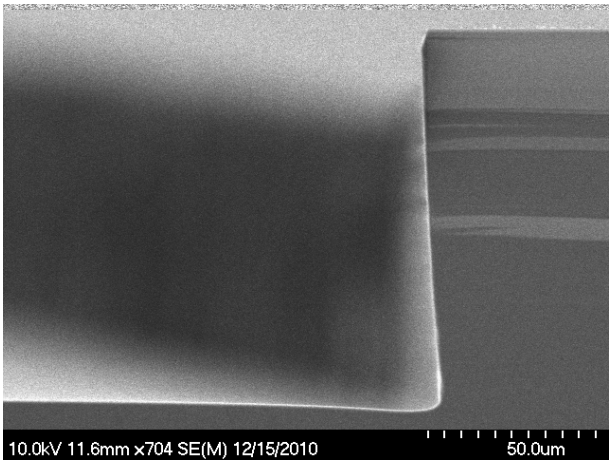

Figure 2.15: Cross section view of a wide opening test structure fabricated using the recipe optimized for narrow high aspect ratio trenches (Table 2.4). Strong image force (IF) effect occurs as a consequence of the reduced inhibitor gas concentration during the etch steps. This optimized recipe is therefore usable only for narrow high aspect ratio trenches, as in Figure 2.14.

2.3 Technological limitations

2.3.1 Overview

Fabricating deep-etched multilayer optical resonators by inductively coupled plasma etching induces several imperfections, which prevent the resulting mirrors to yield the ideal properties described in section 2.1. These imperfections are schematized in Figure 2.16.

Firstly, as the aspect ratio of the etched trenches is limited to 1:30, the required etch depth, for a given design, imposes a minimum value to the m_{Air} layer order, which restricts the mirror bandwidth (see in Figure 2.3). However, for all the devices presented in the current work, small enough layer thicknesses always allowed reflection bandwidth larger than 100 nm. Such bandwidth allows coverage of the entire conventional (C) telecommunication band (1530 nm - 1570 nm) and is also more than sufficient for sensing applications.

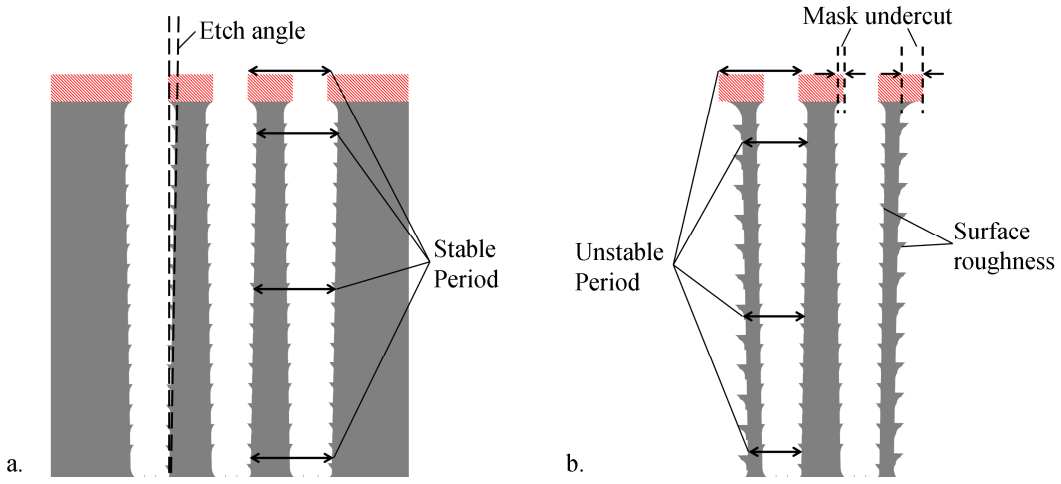

Figure 2.16: Schematic representation of a 2.5 periods deep-etched silicon-air multilayer mirrors suffering from mask undercut, surface roughness, and imperfect verticality. The importance of these imperfections depends on the dimension of the opening defined by the photomask. (a) With silicon as the incidence and output medium (e.g. waveguided interferometers), all the layers of the multilayer mirror can be assumed to have the same dimensions, etch angles, and surface roughness, which yield more predictable optical characteristics. (b) With air as the input and output medium (e.g. free-space interferometers) these imperfections are different for the layers facing the larger openings, which results in less predictable characteristics.

Secondly, each silicon-air material interface will present surface roughness, which will cause light scattering and reduce mirror reflectivity. As presented in Figure 2.16, the amount of surface roughness varies as a function of the width of the etched trenches. In larger trenches, ions having non-vertical trajectories are free to impact the etched sidewalls, causing more strongly defined scalloping. On the opposite, only ions having nearly vertical trajectories can penetrate high aspect ratio trenches. Surface scalloping is therefore typically much less important as the aspect ratio increases [49]. However, as will be presented in Chapter 4, high aspect ratio trenches still present important amounts of random, low spatial frequency roughness which strongly contribute to light scattering. In Chapter 4, measurements of surface roughness in typical deep-etched trenches will be presented. A theoretical model that account for surface roughness will also be proposed and will be demonstrated to correspond remarkably well with the experimental results. In section 4.5 of Chapter 4, a review of etching techniques that were optimized to yield high surface quality sidewalls will be presented.

Thirdly, even if careful optimisation of the etching recipe is carried, the profile of the etched trenches can never be perfectly vertical. In Chapter 4 (section 4.9.2) the effect of imperfect verticality will be discussed in the context of free-space deep-etched Fabry-Perot resonators. Imperfect verticality will be demonstrated to be a potentially important source of insertion losses and finesse reduction. However, measurement of typical etches angles will be performed and will demonstrate that, in the current work, surface roughness rather than imperfect verticality is the dominant source of loss and peak broadening.

Lastly, as schematized in Figure 2.16, imperfect verticality and mask undercut will change the thickness of the layers, compared with the dimensions that were originally designed. As described in the following section, these variations of the layer thicknesses can strongly affect the mirrors reflection spectra.

2.3.2 Unpredictable layer dimensions

As shown in Figure 2.16, the fabricated dimensions of each layer inside deep-etched mirror can be very different than the ideal dimensions that were designed on the photomask. These variations will typically yield optical spectra that are different than what can be expected from simulations based on ideal (m_{Si}, m_{Air}) layers dimension (section 2.1).

Dimension variations are more predictable for mirrors that use silicon as the incidence and output medium (e.g., Figure 2.16 a). In this case, all the trenches have the same initial widths and can therefore be assumed to suffer from the same dimension variations upon fabrication. The silicon-air period that is designed on the photomask is therefore a constant (see Figure 2.16 a) that does not change during fabrication (i.e., increases of the air layer thicknesses translate in equivalent decreases of the silicon layer thicknesses, such that the period is constant). Because of this stable period, there is only one unknown—i.e, the width of the air trenches—to consider during mirror design[3]. In Figure 2.17, the reflectivity spectrum of a mirror having (m_{Si}, m_{Air}) = (17, 5) nominal dimension (i.e. a 3.83 μm fixed silicon-air period) is presented as a function of the error on the air layer thickness. This mirror is based on 2.5 periods, as in Figure 2.2. When no thickness variation occurs, the reflection bandwidth is centered at λ_c = 1550 nm, as in the ideal case (see Figure 2.2). For small variations (± 100 nm) of the air layer thickness, the peak reflectivity value and the bandwidth are essentially constant, and the central wavelength (i.e., the central position of the bandwidth) shifts slightly between 1500 nm and 1600 nm.

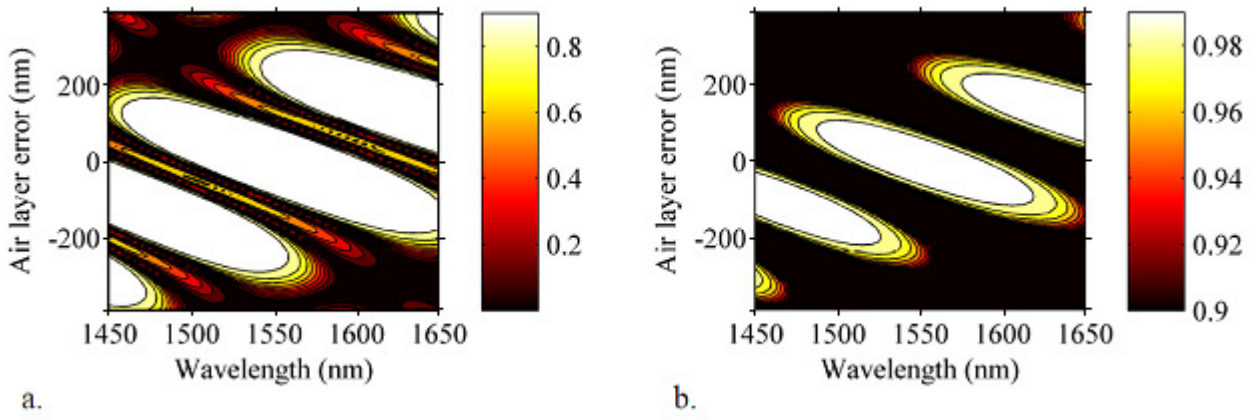

Figure 2.17: (a) Simulated reflectivity spectrum of a (m_{Si}, m_{Air}) = (17, 5) mirror as a function the fabrication error on the air layer thickness. The incidence and output medium is silicon, such that each of the 2.5 silicon-air period has an invariable length (3.83 μm), as in Figure 2.16a. (b) Same simulation but different color scale to highlight the zones of high (> 90%) reflectivity.

[3] Imperfect verticality of the etch profiles will also cause losses at resonance when multilayer mirrors are assembled to create interferometers. This case will be detailed in section 4.9.2.

In order to achieve predictable optical characteristics upon fabrication, we typically fix the silicon-air period for all the devices included on a given photomask. For this fixed period, we design several air layer thicknesses to ensure that some of the fabricated devices will have dimensions falling within the ± 100 nm margin outlined in Figure 2.17. This approach will be used for the interferometers presented in Chapter 4, Chapter 6, and Chapter 7.

On the contrary, when air is used as the incidence and output medium, the dimensions—and thus the reflection spectra—of deep-etched multilayer mirror can be highly unpredictable. As show in Figure 2.16, the silicon layers facing larger openings can be thinner than the inner silicon layer, due to more important mask undercut during etching. There is therefore several unknowns to consider during photomask design (e.g., mask undercut in large vs. narrow trenches, optical diffraction during photolithography in large vs. narrow openings, etch angle, etc.) such that predictable characteristics are not achievable. However, it is still possible to obtain good optical properties, fortuitously, simply by testing several devices that suffered from different dimension variations. For example, in Figure 2.18, simulated reflection spectra of a (m_{Si}, m_{Air}) = (17, 5) reflector having 2.5 silicon-air periods are performed for various mask undercut values. In Figure 2.18 (a), typical undercut values of 550 nm in large trenches, and 250 nm in narrow trenches are considered. In this case, no useful reflection band occurs in our targeted wavelength range (1500 nm - 1600 nm). However, In Figure 2.18 (b), changing slightly the narrow trench undercut value, from 250 nm to 320 nm, yields a useful reflection band centered at 1550 nm with a peak reflectivity greater than 99%. In fact, for any undercut value, a useful reflection band always occurs, but not always at the desired wavelength (for example, in Figure 2.18 (a), a useful reflection band occurred around λ = 1400 nm).

In brief, by including several dimensions variations on a given photomask, reflection bands centered on a desired wavelength (1550 nm in our case) can be achieved. This approach was successfully used for our early work on refractive index sensors (Chapter 5) and also in our previous work on tunable filters [21]. The main drawbacks of this approach are a low and unpredictable yield, and the need to characterize each device individually before use. For this reason, in Chapter 4 (section 4.6.1), a method for the fabrication of free-space interferometers

(e.g. Figure 2.16 b) having the dimension predictability of waveguided (e.g. Figure 2.16 a) interferometers will developed.

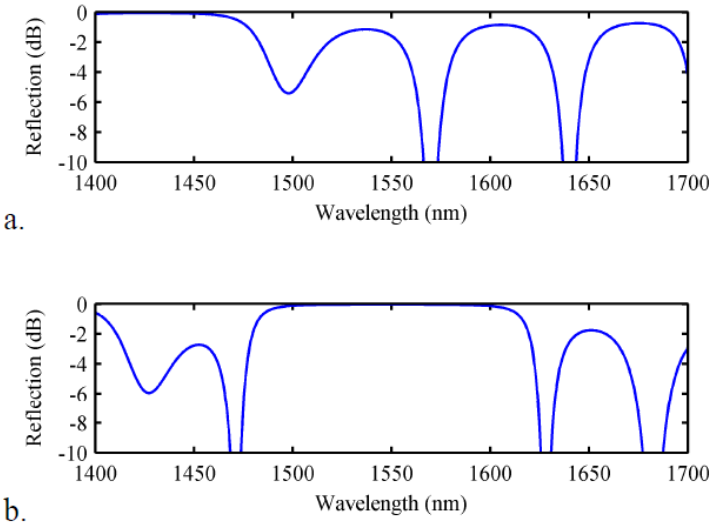

Figure 2.18: Simulated reflectivity spectra of a 2.5 periods, (m_{Si}, m_{Air}) = (17, 5) reflector for various mask undercut value. The incidence and output medium is air, such that the final dimension of each layer is unpredictable, as in Figure 2.16b. (a) With typical undercut values of 550 nm in the larger trenches and 250 nm in the narrower trenches, no useful reflection band occurs in the targeted 1500 nm - 1600 nm range. (b) With slightly different values (550 nm in larger trenches, 320 nm in narrower trenches) a useful reflection band occurs at λ_c = 1550 nm.

CHAPTER 3 IN-PLANE INTERFEROMETERS BASED ON DEEP-ETCHED SILICON-AIR MULTILAYER REFLECTORS

In the next chapters, deep-etched silicon-air multilayer reflectors will be used to create in-plane optical interferometers. The current chapter presents the ideal properties of such interferometers, followed by a summary of the main results that will be presented.

3.1 Free-space Fabry-Perot interferometers

3.1.1 Basic ideal properties

We define free-space interferometers as devices that do not confine light in the transverse dimension (as opposed to the waveguided interferometers that will be presented in section 3.2). These free-space interferometers will be used mainly as sensors (Chapter 5, Chapter 6). Consequently, the material filling the gap between the two mirrors is initially air, such that samples (liquids or polymers) can subsequently be admitted into the cavity.

A typical deep-etched etched free-space Fabry-Perot interferometer is schematized in Figure 3.1. The distance (L) between the two mirrors forming the cavity is defined as in Eq. (3.1) using a notation similar to the one used for the thickness of the layers forming the Bragg mirrors (see Chapter 2, Figure 2.1).

$$L = \frac{m_{Gap}\lambda_c}{2n_{Gap}} \tag{3.1}$$

As in Chapter 2, we always use λ_c = 1550 nm as our targeted central wavelength of operation. For design purposes, we also consider that air is filling the gap between the mirrors, such that $n_{Gap} = n_{Air} = 1.0003$ [3]. In that case, Fabry-Perot resonance is expected to occur at λ_c for cavity lengths of an integer multiple (m_{Gap}) of $\lambda_c/2n_{Gap}$ = 775 nm. In the current chapter, we will refer to our deep-etched free-space Fabry-Perot interferometers using a notation that include m_{Gap}, and also the odd integers multiple of the silicon and air layers forming the multilayer mirrors: (m_{Si}, m_{Air}, m_{Gap}).

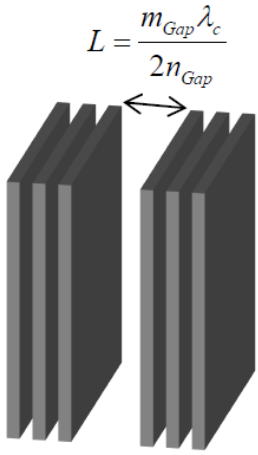

Figure 3.1: Schematic representation of a deep-etched free-space Fabry-Perot interferometer labelled using the notation (Eq. (3.1)) defining the cavity length (L).

The simulated ideal transmission spectrum of a Fabry-Perot interferometer, based on 2.5 silicon-air periods per mirror and having dimensions constants (m_{Si}, m_{Air}, m_{Gap}) = (17, 5, 50), is presented in Figure 3.2. This simulation considers a perfectly lossless system and is performed using the same transfer matrix formalism [34] that was also used for individual Bragg mirrors in Chapter 2. As expected, a sharp Fabry-Perot resonance peak occurs at λ_c = 1550 nm. Within the bandwidth of the mirrors (approximately 105 nm for (m_{Si}, m_{Air}) = (17, 5) mirrors, see Figure 2.3), two other resonance peaks are also visible on each side of the central resonance wavelength. The wavelength separation between adjacent peaks is defined as the Free Spectral Range (FSR).

The FSR of Fabry-Perot interferometers is usually expressed as a function only of the wavelength of operation (λ_c in our case) and of the optical path length between the mirrors ($n_{Gap}L$ in our case) through the following relation [51]:

$$FSR_{Ideal} = \frac{\lambda_c^2}{2n_{Gap}L} = \frac{\lambda_c}{m_{Gap}} \tag{3.2}$$

However, this relation does not account for the phase shift (see Figure 2.2 b) experienced by light upon reflection on the Bragg mirrors. For cavities that are very long compared to the thickness of the mirrors, this phase shift is usually negligible and Eq. (3.2) yields accurate predictions. In our case, however, the length of the cavity can be on the same order of magnitude as the thickness of

the mirrors. The effective cavity length can therefore be significantly greater than its actual length (L), such that Eq. (3.2) can greatly overestimate the FSR.

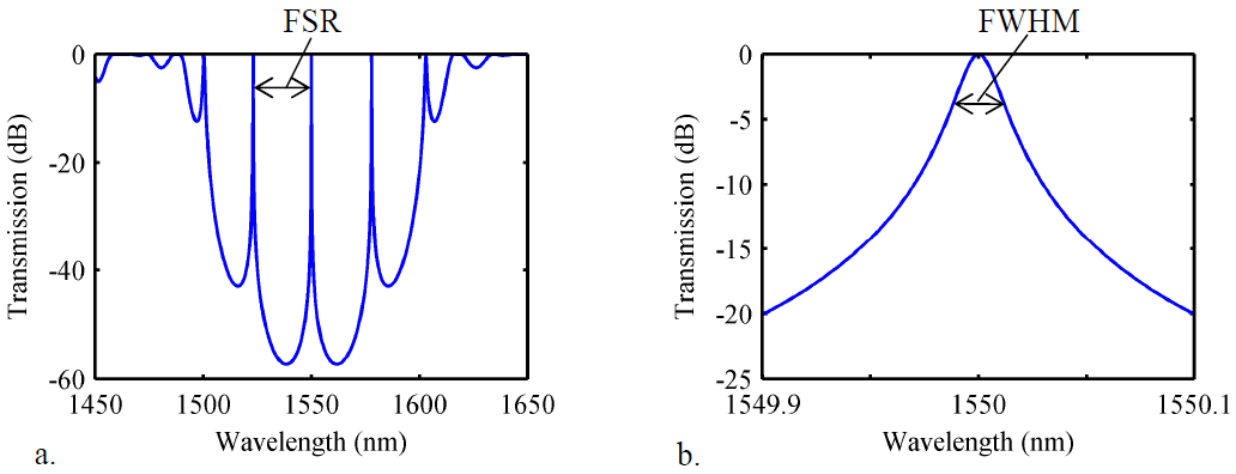

Figure 3.2: (a) Ideal transmission spectrum of a (m_{Si}, m_{Air}, m_{Gap}) = (17, 5, 50) free-space Fabry-Perot interferometer based 2.5 silicon-air periods mirrors. The Free Spectral Range (FSR) between adjacent resonance peaks is labelled. (b) Magnified view of the resonance peak centered on λ_c = 1550 nm. The full width at half maximum (FWHM) of the peak is labelled.

This difference between the ideal FSR, calculated using Eq. (3.2), and the effective FSR ($FSR_{Effective}$) is outlined in Figure 3.3. The effective FSR is obtained by inspection of the transfer matrix simulations, which still consider a Fabry-Perot cavity having (m_{Si}, m_{Air}) = (17, 5) mirrors of 2.5 silicon-air periods. For very small interferometer path lengths ($n_{Gap}L$), the difference between FSR_{Ideal} and $FSR_{Effective}$ can reach almost one order of magnitude. As the path length increases, the phase shift upon reflection becomes negligible compared to the cavity length, such that $FSR_{Effective}$ can be accurately obtained from the FSR_{Ideal} equation (Eq. (3.2)). The behaviour outlined in Figure 3.3 can also be observed, in different proportions, with interferometers based on mirrors having different (m_{Si}, m_{Air}) dimensions and number of Bragg periods (P). Larger (m_{Si}, m_{Air}) dimensions decrease the effective FSR due to the larger effective thickness of the mirrors. On the other hand, the number of Bragg periods (P) in each mirror is found to have very little influence on the expected effective FSR.

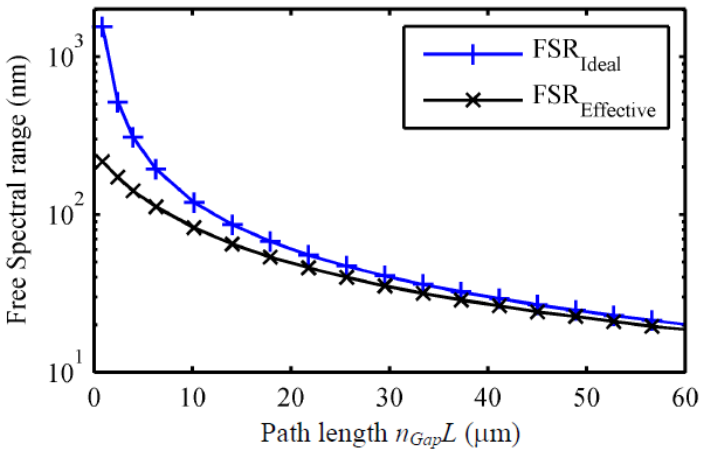

Figure 3.3: Free spectral range of a Fabry-Perot interferometer as a function of the optical path length between the mirrors. For short path lengths, the thickness of the mirrors is not negligible compared to the mirror separation, such that the ideal FSR relation (Eq. (3.2)) greatly overestimates the actual FSR (i.e.: $FSR_{Effective}$, obtained from the transfer matrix simulation). The interferometer is based on (m_{Si}, m_{Air}) = (17, 5) Bragg mirrors of 2.5 silicon-air periods.

The Finesse ($\mathfrak{F}$) is certainly the most widely acknowledged parameter used to quantify the optical quality of Fabry-Perot interferometers, and is therefore the figure of merit that will be used throughout the current work. It is possible to show [52] that the Finesse is proportional (see Eq. (3.3)) to the number of roundtrips (N_{RT}) that light undergoes before exiting the optical cavity (more precisely, N_{RT} is the number of roundtrips after which a fraction ($1 - |e|^{-1}$) of photons have left the cavity).

$$\mathfrak{F} = 2\pi N_{RT} . \tag{3.3}$$

The finesse therefore quantifies the light confinement ability of Fabry-Perot resonators. Interestingly, this parameter does not necessarily have to be measured in the time domain (which is possible but typically requires dedicated setups [52]), but can be obtained directly in the spectral domain using:

$$\mathfrak{F} = \frac{FSR_{Effective}}{FWHM} , \tag{3.4}$$

where FWHM is the full width at half maximum of the resonance peaks (see Figure 3.2 b).

For ideals (i.e.: no sources of loss considered) Fabry-Perot interferometers, the only way for light to exit the cavity is by transmission through the mirrors. The predicted finesse [51] is therefore function only of the reflection (R) and transmission coefficients (T=1-R) of the mirrors:

$$\Im = \frac{\pi\sqrt{R}}{1-R}. \tag{3.5}$$

We saw in Chapter 2 (Table 2.1) that the ideal reflectivity of silicon-air multilayer reflectors depends only on the number of Bragg periods that constitute the mirrors. The ideal Finesse of deep-etched free space Fabry-Perot resonators is therefore also independent of the mirror and gap layer dimensions. We can consequently predict (see Table 3.1) the maximum theoretical finesses using only Eq. (3.5) and the ideal reflection coefficients reported in Table 2.1. These predictions are however highly hypothetical. As will be demonstrated in Chapter 4, and as summarized below in section 3.3.1, other sources of loss affect the finesse of our deep-etched Fabry-Perot resonators. Experimental finesses are therefore usually orders of magnitudes smaller than in Table 2.1.

Table 3.1: Maximum finesse vs. number of Bragg periods per mirror.

Number of Bragg periods (P)	Finesse ($\Im$)
1.5	1.15×10^2
2.5	1.39×10^3
3.5	1.68×10^4

3.1.2 Sensitivity to refractive index variations and mechanical deformations

In the current work, free-space Fabry-Perot interferometers will be used to detect refractive index (RI) variations and mechanical deformations. Changes of the refractive index (n_{Gap}), or the length (L), of the gap affect the optical path ($n_{Gap}L$) between the mirrors, which results into a shift of the interferometer resonance wavelength (λ_{Res}). For example, for the (m_{Si}, m_{Air}, m_{Gap}) = (17, 5, 50) interferometer presented in Figure 3.2, a $\Delta n = 5 \times 10^{-5}$ shift of the gap refractive index results into a $\Delta\lambda_{Res} = 0.07$ nm shift of the resonance wavelength (see Figure

3.4). We define the ratio between these two quantities ($\Delta\lambda_{Res}/\Delta n$) as the refractive index sensitivity of the interferometer, which is 1390 nm/RIU (Refractive Index Units) in Figure 3.4.

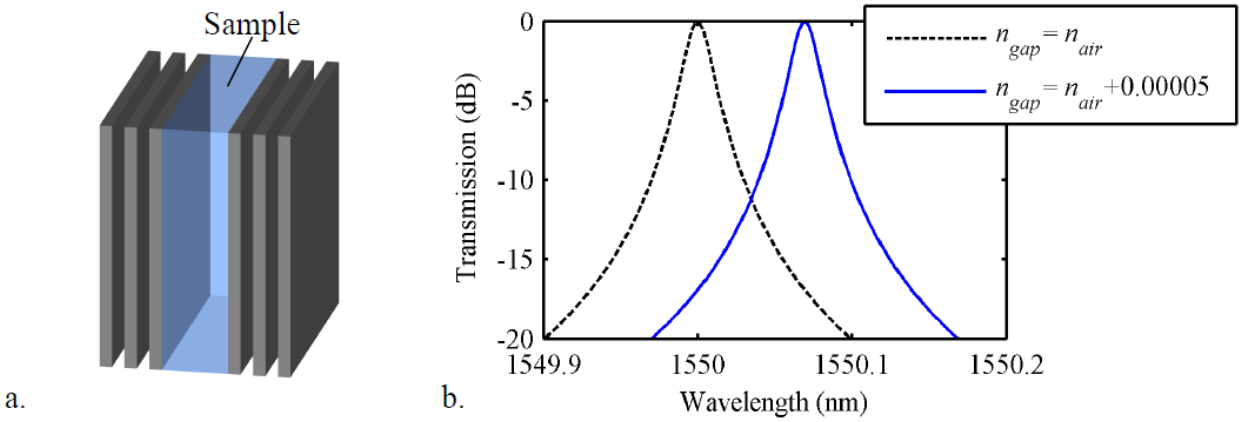

Figure 3.4: (a) Schematic representation of a deep-etched free-space Fabry-Perot interferometer filled with a sample to be characterized. (b) Simulated ideal transmission spectra of a Fabry-Perot interferometer filled with air and upon a $\Delta n = 5 \times 10^{-5}$ variation of the refractive index in the gap between the mirrors. The interferometer dimensions are the same as in Figure 3.2.

It is possible to demonstrate that—in the ideal case of mirrors that are very thin compared to the optical path length of the interferometer—the normalised displacement ($\Delta\lambda_{Res}$) of the resonance wavelength (λ_{Res}) as a function of refractive index changes in the gap is given by:

$$\left.\frac{\Delta\lambda_{Res}}{\lambda_{Res}}\right|_{Ideal} = \frac{\Delta n_{Gap}}{n_{Gap}}, \tag{3.6}$$

which can be rearranged to provide the ideal refractive index sensitivity (in nm/RIU):

$$\left.\frac{\Delta\lambda_{Res}}{\Delta n_{Gap}}\right|_{Ideal} = \frac{\lambda_{Res}}{n_{Gap}}. \tag{3.7}$$

Equation (3.7) means that the maximum theoretical RI sensitivity of any Fabry-Perot sensor can not exceed the ratio of the wavelength of operation over the refractive index of the sample. For

example, a sensor operating around $\lambda = 1550$ nm for the detection of RI variations in water-based solution ($n \sim 1.3$) would yield a maximum possible sensitivity of 1200 nm/RIU.

For Fabry-Perot resonators based on deep-etched multilayer reflectors, the effective RI sensitivity can be significantly lower than the ideal sensitivity predicted by Eq. (3.7). If the thickness of the mirrors is not negligible compared to the interferometer path length, the overlap between the sample and the resonant light mode will be significantly smaller than unity. Non-negligible mirrors thickness will therefore decrease the effective RI sensitivity, in the same way as it decreased the free-spectral range of the interferometer (see Figure 3.3). In fact, it is possible to show, analytically [51] or simply by inspection of transfer matrix simulations, that the effective refractive index sensitivity is proportional to the ratio of the ideal and effective FSR:

$$\left.\frac{\Delta\lambda_{Res}}{\Delta n_{Gap}}\right|_{Effective} = \frac{\lambda_{Res}}{n_{Gap}} \frac{FSR_{Effective}}{FSR_{Ideal}}. \tag{3.8}$$

In Figure 3.5, the refractive index sensitivity of a typical free-space Fabry-Perot interferometer is reported as a function of the optical path length between the mirrors. The mirrors are still considered to have 2.5 silicon-air periods each and (m_{Si}, m_{Air}) = (17, 5) dimension constants. When the path length is 40 μm or more, the expected refractive index sensitivity reaches 90% of its maximum possible value. As we will use free space Fabry-Perot interferometers to characterize liquids and polymers having refractive indices in the 1.3-1.45 range, a 40 μm path length corresponds to a mirror separation $L \sim 30$ μm. Increasing further the mirror separation would allow only a modest increase of the refractive index sensitivity, at the expense of higher insertion losses caused by Gaussian beam divergence. We will therefore use mirror separations of roughly 30 μm for all the refractive index sensing applications presented in the next chapters.

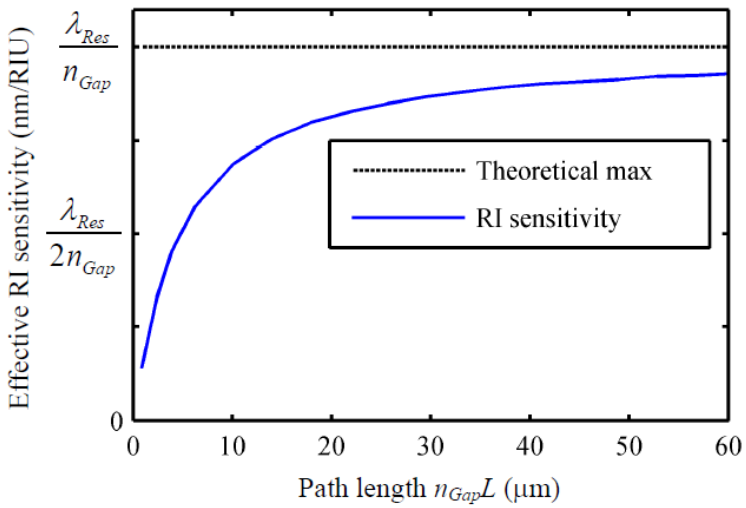

Figure 3.5: Refractive index sensitivity of a typical free space Fabry-Perot interferometer, as a function of the optical path length between the mirrors. The mirrors are considered to have 2.5 silicon-air periods each and (m_{Si}, m_{Air}) = (17, 5) dimension constants.

It is possible to demonstrate that the sensitivity of free-space Fabry-Perot interferometers to mechanical deformations (ΔL) follows exactly the same formalism as presented above for refractive index variations (Δn_{Gap}). Equations (3.6)-(3.8) can therefore be used to predict the interferometer response to mechanical deformations simply by replacing "n_{Gap}" and "Δn_{Gap}" by "L" and "ΔL". In particular, the expression of the effective mechanical deformation sensitivity rewrites as:

$$\left.\frac{\Delta\lambda_{Res}}{\Delta L}\right|_{Effective} = \frac{\lambda_{Res}}{L}\frac{FSR_{Effective}}{FSR_{Ideal}}. \tag{3.9}$$

Equation (3.9) indicates that the resonance wavelength shift ($\Delta\lambda_{Res}$) caused by a given change of the interferometer length (ΔL) will be maximised for an initial cavity length (L) that is as small as possible. However, this condition does not accurately illustrate the type of mechanical deformation measurements that we will undertake in Chapter 6. In that case, the cavity will be functionalized with a gas absorbent polymer. Upon exposition to a given concentration of analyte in air (C_{air}), the cavity will expand with a relative magnitude ($\Delta L/L$) proportional to C_{air} (i.e. $\Delta L/L \propto C_{air}$). In other words, the parameter of interest in this case is the relative ($\Delta L/L$),

rather than absolute (ΔL) deformation of the interferometer. A more meaningful way to rewrite Eq. (3.9) is therefore:

$$\left.\frac{\Delta\lambda_{Res}}{\Delta L / L}\right|_{Effective} = \lambda_{Res}\frac{FSR_{Effective}}{FSR_{Ideal}}. \tag{3.10}$$

In that case, Eq. (3.10) indicates that the resonance wavelength shift ($\Delta\lambda_{Res}$) caused by a given relative change of the interferometer length ($\Delta L/L$) will be maximised when the ratio of the effective and ideal FSR is maximised (i.e. for $FSR_{Effective}/FSR_{Ideal} \rightarrow 1$). As discussed previously, and as depicted in Figure 3.3, this condition is met for interferometers of longer path lengths. It is possible to show that, exactly as for the refractive index sensitivity (Figure 3.5), a 40 μm interferometer path length yields a sensitivity that is 90% of the maximum theoretical value.

In summary, the sensitivity of deep-etched free space Fabry-Perot interferometers to refractive index variations (Δn_{Gap}) and to relative increases of their length ($\Delta L/L$) is maximized for interferometers of longer optical path lengths. For a 40 μm optical path length (i.e. an $L \sim 30$ μm mirror separation when characterizing samples having refractive indices in the 1.3-1.45 range) both sensitivities reach 90% of their maximum possible value. An $L \sim 30$ μm mirror separation will therefore be used for all the free space Fabry-Perot sensors presented in the following chapters. Using larger mirror separations would allow only a modest increase of the sensitivities, at the expense of more important signal losses due to Gaussian beam divergence.

3.2 Waveguided Gires-Tournois interferometers

3.2.1 Basic ideal properties

Gires-Tournois interferometers (GTIs) present several similarities with Fabry-Perot interferometers. Both consist of two mirrors, facing each other, and between which light is in resonance. The particularity of GTIs, compared to Fabry-Perot interferometers, is that these two mirrors have different reflectivities. More precisely, the back mirror of a GTI has a ~ 100% reflectivity, while the reflectivity of the entrance mirror can fixed to any value in the 0 - 100% range, depending of the targeted applications. Due to the very high reflectivity of the cavity back mirror, GTIs are, in the ideal case, all pass filters (i.e. filters that reflect all light, regardless of the wavelength). These interferometers are therefore used in reflection, as opposed to Fabry-Perot cavities that are used mainly as transmission filters. As will be described later in this section, at the resonance wavelengths, light reflected by GTIs suffers from important phase shifts (i.e. light is confined more strongly in the interferometer at the resonance wavelengths). These phase shifts (i.e. dispersion) can be tailored to compensate the chromatic dispersion in optical fiber telecommunication networks. Alternately, these phase shift can be used to create dispersive mirrors in Michelson-GTI bandpass filters such as interleavers.

In the present case, the GTI back mirror consists of a deep-etched multilayer reflector of several silicon-air periods (see Figure 3.6 a). As discussed in Chapter 2, in the ideal case, such mirror is expected to yield a reflectivity above 99.9% for numbers of Bragg periods greater than 3.5. The entrance mirror consists of a silicon-air material interface which, in the ideal case, yields a $|r| = 0.55$ Fresnel amplitude reflection coefficient. Between the two mirrors, light propagates in a single-mode rib waveguide, as opposed to the free-space propagation region used with our Fabry-Perot sensors. Such waveguided cavity limits Gaussian beam divergence losses, allowing much longer interferometers (e.g. $L > 1$ mm) than with free-space designs.

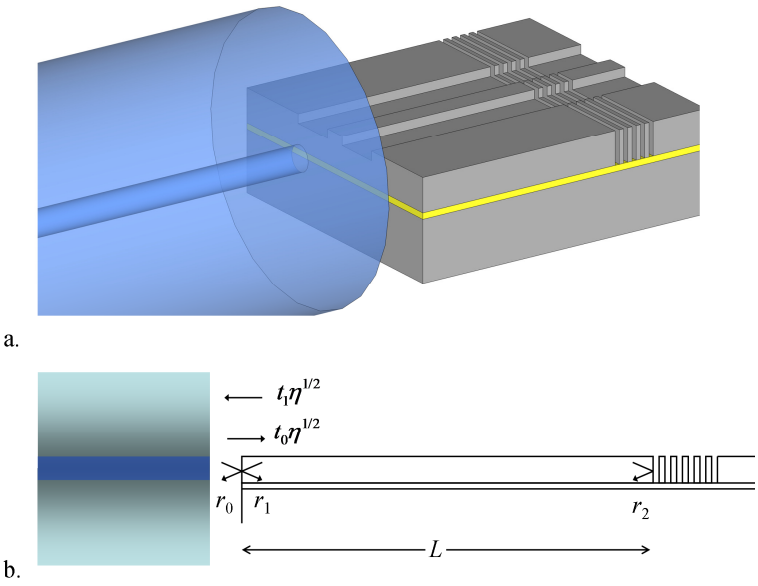

Figure 3.6: Schematic representation of the proposed waveguided Gires-Tournois interferometers. (a) 3D view. (b) Cross section view presenting the notation for the interferometer length, and for the amplitude coefficients of reflection and transmission at the two mirrors.

The amplitude reflection and transmission coefficients at each of the two mirrors of the GTI, are labelled in Figure 3.6 (b). Using this notation, it is possible to show that the overall amplitude reflectivity of the interferometer (r_{GT}) is given by:

$$r_{GT} = r_0 + \frac{\eta t_0 t_1 r_2 e^{-2i\beta L}}{1 - r_1 r_2 e^{-2i\beta L}}, \tag{3.11}$$

where $\beta = 2\pi n_{eff}/\lambda$ is the waveguide propagation constant and η is the fiber-waveguide intensity coupling efficiency. In the ideal case, the (r_0, r_1, t_0, t_1) coefficients are simply the normal incidence silicon-air Fresnel coefficients.

From the large refractive index contrast between silicon and the cladding materials (air and silicon oxide), and as we use large area single-mode waveguides of low numerical aperture, we expect the waveguide effective index (n_{eff}) to essentially match the refractive index of silicon ($n_{eff} \approx n_{Si}$). However, as shown in Figure 3.7, the refractive index of silicon presents strong wavelength dependence in the near-infrared region [2]. This material dispersion translates,

through Eq. (3.12), in a significant 3.6 % increase of the waveguide group index (n_g = 3.60) compared to the refractive index of silicon (n_{Si} = 3.48).

$$n_g = n_{Si} - \lambda \frac{dn_{Si}}{d\lambda} \tag{3.12}$$

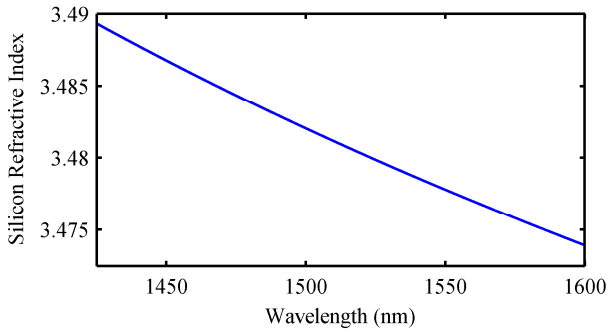

Figure 3.7: Wavelength dependence of silicon refractive index in the near-infrared.

The ideal amplitude reflection coefficient of the cavity back mirror (r_2) is calculated using the same plane wave transfer matrix formalism [34] as in Chapter 2. The thickness of the silicon and air layers are initially designed to 1.5 μm each, in order to yield the highest possible mirror reflection bandwidth, while remaining easily definable by contact lithography. As discussed in Chapter 2 section 2.3.2, the 3 μm silicon-air period remains invariant upon fabrication, even if the thickness of the air layers increases due to diffraction during photolithography or mask undercut during etching (see also Chapter 2, Figure 2.16 a). As shown in Figure 3.8 (a), for a 3 μm silicon-air invariant period, the cavity back mirror is expected to yield broadband high reflectivity—exceeding the conventional (C) 1530 - 1570 nm telecommunication wavelength range—for air layers thicknesses around 1.75 μm and 2 μm. For example, in Figure 3.8 (b), the amplitude reflection coefficient (r_2) is reported for a 1.78 μm air layers thickness (and a 3.0 μm silicon-air period), showing broadband high reflectivity (> 99.9%) exceeding the S and C wavelength ranges (1460 - 1570 nm). These dimensions (1.78 μm air layers, 1.22 μm silicon layers) correspond to what will be obtained experimentally in Chapter 7 and will therefore be used throughout the current section.

a.

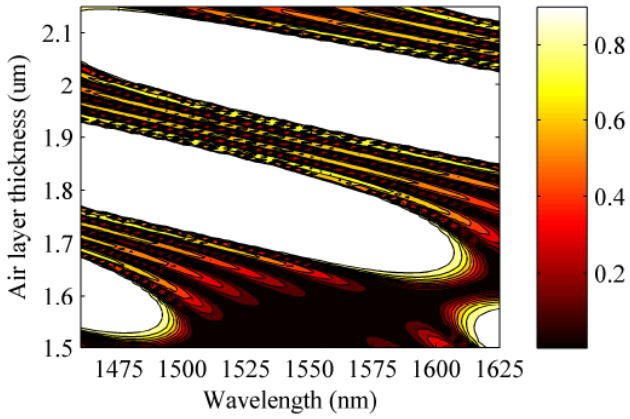

b.

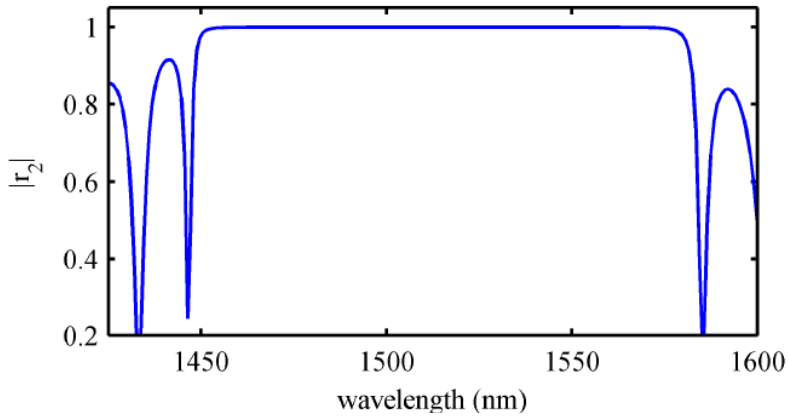

Figure 3.8: (a) Reflectivity of a 3.0 μm period silicon-air multilayer mirror (i.e.: the GTI back mirror) as a function of the air layers thickness. High reflectivity in the desired wavelength range is expected for air layers thicknesses around 1.75 μm and 2 μm. (b) Amplitude reflection coefficient of the cavity back mirror for 1.78 μm air layers thickness.

The geometry of the waveguide cross section is optimized to yield the highest possible fiber-waveguide coupling efficiency. We also limit ourselves to waveguides designs that respect the single-mode condition, in order to avoid unpredictable intermodal dispersion and polarization mode dispersion (PMD). Using the waveguide dimension notation presented in Figure 3.9 (a), the single mode condition [53] is given by:

$$\frac{w}{H} < \frac{h/H}{\sqrt{1-(h/H)^2}}. \tag{3.13}$$

In order to optimise waveguide dimensions, we first fix the thickness of the silicon-on-insulator device layer (H) to 11 μm in order to match the beam diameter of conventional single mode optical fibers ($2w_0$ = 10 μm) at λ = 1550 nm. More precisely, the device layer thickness (H) is slightly larger than the beam diameter ($2\omega_0$) to maximize light collection by the waveguide. It is possible to show that, with a H = 10 μm device layer, 5 % of the optical fiber mode power would be launched above or under the device layer, while a H = 11 μm layer loses only 2 % of the incident light. Once the H value is fixed, the w and h dimensions are varied in order to maximize fiber-waveguide coupling, while keeping the waveguide single mode.

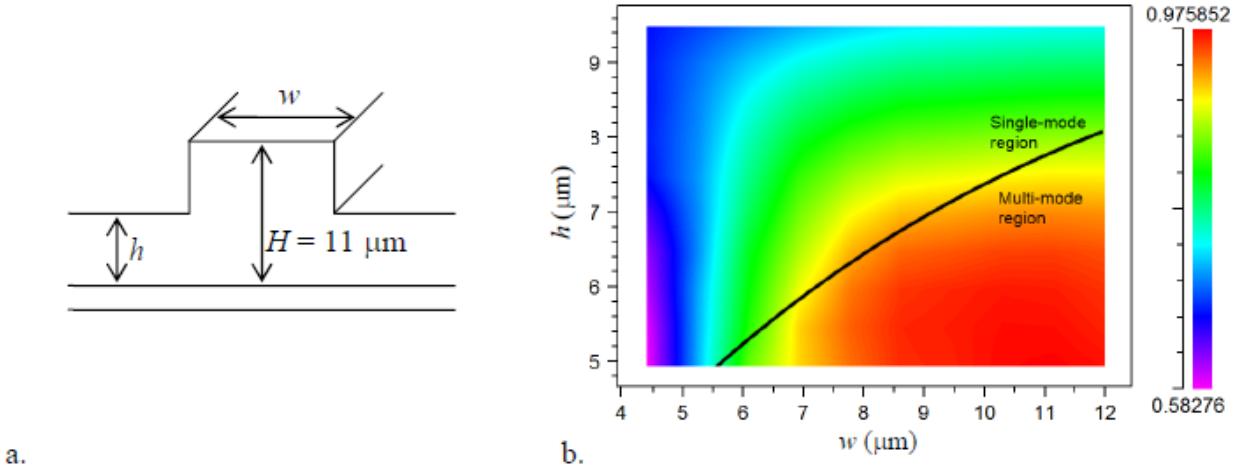

Figure 3.9: (a) Schematic representation of a RIB waveguide cross-section with the notation used to defined waveguide dimensions. (b) Simulated (beam propagation method) coupling efficiency between a silicon-on-insulator RIB waveguide and a conventional (8.2 μm diameter core) single-mode optical fiber. The waveguide height (H) is fixed (11 μm) while the width (w) and cladding height (h) are varied to optimise coupling efficiency. The black line indicates the waveguide single-mode condition.

In Figure 3.9 (b), the expected fiber-to-waveguide[4] coupling efficiency (η) is reported as a function of the w and h waveguide dimensions. The simulations are performed using the beam propagation method (BPM) mode solver of RSoft Photonics CAD suite. The best coupling efficiency, within dimensions that respect the single mode condition, is η = 0.8847 and is obtained with w = 8.2 μm and h = 6.7 μm. The expected mode profile of a waveguide of such dimension is presented in Figure 3.10 (b), and is compared with the mode of a conventional [54] single-mode optical fiber (8.2 μm core diameter, Δn = 0.0053 core-cladding refractive index difference).

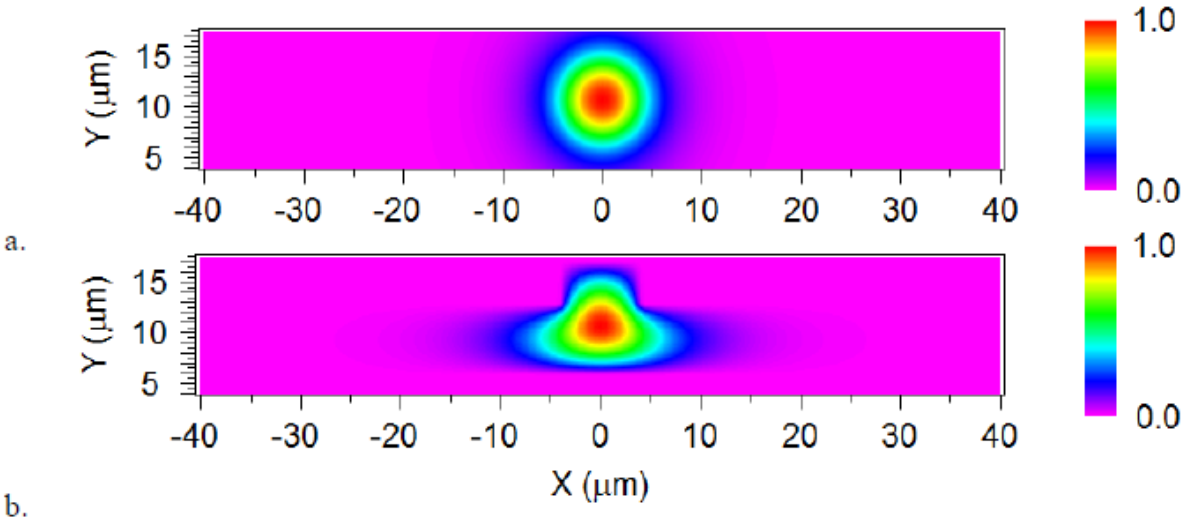

Figure 3.10: (a) Simulated amplitude mode profile of a conventional single-mode optical fiber (8.2 μm core diameter, Δn = 0.0053 core-cladding refractive index difference). (b) Simulated mode profile of the silicon-on-insulator waveguide having the dimensions (H = 11 mm, w = 8.2, h = 6.7) that maximize fiber-waveguide coupling efficiency (η = 0.8847).

As we have determined the ideal values of the back mirror reflectivity (r_2), the waveguide group index (n_g), and the fiber-waveguide coupling efficiency (η), it is now possible to predict

[4] For single-mode waveguides and optical fibers, the fiber-to-waveguide and waveguide-to-fiber coupling efficiencies are identical quantities. For the multi-mode region presented in Figure 3.9 (b), however, the calculated efficiency applies strictly to coupling from the single-mode fiber to the waveguide.

the GTI ideal response using Eq. (3.11). In Figure 3.11, the GTI intensity reflection spectrum is simulated for an L = 415 μm interferometer. When considering η = 1 as the fiber-waveguide coupling efficiency, the GTI yields a reflectivity greater than 99.9% over the bandwidth of the cavity back mirror. However, when considering the best possible coupling efficiency (η = 0.8847) between the circular optical fiber mode and the rectangular-like waveguide mode, the reflectivity drops to -0.5 dB with -1 dB wavelength dependant losses at the resonance wavelengths.

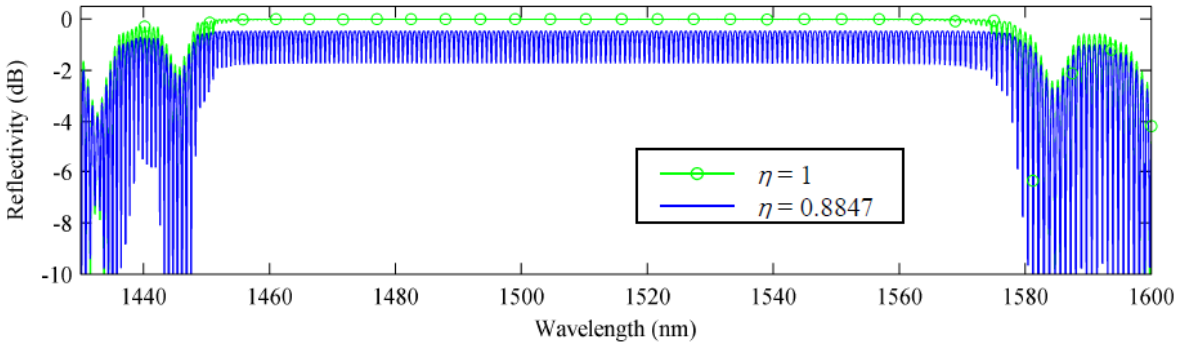

Figure 3.11: Expected reflectivity of the proposed GTI when considering perfect fiber-waveguide coupling efficiency (η = 1) and also the best possible coupling efficiency obtained from the beam propagation method simulations (η = 0.8847).

In Figure 3.12, the same reflectivity spectra (with η = 0.8847) is presented over a narrower wavelength range, outlining more clearly the behaviour of the GTI at the resonance wavelengths. The optical phase (ϕ) of the reflected signal ($r_{GT} = |r_{GT}|e^{i\phi}$) and the corresponding group delay (GD) are also presented. The latter is related to the optical phase through:

$$GD = -\frac{d\phi}{d\omega} = \frac{\lambda^2}{2\pi c}\frac{d\phi}{d\lambda}, \tag{3.14}$$

where c is the speed of light in vacuum and ω is the angular frequency. At the resonance wavelengths, constructive interference leads to a stronger confinement of light inside the cavity (i.e. light is confined for a longer period of time). This stronger confinement of light translates in group delay peaks, which are visible in the group delay spectrum presented in Figure 3.12 (c).

Finally, the derivative of these group delay peaks yields the group delay dispersion (GDD) spectrum of the interferometer (Figure 3.12 d). We perform this derivative (Eq. (3.15)) relative to the wavelength in order to be consistent with optical fiber suppliers (e.g. [54]), which usually express group delay dispersion in picoseconds per nanometres (ps/nm).

$$GDD = \frac{dGD}{d\lambda} \tag{3.15}$$

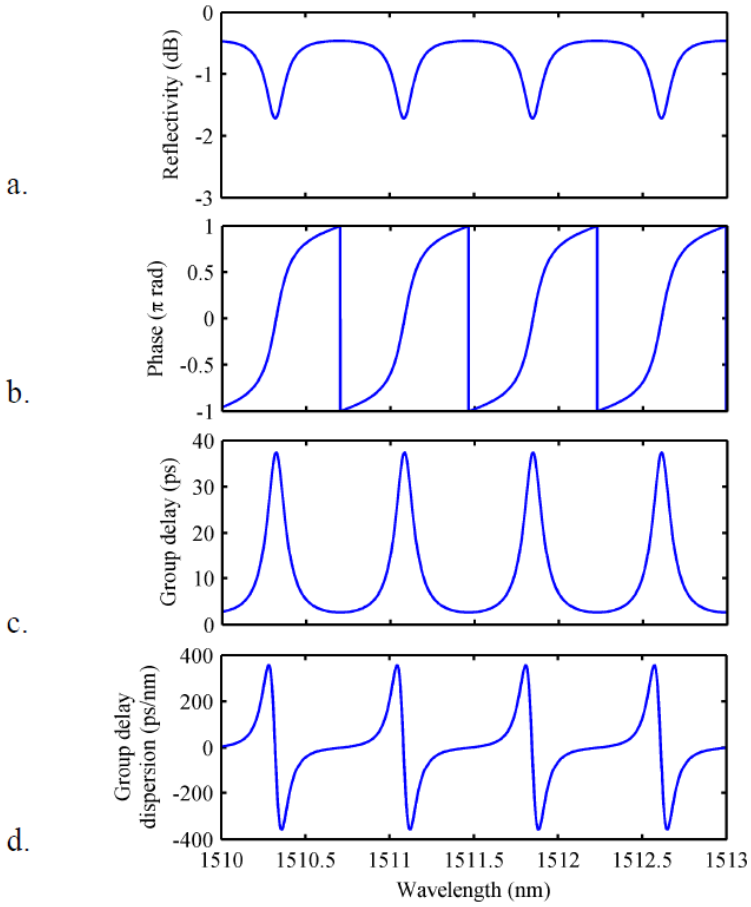

Figure 3.12: Simulated response of a 100 GHz free spectral range GTI based on the mirror presented in Figure 3.8 and considering the best possible fiber-waveguide coupling efficiency (η = 0.8847). No other sources of loss are considered. (a) Reflectivity. (b) Optical phase. (c) Group delay. (d) Group delay dispersion.

The wavelength separation (FSR) between adjacent GTI resonance peaks is given by:

$$FSR = \frac{\lambda^2}{2n_g L} \tag{3.16}$$

This expression does not account for the effective thickness of the cavity back mirror (as for long Fabry-Perot cavities in Eq. (3.2)), since this quantity will always be negligible compared to the cavity lengths (L) that will be designed. We will indeed always use cavity lengths such that the FSR matches the channel separation (100 GHz, 50 GHz, 25 GHz) of dense wavelength multiplexed (DWDM) optical fiber telecommunication networks. Expressing the GTIs free spectral ranges in frequencies, rather than in wavelengths (Eq. (3.16)) is therefore more relevant in the present case:

$$FSR = \frac{c}{2n_g L}. \tag{3.17}$$

Using n_g = 3.60 in Eq. (3.17), the interferometer lengths (L) required to match 100, 50, and 25 GHz channel separations are respectively 416.4, 832.8, and 1665.5 μm.

3.2.1.1 Tunability

In the same way as the free-space Fabry-Perot interferometers presented in section 3.1, Gires-Tournois interferometers are very sensitive to refractive index variations. Adjusting the effective index of the GTI waveguides could therefore allow resonance wavelength tuning for application that would require dynamic adjustments. Using the same formalism as in section 3.1.1, the sensitivity of the resonance wavelengths to effective index changes (for long GTI interferometers with negligible Bragg mirror thicknesses) is given by:

$$\frac{\Delta\lambda_{Res}}{\Delta n_g} = \frac{\lambda_{Res}}{n_g}. \tag{3.18}$$

Considering a n_g = 3.60 waveguide effective index and a $\lambda \sim$ 1550 nm wavelength of operation, the expected GTI sensitivity is 430 nm/RIU.

If our proposed GTIs were to be tuned, their required tuning range would most certainly be smaller or equal to one free spectral range (i.e. when tuned by exactly one FSR, a GTI yields essentially the same spectral response as its initial one). As the larger FSR considered for the current GTIs is 100 GHz (~ 0.8 nm) the maximum required effective index change, for the proposed devices, would be $\Delta n_g = 2 \times 10^{-3}$. Such group index variation could easily be achieved using carrier injection [10] or thermo-optic tuning [55].

3.2.2 Potential applications

As discussed above (and also in more details in Chapter 7, section 7.3), two potential uses of Gires-Tournois interferometers are in optical fiber dispersion compensation devices and in Michelson-GTI interleavers. As shown in Figure 3.12 (c), each group delay peak present positive and negative slopes, which result (Figure 3.12 d) in positive and negative group delay dispersion. This dispersive behaviour could be used to compensate chromatic dispersion of optical fiber telecommunication network. This application was one of the primary objectives for the development of in-plane GTIs. Indeed, the proposed in-plane configuration presents advantages compared to existing out-of-plane designs. For example, as discussed in Chapter 7, section 7.3, in-plane configuration allows long interferometers (L > 1 mm) having FSRs that match dense DWDM channel spacing of 25 of 50 GHz. Such interferometer length is not possible with on-chip out-of-plane designs [56] that are limited by the thickness of the silicon substrate (~ 500 μm). The waveguided in plane configuration could also allow tuning of the resonance wavelength position (see section 3.2.1.1) for fast tunable dispersion compensation.

However, dispersion compensation with GTIs typically requires several cascaded interferometers [56] in order to allow group delay slopes that are constant over the channel bandwidths. In our case, even without considering any imperfections in our GTIs, the upper limit of the fiber-waveguide coupling efficiency (η = 0.8847) is expected to induce -1.5 dB losses at resonance. Cascading several interferometers would therefore most likely induce unacceptable losses compared to existing systems based on fiber Bragg gratings [57]. For example, these systems typically report dispersion tuning ranges of ± 1500 ps/nm over channel bandwidths greater than 30 GHz. For cascaded Gires-Tournois with entrance mirror reflectivity around 30%,

achieving a similar dispersion range over such channel bandwidth would require at least seven cascaded Gires-Tournois [58]. If each Gires-Tournois causes, in the best case, -1.5 dB insertion losses, overall insertion losses greater than 10 dB can be expected, which is significantly higher than what is achieved experimentally (~ 5 dB) using thermally actuated fiber Bragg grating systems [57].

A more realistic application of our Gires-Tournois interferometer would therefore be in Michelson-GTI bandpass filters such as optical interleavers. As described in [59], and schematized in Figure 3.13 (a), these devices use a single GTI as a dispersive mirror in one arm of a Michelson interferometer, while a conventional mirror is placed in the other arm. If the length difference between the two arms, and the reflectivity of the GTI entrance mirror, are designed properly (see [59]), the phase difference between the arms yields a step-like increase (as a function of wavelength), which can be used for flat top interleaving. Ideally, the cavity entrance mirror must have an $r = 0.4$ amplitude reflectivity, which is not far from the $r = 0.55$ entrance mirror reflectivity of our GTIs.

Figure 3.13 (b) presents the interleaving capability of the ideal GTI described in Figure 3.12 (i.e.: when no source of loss is considered except the $\eta = 0.8847$ fiber-waveguide coupling efficiency). The reflectivity of the reference mirror is set to -0.5 dB in order to match the maximum peak reflectivity obtained in Figure 3.12 (a). This proposed interleaver yields 20 dB channel isolation, -0.5 dB insertion losses and flat top response over nearly 50 GHz (for a 100 GHz FSR Gires-Tournois interferometer). Tunable GTIs could also allow, for example, dynamic compensation of drifts due to temperature variations.

a.

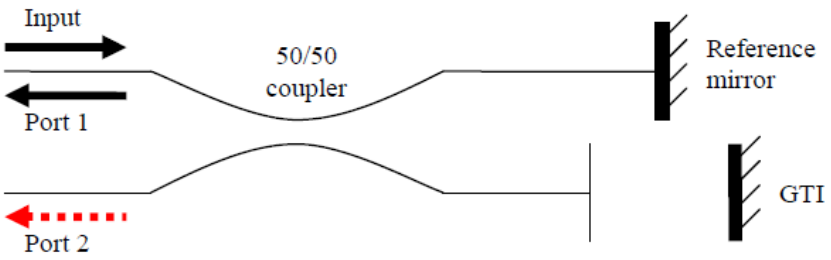

b.

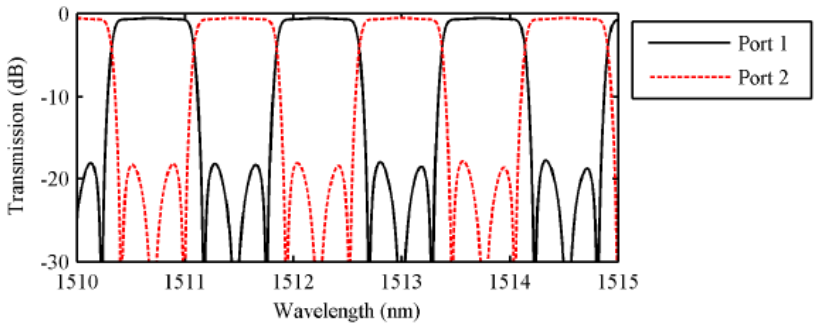

Figure 3.13: (a) Schematic representation of a Michelson-GTI interleaver. (b) Simulated interleaving capability of a Michelson-GTI interleaver based on the GTI presented in Figure 3.12.

3.3 Summary of main results

3.3.1 Modeling of losses affecting deep-etched multilayer interferometers

Up to this point, the interferometers proposed in this work were not considered to suffer from any insertion losses (other than the unavoidable losses occurring when coupling a circular fiber mode to a rectangular-like waveguide, see section 3.2.1). When considering no sources of loss, silicon-air Fabry-Perot interferometers, for example, are expected to yield very high resonance finesses and null insertion losses (see section 3.1.1). However, as outlined in introduction (section 1.2), the finesses and the insertions losses that were previously obtained experimentally are always order of magnitude smaller than what is predicted by basic ideal simulations.

In Chapter 4, in order to explain this difference between experimental results and ideal case simulations, a series of models for the various sources of loss occurring in deep-etched multilayer optical resonators will be proposed. Namely:

1. Divergence of the input optical beam in free-space interferometers (applicable to free-space interferometers).
2. Reduced transmission and reflection caused by surface roughness at the silicon-air interfaces of deep-etched reflectors (applicable to both free-space and waveguided interferometers).
3. Verticality deviations of the etch profiles (applicable to both free-space and waveguided interferometers).
4. Misalignment between the input and output optical fibers (applicable to free-space Fabry-Perot interferometers).

Of these four loss mechanisms, the first two will be found to be the dominant sources of loss in free-space Fabry-Perot interferometers, while the second one will be found to be the main loss source in waveguided Gires-Tournois interferometers (Chapter 7). The third one will be found to be generally important but, for the reported devices, to be negligible compared to the first two. Finally, the fourth one will be found to be essentially negligible in all cases.

3.3.2 Fabrication of free-space interferometers with predictable dimensions

As described in Chapter 2 (section 2.3.2), plasma etching of free-space silicon-air multilayer reflectors usually yield unpredictable layer dimensions, which translates in highly unpredictable optical characteristics. Waveguided interferometers do not suffer from the same problem since, in this case, every etched trench is designed with the same initial width, which translates in identical width variations upon mask undercut during plasma etching. In Chapter 4, a fabrication method that allows the same dimension predictability for free-space interferometers than for waveguided interferometers will be presented and will be successfully implemented experimentally.

3.3.3 Free-space Fabry-Perot interferometers for sensing applications

As described in section 3.1.2, free-space Fabry-Perot interferometers are expected to be highly sensitive to refractive index variations and mechanical deformations. These properties will be confirmed in Chapter 5 and Chapter 6, and will be used to create two different types of sensors.

3.3.3.1 Refractive index measurement of liquids in microfluidic systems

In Chapter 5, free-space Fabry-Perot interferometers will be monolithically integrated with microfluidic systems to create refractive index sensors for homogenous liquids. The refractive index sensitivity expected from section 3.1.2 will be confirmed experimentally using certified refractive index oils. From this high experimental sensitivity (907 nm/RIU), the limit of detection of the sensor will be shown to be 1.7×10^{-5} RIU.

3.3.3.2 Gas sensing using polymer-functionalized free-space Fabry-Perot interferometers

In Chapter 6, free-space Fabry-Perot interferometers will be functionalized with gas absorbent polymers. Upon absorption, these polymers will deform the interferometers and induce important resonance wavelength shifts, in accordance with the formalism presented in section 3.1.2. Fabry-Perot interferometers will be functionalized with two different polydimethylsiloxane (PDMS) based polymers that will be tested for the detection of xylene and cyclohexane vapors. Limits of detection of 1.6 ppm and 6.3 ppm, respectively, will be obtained for these two compounds.

3.3.4 Guided Gires-Tournois interferometers for optical telecommunication applications

Finally, in Chapter 7, the waveguided Gires-Tournois interferometers proposed in section 3.2 will be fabricated and tested. Surface roughness at the silicon-air material interfaces will be found to induce important losses at resonances, in accordance with the model for surface roughness presented in Chapter 4. However, at off resonance wavelengths, acceptable loss levels (below 2 dB) will be reached and could therefore allow useful applications in Michelson-GTI filters, as proposed in section 3.2.2.

CHAPTER 4 ADVANCES IN MODELING, DESIGN, AND FABRICATION OF DEEP-ETCHED MULTILAYER RESONATORS

This chapter presents analytical models for the prediction of the optical properties of deep-etched multilayer optical resonators. Sections 4.1-4.8 are a reproduction of an article published in Journal of Lightwave Techonology[5], in which models for Gaussian beam divergence and surface roughness at silicon-air material interfaces are presented. These models are demonstrated to predict remarkably well measurements performed on deep-etched Fabry-Perot interferometers, leading us to conclude that surface roughness and Gaussian beam divergence are the dominant loss mechanism affecting the Fabry-Perot interferometers presented in this thesis. The article also presents a technique for the design and fabrication of deep-etched free-space Fabry-Perot interferometers having predictable dimensions, which, as presented in section Chapter 2 (section 2.3.2), is not possible using single lithography fabrication techniques.

In section 4.9, an unpublished extended discussion on other sources of losses affecting deep-etched free-space Fabry-Perot resonators is presented. The formalism developed in the article is modified to account for misalignment between input and output optical fibers, or for imperfect verticality of the etch profiles. In general, these imperfections are predicted to yield non-negligible effects on the finesse and peak transmission at resonance of the interferometers. However, in the context of this thesis, considering the use of non-collimated Gaussian beams ($\omega_0 = 5$ μm) and the important amounts of surface roughness at silicon-air interfaces, these imperfections are predicted to be less important than Gaussian beam divergence and surface roughness.

---

[5] R. St-Gelais, A. Poulin, and Y.-A. Peter, "Advances in modeling, design, and fabrication of deep-etched multilayer resonators," Journal of Lightwave Technology, vol. 30, pp. 1900-1908, 2012.

4.1 Authors and affiliation

Raphael St-Gelais, Alexandre Poulin, and Yves-Alain Peter

Department of Engineering Physics, Ecole Polytechnique de Montréal, P.O. Box 6079, Station Centre-Ville, Montréal, Quebec H3C 3A7, Canada

4.2 Abstract

We present recent advances in modeling, design, and fabrication of in-plane multilayer optical resonators fabricated by high aspect ratio etching of silicon. We first revisit the model of Gaussian beam divergence proposed by A. Lipson et al. to correct a mistake that leads to an underestimation of the losses affecting this type of resonator. Secondly, we discuss the influence of surface roughness at the silicon-air interfaces of multilayered structures. Roughness profiles—measured by white light interferometry on the sidewalls of silicon trenches etched by deep reactive ion etching (DRIE)—are presented. The single absorbing layer model of Carniglia et al. is used to predict the influence of the measured roughness (30 ± 5 nm RMS). This model is combined with the corrected model for Gaussian beam divergence and is compared with recent experimental results obtained for a new generation of deep-etched Fabry-Perot refractive index sensors. These sensors are fabricated using the contour lithography method, which is demonstrated to greatly improve the predictability of their optical characteristics. The combined model for roughness and divergence is found to correspond remarkably well with the experimental results, with predictions of loss and finesse of the resonances within an average error of 1.3 dB and 25%, respectively. We therefore expect the models and the simulations presented in this article to become a useful tool for the design of devices based on deep-etched multilayer resonators.

Index Terms—Fabry-Perot resonators, Integrated optics, Optical resonators, Scattering.

4.3 Introduction

With the availability of high performance etching processes for silicon and with the need for cheap integrated optical components, silicon photonics is now attracting the attention of several research groups. In particular, multilayered silicon-air structures based on vertically

etched high aspect ratio trenches are interesting since the in-plane configuration allows simple integration with electrostatic actuators, microfluidic systems, optical fibers and waveguides.

Because of the high refractive index contrast between silicon and air, mirrors based on these structures have a high reflectivity on a broad spectrum for very few Bragg periods. Two of such mirrors could therefore be used to form high finesse Fabry-Perot cavities. This possibility was investigated to fabricate tunable filters [12, 18, 19, 21], refractive index sensors [60] and high quality factor resonators [27]. However, as reported in Table 4.1, each of these devices suffers from high insertion loss and relatively low finesse ($\mathfrak{F}$). These performances make the tunable filters unusable for most of the targeted telecommunication applications. Such imperfections are less critical for refractive index sensors [60] than for tunable filters, but their detection limit could still be greatly improved by increasing the finesse of the resonance.

Table 4.1: Reported performances of deep-etched Fabry-Perot resonators

Device type	Finesse	Peak transmission (dB)	Ref.
Tunable filter	39	-10	[19]
Tunable filter	24	-17	[21]
Refractive index sensor	7.1	-26	[60]
High quality factor cavity	20	-23	[27]

Therefore, it becomes necessary to identify clearly the influence of the different sources of losses in resonators based on deep-etched Bragg reflectors, with a particular emphasis on Fabry-Perot cavities coupled to optical fibers. In section 4.4, Gaussian beams are decomposed into plane waves to calculate the effect of beam divergence. The analysis is very similar to the one proposed in [24] but an important difference is outlined, which influences the results significantly. In section 4.5, measurements of surface roughness profiles on typical deep-etched sidewalls are presented. The single absorbing layer model [61] is proposed for the prediction of the losses due to the measured amount of roughness. In section 4.6, the models for divergence and roughness are combined and are compared to experimental results obtained with a new generation of previously reported Fabry-Perot refractive index sensors [60]. These sensors are now fabricated by the contour lithography method [62]. We demonstrate that this technique improves the predictability of the dimensions of the optical resonators, and therefore of their

optical characteristics. Finally, a brief discussion on other sources of loss that are not treated in the present text is presented in section 4.7.

4.4 Gaussian beam reflection and transmission through ideal deep-etched multilayers

4.4.1 Theory

A Fabry-Perot cavity based on two in-plane Bragg mirrors is presented in Figure 4.1. Each of the Bragg mirrors is made of 2.5 silicon-air periods (P). If the thickness of each of the layers equals an odd multiple (m_{Si} for silicon and m_{Air} for air) of a quarter of a given wavelength (λ_c), the mirrors should have a broadband high reflectivity centered on λ_c. Fabry-Perot resonance will occur at that wavelength when a cavity of an integer multiple (m_{Gap}) of $\lambda_c/2$ is formed between the two mirrors. In this text, as in [24], the dimensions of Fabry-Perot cavities will be written using a notation that includes the odd multiple of the silicon (m_{Si}) and air (m_{Air}) layers, and the integer multiple of the cavity (m_{Gap}): (m_{Si}, m_{Air}, m_{Gap}). The cavities are considered to be coupled at normal incidence to lensed or cleaved single-mode optical fibers, which working distance (W_d) and waist (ω_0) are presented in Fig. 1. For cleaved Corning® SMF-28™ fibers at near IR wavelength (1550 nm), the working distance and the waist are approximately zero and 5 μm, respectively.

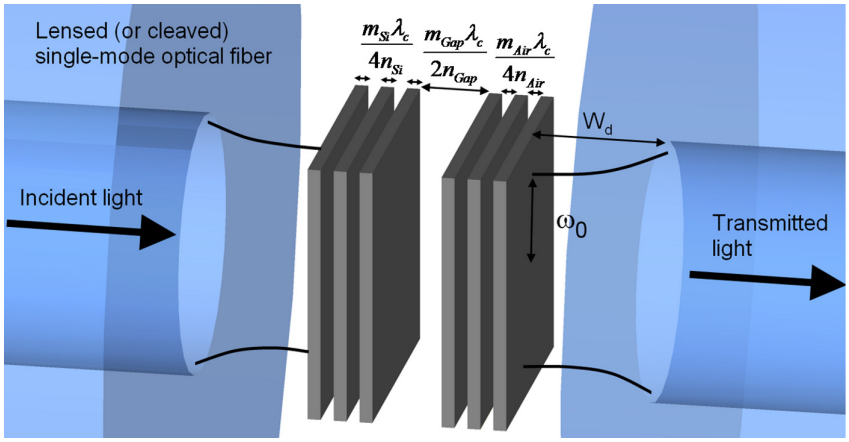

Figure 4.1: Schematic representation of a (m_{Si}, m_{Air}, m_{Gap}) Fabry-Perot cavity made of two mirrors of 2.5 silicon-air Bragg periods (P). The cavity is coupled at normal incidence to lensed or cleaved single-mode fibers of working distance W_d and Gaussian beam waist ω_0.

Assuming that the beam incident on the multilayer structure of Figure 4.1 is Gaussian and propagates along the z axis, its complex electric field distribution (neglecting the amplitude constant) can be expressed as in Eq. (4.1), where *q(z)* is the complex beam parameter, *k* is the wavenumber, ω_0 is the beam waist and λ is the wavelength in the medium [63].

$$E(k,x,y,z) = \frac{q_0}{\omega_0}\frac{1}{q(z)}\exp\left(-ik\frac{x^2+y^2}{2q(z)} - ikz\right), \tag{4.1}$$

with:

$$q(z) = z + q_0 = z + i\frac{\pi\omega_0^2}{\lambda}.$$

In order to compute the transmission through the multilayer system, the beam is decomposed into a two dimensional angular distribution of plane waves [64, 65] of transverse wavenumbers k_x and k_y. This is done by performing the Fourier transform presented in Eq. (4.2).

$$\begin{aligned}\tilde{E}(k,k_x,k_y,z) &= \iint E(k,x,y,z)\,e^{-i(k_x x + k_y y)}dxdy \\ &= -\frac{q_0}{\omega_0}\frac{2\pi i}{k}\exp\left(-i\frac{q(z)\left(k_x^2+k_y^2\right)}{k} - ikz\right)\end{aligned} \tag{4.2}$$

At this point, since the problem presents circular symmetry around the *z* axis, the two transverse components of the wavevector can be merged into a single variable using $k_t^2 = k_x^2 + k_y^2$ in Eq. (4.2).

For the transmission and the reflection of plane waves, the characteristic matrix formalism [34] is used. Each of the *p* layers of the assembly is modeled by a 2×2 matrix which is function of its thickness (d_r), its refractive index (N_r), of the angle of propagation in the layer (θ_r), and of the wavelength in vacuum (λ_0). The matrices are multiplied, starting with the output medium of admittance η_{out} and ending with the first layer of the assembly (at the interface with the incidence medium):

$$\begin{bmatrix} B \\ C \end{bmatrix} = \left\{ \prod_{r=1}^{p} \begin{bmatrix} \cos\delta_r & (i\sin\delta_r)/\eta_r \\ i\eta_r \sin\delta_r & \cos\delta_r \end{bmatrix} \right\} \begin{bmatrix} 1 \\ \eta_{out} \end{bmatrix} \tag{4.3}$$

with:

$$\delta_r = 2\pi N_r d_r \cos\theta_r / \lambda_0 ,$$

$$\eta_r = N_r \cos\theta_r \text{ (for s polarization)},$$

$$\eta_r = N_r / \cos\theta_r \text{ (for p polarization)}.$$

In Eq. (4.3), the cosines of the angle of propagation (θ_r) in each layer can be expressed in term of the refractive index of the layer, of the wavelength in vacuum (λ_0) and of the transverse component of the wavevector (k_t) which is independent of the refractive index of the medium. This is presented in Eq. (4.4), which is simply an alternative notation of Snell's law of refraction.

$$\cos\theta_r = \sqrt{1-\left(k_t\lambda_0 / 2\pi N_r\right)^2} \tag{4.4}$$

Using Eq. (4.4) in Eq. (4.3), the amplitude reflection (r) and transmission (t) coefficients can be obtained [34] as a function of k_t, λ_0 and of the admittance of the incident medium (η_{inc}):

$$\begin{aligned} r(\lambda_0, k_t) &= \frac{\eta_{inc}B - C}{\eta_{inc}B + C}, \\ t(\lambda_0, k_t) &= \frac{2\eta_{inc}}{\eta_{inc}B + C}. \end{aligned} \tag{4.5}$$

Finally, using the plane wave distribution of Eq. (4.2) combined with the plane wave reflection and transmission coefficients of Eq. (4.5), it is possible to obtain the reflectivity and the transmission of the complete system.

From this point, it is assumed that the distance between the optical fibers and the multilayer system is equal to the lensed fibers working distance (W_d), as depicted in Figure 4.1. In the current notation, this involves taking z=0 in Eq. (4.2). The important example of a cleaved single-mode optical fiber should be represented accurately by this assumption if the fibers are placed as close as possible to the multilayer assembly ($W_d \approx 0$). It is also assumed that, at the first

and last interfaces of the multilayer system, the medium is air and has unit refractive index (i.e.: $\eta_{inc}=\eta_{out}=\eta_{vacuum}$).

The fiber-to-fiber transmission and reflection spectra (T, R) are obtained by multiplying the incident electric field distribution of Eq. (4.2) by the coefficients of Eq. (4.5), and by calculating the overlap integral with the output optical fiber:

$$T(\lambda_0), R(\lambda_0) = \frac{\left|\left\langle \tilde{E}_{out} \middle| \tilde{E}_{fiber} \right\rangle\right|^2}{\left\langle \tilde{E}_{fiber} \middle| \tilde{E}_{fiber} \right\rangle^2}, \tag{4.6}$$

with:

$$\tilde{E}_{fiber} = \tilde{E}\left(\frac{2\pi}{\lambda_0}, k_t, 0\right),$$

$$\tilde{E}_{out}\left(\frac{2\pi}{\lambda_0}, k_t, 0\right) = \tilde{E}_{fiber} \cdot t(\lambda_0, k_t) \text{ (transmission)}$$

$$\tilde{E}_{out}\left(\frac{2\pi}{\lambda_0}, k_t, 0\right) = \tilde{E}_{fiber} \cdot r(\lambda_0, k_t) \text{ (reflection)}$$

At this point, a choice must be made whether to use the plane wave coefficients (t, r) calculated for s or p polarization using Eqs. (4.3)-(4.5). The Gaussian beam expression of Eq. (4.1) is a linear approximation, which implies that the components of the polarization that are parallel to the main direction of propagation (the z axis) are considered to be weak and are neglected [66]. Therefore, if the Gaussian beam approximation is appropriate to treat the current problem, the use of whether the s or the p coefficients of transmission and reflection should not influence the calculated results (for the case of a beam at normal incidence). This is effectively the case. For all the following calculations, using s or p coefficients yields almost exactly the same spectra. In the worst case (minimum beam waist and highest number of periods for each Bragg mirrors) the difference at peak transmission is less than 0.3 dB.

The bracket notation in Eq. (4.6) denotes the scalar product of two electric fields. From the properties of Fourier transforms, it can be calculated directly in the k_t space without going back to the (x, y) space (see Parseval's theorem [67]). From the circular symmetry of the problem, this integration can be performed in polar coordinate.

$$\left\langle \tilde{E}_1 \middle| \tilde{E}_2 \right\rangle = 2\pi \int_0^k \tilde{E}_1 \tilde{E}_2^* k_t dk_t \tag{4.7}$$

The analysis of Eqs. (4.1)-(4.6) is equivalent to the one published by A. Lipson et al [24]. These authors must of course be credited for the original idea, at least in the context of deep-etched multilayer resonators (similar developments can be found to treat the deformation of beams incident on multilayer structures [64]). However, in Eq. (4.2) of [24], it appears that the integration was performed only along k_t without considering the circular symmetry of the problem. In the current notation, this is equivalent to replace $k_t dk_t$ in Eq. (4.7) by dk_t.

This error can have important consequences on the calculated response of resonators based on deep-etched Bragg reflectors. In Figure 4.2, the transmission of a Fabry-Perot cavity based on 2.5 periods mirrors is calculated for different beam waist using the formulation of the overlap integral of Eq. (4.7), and also by removing the k_t factor, as appears to be the case in [24]. The axis limits are set to reproduce as exactly as possible the Fig. 2 of [24]. For a 31 μm beam waist, the effect of divergence is negligible and both models yield the same transmission spectrum. However, for a 4 μm waist, the difference between the peak transmissions is nearly 10 dB.

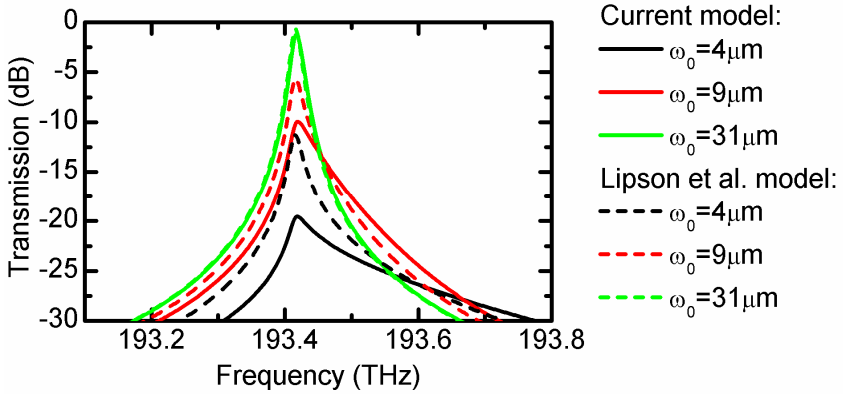

Figure 4.2: Transmission spectra of a (m_{Si}, m_{Air}, m_{Gap}) = (*21, 5, 2*) Fabry-Perot filter of 2.5 periods mirrors for various Gaussian beam waists. Plain lines: calculation using the current proposed model. Dashed lines: calculations removing the k_t factor in Eq. (4.7), as is supposed to be an error in Lipson et al. [24] original model. For large beam waists (ω_0=31 μm) the effect of divergence is negligible and the curves obtained with the two models are superimposed.

In order to validate which of the current or of Lipson et al. [24] model is accurate, a simple numerical experiment was also performed. The developed algorithm (Eqs. (4.1)-(4.7)) was used to calculate the coupling loss between two optical fibers separated by an air layer. This is done using a single air layer of any given thickness in Eq. (4.3). With the current model, the results match perfectly the equations developed in [68]. Removing the k_t factor in Eq. (4.7) yields the square root of the value of [68]. This can be understood by noting that removing k_t in Eq. (4.7) is equivalent to considering divergence in only one (say x) of the two transverse dimensions (x, y).

4.4.2 Discussion

The difference between the two models, outlined in Figure 4.2, justifies the formulation of new design rules for resonators based on deep-etched Bragg reflectors, especially since it affects particularly the important case of cleaved single-mode optical fibers ($\omega_0 \approx 5$ μm at λ_0=1550 nm).

These are presented in Figure 4.3, where the peak transmission and the finesse ($\mathfrak{F}$) are reported as a function of Gaussian beam waist, for a variety of Fabry-Perot resonators having resonance peaks centered on λ_c=1550 nm. The finesse is defined as the ratio of the free spectral range (FSR) and of the full width at half maximum (FWHM) of the resonance peaks ($\mathfrak{F}$=FSR/FWHM). The FWHM is determined by inspection of the simulated resonance. For long cavities (large m_{Gap}) the thickness of the mirrors is negligible compared to the cavity length and the FSR can be determined solely from the m_{Gap} value using the simplification in Eq. (8). For shorter cavities (small m_{Gap}), however, the phase shift upon reflection on the mirrors becomes significant and the FSR must be calculated by inspection of the transfer matrix simulations using:

$$FSR = \frac{\Delta\lambda_c}{\Delta m_{Gap}} = \frac{\lambda_c}{2}\frac{\Delta\lambda_c}{\Delta(n_{gap}l)} \xrightarrow{\text{large } m_{Gap}} \frac{\lambda_c^2}{2n_{gap}l} = \frac{\lambda_c}{m_{Gap}}, \tag{4.8}$$

where $l=m_{Gap}\lambda_c/2n_{gap}$ is the distance between the mirrors.

In Figure 4.3, the dimension constants (m_{Si}, m_{Air}, m_{Gap}) of the resonators are increased progressively with the beam waist to take into account the limitations of deep etching techniques. When the beam diameter ($2\omega_0$) becomes more than 25 times greater than the thickness of the air layers ($m_{Air}\lambda_c/4$), the dimension constant m_{Air} is increased to the next odd integer (i.e.: the

required aspect ratio is kept below 1:30). The thickness of the silicon layers (related to the integer m_{Si}) is also adjusted to respect the same aspect ratio criterion.

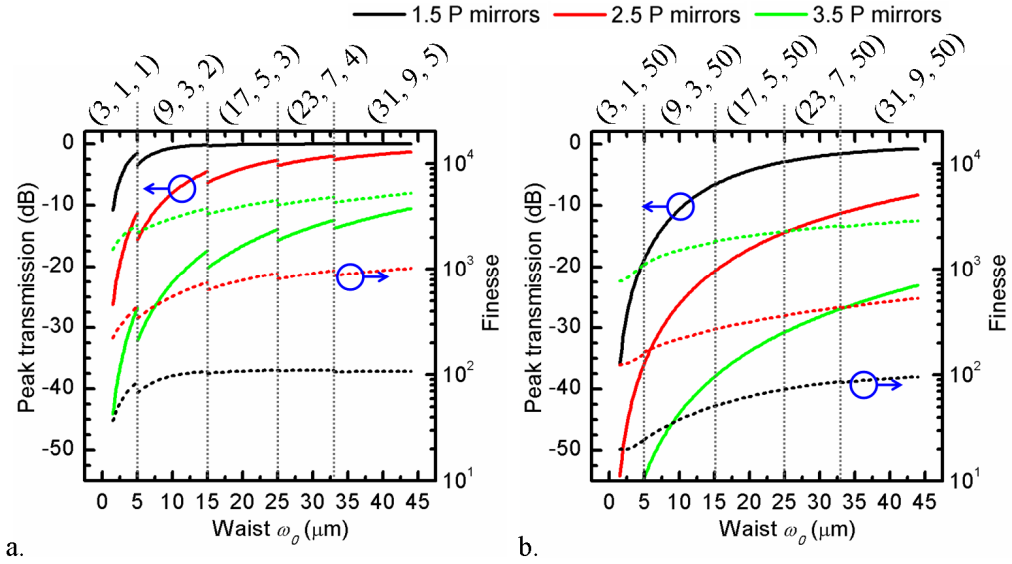

Figure 4.3: Peak transmission (plain lines) and finesse (dashed lines) of a Fabry-Perot resonance occurring at the center of a reflection bandwidth, set at λ_c=1550 nm, as a function of the Gaussian beam waist, and for various silicon-air periods (P) in each mirror. The (m_{Si}, m_{Air}, m_{Gap}) dimension parameters are adjusted to maintain a 1:30 maximal aspect ratio criterion for the etched trenches. (a) Simulations performed for shorter cavity lengths (e.g.: tunable filters). (b) Simulations performed for longer cavities (e.g.: sensors).

In Figure 4.3 (a), simulations are performed for short cavity lengths (low m_{Gap}), which are more representative of works related to tunable Fabry-Perot filters [12, 18, 19, 21]. Increasing the number of silicon-air periods increases the reflectivity of the Bragg mirrors and therefore increases the finesse. However, this also confines the light more strongly within the cavity and the losses due to divergence increase. For 1.5 period mirrors, it is theoretically possible to reach losses lower than -3 dB for the typical beam waist of a cleaved single-mode fiber (~5 μm). For 2.5 period mirrors, the same level of losses is obtained only with beam waists of 23 μm or higher. For 3.5 period mirrors, the same level of loss could not be obtained unless using inconvenient etch depths (>100 μm). Maintaining good surface quality and constant layer thickness on such a high depth would be extremely challenging. Moreover, as the (m_{Si}, m_{Air}) dimension constants

increase, the width of the reflection band (i.e.: the range around λ_c on which high finesse Fabry-Perot resonance occurs) reduces significantly. For example, at dimensions higher than (m_{Si}, m_{Air})=(23, 7), the reflection bandwidth becomes lower than 80 nm and it becomes impossible to cover more than one of the 40 nm wide S, C and L telecommunication bands.

In Figure 4.3 (b), simulations are performed for longer cavity lengths (large m_{Gap}), which are more representative of the work related to Fabry-Perot refractive index sensors [60]. The losses are more important in this case since light diverges on a longer distance during each round trip in the cavity. Losses are however less critical for sensors than for tunable filters. Their design, for the highest possible finesse, should therefore also be dictated by the highest amount of loss that is acceptable with a given measurement setup, by the operation bandwidth, and by other considerations such as the amount of surface roughness, as presented in the next section.

4.5 Surface roughness in deep-etched trenches

Various well documented fabrication methods can be used to minimize the amount of surface roughness in deep-etched trenches. Most of the etching processes are performed in inductively coupled plasma reactors (ICP). At room temperatures, fluorine based ICP chemistry can be optimized to reduce the characteristic scalloping effect induced by chopping between passivation and etching gases [36, 37, 41, 45]. Both gases can also be used in room temperature mixed processes [44, 47], avoiding completely the scalloping effect at the expense of poorer selectivity to the etch mask. At cryogenic temperatures, however, mixed process can yield high selectivity and smooth sidewalls can be obtained in high aspect ratio structures [13, 37, 47, 69]. Other techniques, not based on ICP reactors, also allow etching of smooth high aspect ratio trenches such as electrochemical etching in hydrofluoric acid (HF) [70] and preferential etching of (110) silicon wafers along crystallographic planes [28, 71]. Finally, post-processing techniques such as thermal oxidation [72] and crystallographic planes selective etching [19, 73-75] can be used to reduce surface roughness in deep-etched silicon trenches.

4.5.1 Surface roughness model

Despite this variety of methods, few analyses were carried out to quantify the optical properties of deep-etched multilayered structures as a function of the amount of surface roughness at the material interfaces. In [73], the analysis is limited to a single silicon slab and

does not consider light divergence. In [30], surface roughness is treated as a random variation of the layers thickness (i.e.: scattering by surface roughness is neglected). This kind of analysis is usually appropriate for most Fabry-Perot cavities [51]. However, for silicon-air Bragg reflectors, the refractive index contrast between each layer is much higher than for any multilayer mirror fabricated by thin film deposition. As this contrast increases, the amount of light that is scattered by surface roughness is expected to become significant. Additionally, computing a random distribution of layer thicknesses together with the model of Gaussian beam divergence (section 4.4) would be tedious. For each component of the plane wave decomposition, the transfer matrices would have to be calculated several times to consider the random distribution, which would imply inconvenient computation delays.

For these reasons, the use of the model of Carniglia et al. [61] is proposed. A single absorbing layer is added at each material interface as a function of its surface roughness RMS (root mean square) value (σ). The thickness (d_R) of the layer is function of σ as d_R=2σ. The real part (n_R) of the refractive index of the layer (n) is given by Drude effective medium approximation [61]. An imaginary part (k_R) is added to n in order to take into account the reduced transmission and reflection predicted by the scalar scattering theory. The expression of n, for silicon and air as the adjacent mediums is given by:

$$\begin{aligned} n &= n_R - ik_R \\ &= \sqrt{\frac{n_{Air}^2 + n_{Si}^2}{2}} - i\frac{\pi}{2\sqrt{2}}\frac{\left(n_{Air} - n_{Si}\right)^2\left(n_{Air} + n_{Si}\right)}{\sqrt{n_{Air}^2 + n_{Si}^2}}\frac{d_R}{\lambda_0}. \end{aligned} \tag{4.9}$$

4.5.2 Roughness measurement

The single absorbing layer model requires the knowledge of the amount of surface roughness at the silicon-air interfaces, which is measured using a white light interferometric surface profiler (Fogale Photomap 3D optical profiler). Cleaved silicon-air multilayer test structures (Figure 4.4 a), fabricated simultaneously with the refractometer of Figure 4.8 and having the same silicon-air layers dimensions, are used for the measurements. The measured profile is presented in Figure 4.4 (b). The amount of surface roughness is evaluated on a 20 × 20 μm surface, which is centered on the expected position of the core of the single mode optical fiber that will be used for the characterization of the Fabry-Perot cavities. The measurement

yields a value of 30 ± 5 nm RMS. The 5 nm uncertainty was determined statistically by varying the size and the position of the measurement area, and by repeating the measurement on other test structures.

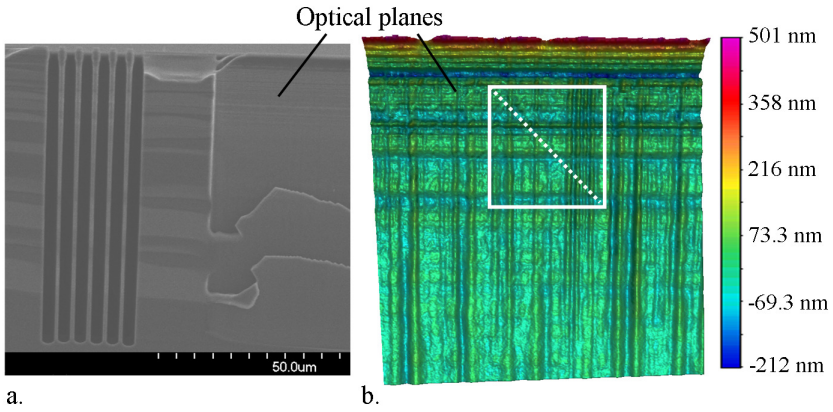

Figure 4.4: (a) Scanning electron micrograph cross section and front view of cleaved multilayer test structures etched using the same DRIE process as for the Fabry-Perot cavity of Figure 4.8. (b) Measured roughness profile of an etched optical plane. The roughness is evaluated within a 20 × 20 μm area (white square) centered on the expected position of the core of the single mode optical fiber that will used for the optical characterization.

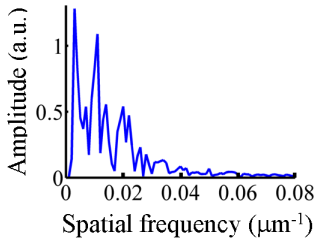

Figure 4.5: One dimensional Fourier transform of the measured profile (along the white dashed line of Figure 4.4 (b) showing that the measured roughness is dominated by large scale harmonics.

The one dimensional Fourier transform of the measured profile is also calculated, following the diagonal of the area of interest (i.e.: the white dashed line in Figure 4.4 b). Its amplitude, presented in Figure 4.5, indicates that the measured RMS roughness is mainly dominated by large-scale harmonics (i.e.: low spatial frequency roughness). This is an important parameter since it can be demonstrated [76] that the model of [61] is valid for large scale

roughness harmonics (T_m), respecting the criterion $1/T_m < 1/\lambda_0 n_2$, where n_2 is the higher refractive index of the assembly (i.e.: n_{Si} in the present case). The roughness measurement method should therefore be chosen carefully in order to ensure that the measured overall RMS roughness contains mainly large scale roughness harmonics, which cause scattering and are taken into account by the model. For example, as described in [77], atomic force microscopy measurements tend to contain mainly small scale harmonics that are not taken into account by the current model.

4.6 Experimental validation

4.6.1 Fabrication of deep-etched Fabry-Perot resonators by contour lithography

In order to compare the developed models for roughness and divergence with experimental results, a new generation of Fabry-Perot refractive index sensors previously described in [60] was fabricated. Instead of using single lithography and DRIE steps, the two masks contour lithography method proposed in [62] was used to fabricate separately the optical parts (multilayer mirrors) and the larger features (optical fiber alignment grooves, microfluidics). The fabrication steps are summarized here but ref. [62] should be consulted for further details, if needed.

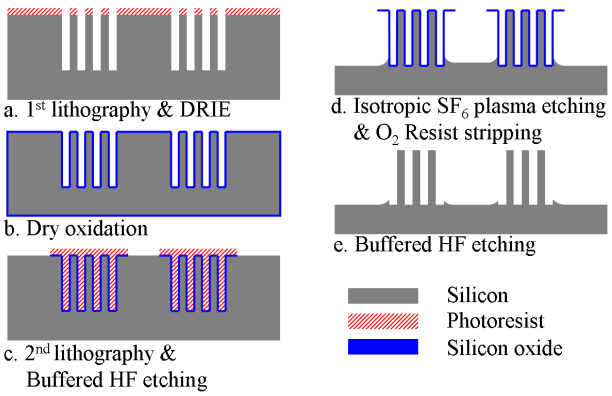

Figure 4.6: Schematic representation of the fabrication process used for the Fabry-Perot refractometer of Figure 4.8.

A schematic representation of the fabrication process is presented in Figure 4.6. The mirrors and the contour of the larger openings (optical fiber grooves, microfluids) are first etched

to a depth of 80 μm by deep reactive ion etching (step a) in an ICP180-100 plasma reactor (Oxford Instruments inc). The chamber parameters for the etching and passivation steps (applied 415 times each) are given in Table 4.2. After a dry oxidation step (~150 nm SiO_2) to protect the optical parts (step b), a second mask is used to define the larger openings (step c). The oxide is etched in buffered hydrofluoric acid (HF) and the larger features are etched by isotropic SF_6 plasma etching in the ICP plasma reactor (step d). The remaining oxide is finally etched in buffered HF (step e).

Table 4.2: DRIE Parameters

Parameter	Etching Step	Passivation step
Time (s)	6	4
ICP power (W)	450	450
Forward power (W)	18	10
SF_6 flow (sccm)	65	0
C_4F_8 flow (sccm)	4	65
O_2 flow (sccm)	6	0
Chuck temperature (^oC)	0	0
Chamber pressure (mTorr)	15	15

The contour lithography method was originally proposed as a technique to integrate nanoscale trenches with wider openings that require significantly different plasma etching conditions. We would like to outline another advantage of the technique, which was not reported in [62], and which motivated its use in the present case. When the mirrors are etched separately from the larger features, all the openings of the first photomask (used for step a in Figure 4.6) have the same width. This width will change upon fabrication because of diffraction during photolithography and undercut during plasma etching. However, since they all have the same initial width, all the air layers that form a set of mirrors can be assumed to have the same final thickness. Conversely, all the silicon layers in Figure 4.6 can also be assumed to have identical thicknesses. Moreover, the thickness of a silicon-air period in Figure 4.6 becomes a constant that is not affected by diffraction and undercutting. There is therefore only one unknown (i.e.: the air layers thickness) to consider during the design of the photomask and much more predictable optical characteristics can be obtained.

For the results presented in the next section, the silicon-air period of each device on the photomask was fixed to a constant value of 4.7 μm. Several different air layer thicknesses were

designed to ensure that some devices yield a high mirror reflectivity in the wavelength range (1500 nm to 1600 nm) used for characterization and refractive index sensing. Indeed, as presented in Figure 4.7 for silicon-air periods of 4.7 µm, high mirror reflectivity is expected in the targeted range for air layers thicknesses around 3.5 µm or 4.15 µm.

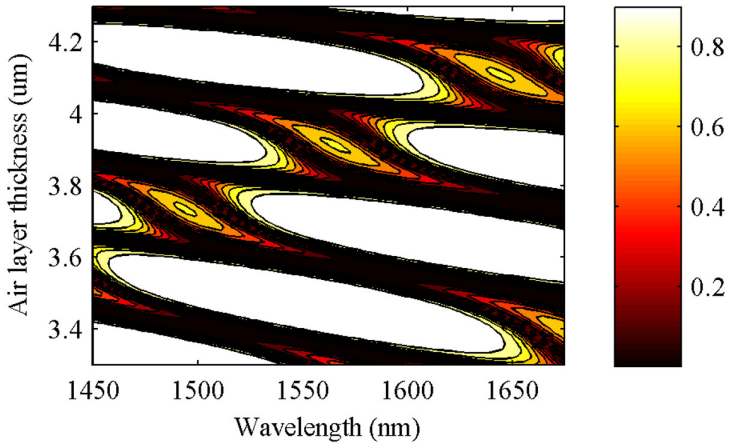

Figure 4.7: Calculated reflectivity of a 2.5 periods mirror having a constant silicon-air period of 4.7 µm, as a function of wavelength and of the air layers thickness. High reflectivity (>0.9) covering the desired wavelength range (1500 to 1600 nm) occurs for air layers thicknesses around 3.5 or 4.15 µm

4.6.2 Results and discussion

A Fabry-Perot refractometer fabricated by contour lithography and based on 2.5 periods mirrors is presented in Figure 4.8 (a). Similar devices, based on 1.5 periods mirrors, were also fabricated and characterized. The measured and calculated transmission spectra, for both designs, are presented in Figure 4.8 (b). As targeted, the reflection band of the mirrors span across the 1500 - 1600 nm wavelength range, where the sharpest resonance peaks are visible. The results were obtained for nominal (i.e.: dimensions on the photomask) thicknesses of the air and silicon layers of 2.8 µm and 1.9 µm, respectively, and for a nominal gap between the mirrors of 35 µm.

The nominal dimensions are of course different from those of the fabricated devices. The dimensions used to simulate the devices in Figure 4.8 (b) were determined using the calculations of Figure 4.7. The silicon-air period was kept constant (4.7 µm) and the air layer thickness was adjusted to reach the best match between the position of the simulated and measured reflection bands. For the 2.5 P devices, the best match was obtained with air layer thicknesses of 4.105 (i.e.:

0.595 μm silicon layers). The gap between the mirrors, which was designed at 35 μm, was consequently increased to 36.305 μm. The characterized 1.5 P device apparently experienced a little more diffraction during lithography and/or undercut during DRIE since the best fit was obtained for dimensions of 4.115 μm (air), 0.585 μm (silicon) and 36.315 μm (gap). This difference could be due to slightly inhomogeneous plasma and/or photomask-wafer contact during photolithography.

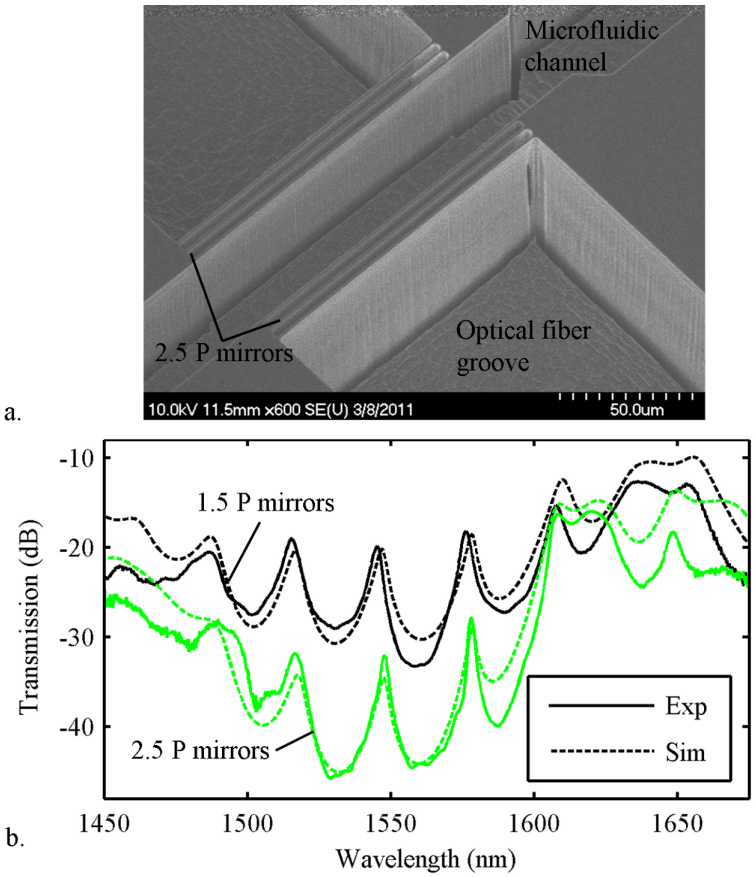

Figure 4.8: (a) Scanning electron micrograph of a Fabry-Perot refractometer fabricated by contour lithography and based on 2.5 periods (P) mirrors. (b) Experimental and simulated transmission spectra of Fabry-Perot refractometers based on 2.5 P (green) and 1.5 P mirrors (black).

To include the effect of surface roughness, a thickness of $2\sigma=2\times30$ nm RMS is subtracted from each layer and a 2σ thick absorbing layer, described by Eq. (4.9), is added at each silicon-air interface. The devices are characterized using cleaved Corning® SMF-28™ single mode

optical fibers. The effect of divergence is therefore taken into account by performing the simulations with a 5 μm Gaussian beam waist.

As shown in Figure 4.8 (b), the simulations correspond closely to the measured transmission spectra. The maximum transmission of the main resonance peaks (i.e.: the peaks located between 1500 nm and 1600 nm) is estimated correctly, within an average error of 1.3 dB. The finesses ($\mathfrak{F}$) of the resonance peaks also correspond to the measurements, within an average error of 25%. The difference between the simulated and experimental results may be due to the glass-air interfaces of the cleaved optical fibers, for which the exact positions are unknown, to the uncertainty on the dimensions of the layers on the photomask (<50 nm according to the mask supplier, Benchmark Technologies), to the uncertainty on the amount of surface roughness (5 nm RMS), or to other imperfections that are not taken into account in the model (see next section).

The model was also used to interpret other structures that are not presented to lighten the text. It allowed the prediction of the finesse within less than 30% of uncertainty and of the losses within 3 dB of uncertainty for the main peaks of the Fabry-Perot tunable filter presented in [21]. It also allowed the interpretation of the loss of the Gires-Tournois interferometer presented in [78] within less than 3 dB of uncertainty. Finally, one-dimensional photonic crystals fabricated by other groups [28, 30] were also simulated. The model allowed the prediction of a decrease of the reflectivity in the bandgap region due to light scattering, an effect that could not be predicted in [30] by treating roughness as a random variation of the layer thicknesses.

In Figure 4.8, the highest finesse ($\mathfrak{F}$ = 12.1) is obtained at λ = 1578 nm for the cavity based on 2.5 periods mirrors. This is a 70% increase (see Table 4.1) compared to previous works on refractive index sensors [60] having similar dimensions. It is possible that the contour lithography fabrication method allowed lower surface roughness on the silicon surfaces that face large openings (optical fiber alignment grooves, microfluidic channels), as previously reported [62]. It is also possible that the oxidation step of the contour lithography method (Figure 4.6, step b) reduced surface roughness at the silicon-air interfaces [72]. The reached finesse is, however, lower than what was previously obtained with Fabry-Perot cavities based on smaller gaps [19, 21] or incorporating focusing optics [27]. The impact of divergence was most likely less important in these cases, which allowed higher finesses, as predicted in Figure 4.3 for shorter cavities (lower m_{Gap}).

In Figure 4.8 (b), the finesse reached with 2.5 P mirrors ($\mathfrak{F}$=12.1), is 70% higher than with the 1.5 P device ($\mathfrak{F}$=7.0). However, this relatively modest increase occurs at the expense of signal losses of more than 10 dB. This result tends to indicate that, for a given amount of surface roughness, there is an optimal number of layers above which small finesse improvements occur at the expense of important signal losses. This condition can be predicted using the roughness model. In Figure 4.9, the finesse and peak transmission at resonance are reported as a function of surface roughness for resonators based on various numbers of silicon-air periods. The calculations are performed with (m_{Si}, m_{Air}) = (17, 5) nominal mirrors dimensions, but the results would be essentially the same for any other (m_{Si}, m_{Air}) odd integers. The calculations are also valid for any cavity length (i.e.: any m_{Gap} dimension constant). Above a given amount of roughness, the reflectivity of the Bragg mirrors, and hence the finesse, is not increased anymore by adding additional Bragg periods. For example, in Figure 4.9, the finesse for 2.5 and 3.5 period mirrors is essentially the same when surface roughness is superior to 10 nm RMS. Therefore when Bragg mirrors are to be used in transmission (such as for Fabry-Perot filters) the choice of the number of Bragg periods should be dictated by the lowest level of surface roughness that can be reached experimentally.

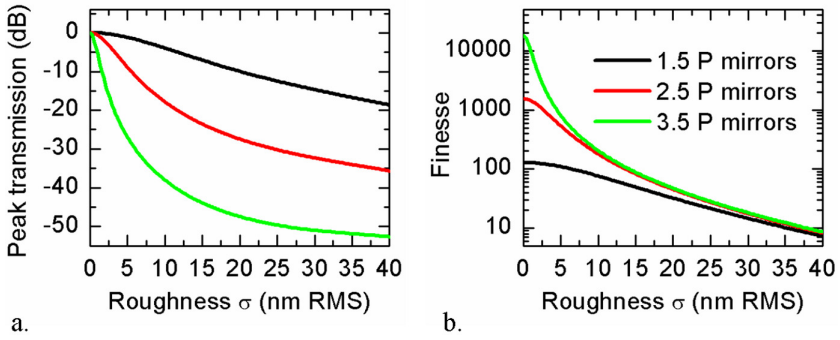

Figure 4.9: Peak transmission (a) and finesse (b) of a (m_{Si}, m_{Air}) = (17, 5) Fabry-Perot resonator of infinite beam waist (ω_0) as a function of surface roughness and for different numbers of Bragg periods (P) in each mirror.

4.7 Other sources of loss

The correspondence between the model and the experimental results in Figure 4.8 tends to demonstrate that, for the reported devices, surface roughness and beam divergence are the

dominant sources of loss. However, if surface roughness was decreased and if a larger beam waist was used, other sources of loss would probably become non-negligible.

For Fabry-Perot cavities based on stacked thin films reflectors, curvature and imperfect parallelism between the mirrors affect the finesse in a similar way as surface roughness does. For example, a 10 nm deviation of the distance between the mirrors due to imperfect parallelism—which would corresponds to an angle of 0.06° for a mirror diameter of 10 μm—is expected to induce roughly the same decrease of finesse as the presence of 10 nm RMS surface roughness [51].

In the particular case of resonators based on deep-etched Bragg reflectors, curvature or imperfect parallelism between the silicon-air interfaces should also affect the finesse. In [24], imperfect parallelism is considered to occur between the two mirrors (i.e.: verticality deviations inside the Bragg mirrors are neglected) and is simulated by summing the amplitude and phase of the Gaussian beam after each roundtrip in the cavity. For cavities based on 2.5 periods Bragg mirrors, a deviation of verticality of 0.005° is expected to induce roughly the same decrease of finesse as the presence of 5 to 10 nm of surface roughness in Figure 4.9. However, for deep-etched Fabry-Perot resonators, the influence of imperfect parallelism between the Bragg mirror material interfaces, rather than between the mirrors themselves [24, 51] is not treated in the literature and is therefore a subject that remains to be explored.

4.8 Conclusion

Gaussian beam divergence in deep-etched multilayer resonators was demonstrated to induce more loss than what was previously reported in [24]. The underestimation is especially important for smaller beam waist, reaching around 10 dB for the waist of cleaved single mode optical fibers. The model for divergence was corrected and was combined with the single layer model for surface roughness proposed in [61].

The combined model was compared with the measured transmission spectra of Fabry-Perot resonators fabricated using the contour lithography method [62]. This technique—which was originally intended for the integration of nanometer and millimeter-scale structures—is also found to greatly improve the predictability of the dimensions of deep-etched multilayered

structures. This improvement allowed the comparison of simulated and experimental results without errors due to undetermined optical layers thicknesses.

The correspondence of the combined model with experimental results tends to demonstrate that surface roughness is among the dominant source of loss in deep-etched silicon-air multilayer resonators, at least for the reported devices. We therefore conclude that the presence of surface roughness, which is inherent to most silicon etching techniques, should be taken into account during the design of deep-etched multilayer resonators. The single absorbing layer model [61]—coupled with roughness profiles measured by white light interferometric surface profiling—is found to be appropriate for this purpose. We demonstrated that it can conveniently be combined with the corrected model for Gaussian beam divergence. It also takes into account light scattering, which is expected to be important for the large refractive index contrast between silicon and air.

In summary, the combined model for beam divergence and surface roughness presented in this article is found to correspond closely to experimental results. It is therefore expected to provide useful design guidelines for the optimization of devices based on deep-etched optical resonators. We also provide a design technique—based on the contour lithography fabrication method—that allows the fabrication of deep-etched multilayer structures having predictable dimensions and optical characteristics. This design technique could therefore lead to an improvement of the fabrication yield of deep-etched optical resonators.

4.9 Supplementary information: Extended discussion on other sources of loss

4.9.1 Optical fiber misalignment

Passive alignment grooves, such as those presented in Figure 4.8 (a) greatly simplify the coupling of in-plane resonators with optical fibers. However, input and output fibers are still subject to misalignment, as schematized in Figure 4.10. For example, the width of the grooves (130 μm) is set to a higher value than the diameter of conventional single mode optical fibers (125 μm) to facilitate fiber insertion. The depth of each groove is also subject to variations caused by the fabrication process or by the presence of surface-adsorbed contaminations. Finally, the SMF-28^{TM} single mode optical fibers used in this work are subject to core-cladding eccentricities up to 0.5 μm and to cladding diameter variations up to 0.7 μm [54].

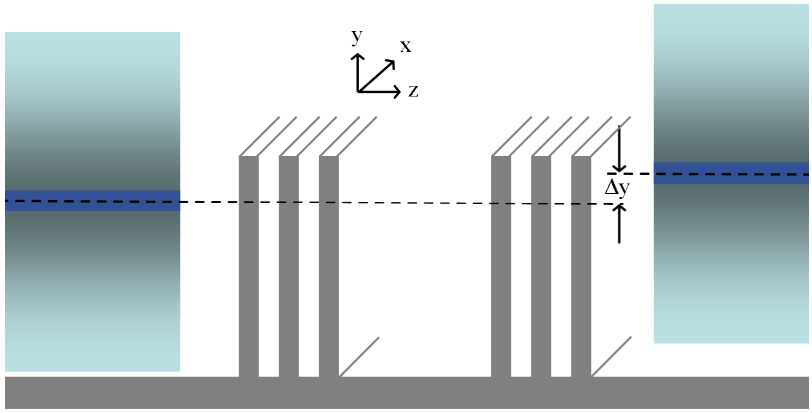

Figure 4.10: Schematic representation cross section view of a Fabry-Perot cavity coupled with optical fibers misaligned by a Δy lateral offset.

The fiber alignment grooves are very long (typically 5 mm) compared to plausible misalignment values (Δy) between the fibers (<10 μm). We therefore expect misalignment angles smaller than 0.12°. This is almost two orders of magnitude smaller than the numerical aperture (NA) of conventional SMF-28^{TM} single mode fibers (5.6°) and five time smaller than the smallest NA (i.e.: NA = 0.63° for ω_0 = 45 μm) considered in this chapter (see Figure 4.3). In this context, we expect negligible losses due to angular misalignments [68], which are therefore neglected in

this section. We consider only lateral offset (Δy), as presented in Figure 4.10, to occur between the input and output optical fibers.

It is possible to predict the effect of a lateral offset (Δy) between the input and output fibers by slightly modifying the formalism developed in section 4.4. From the translation property of Fourier transforms, if the axis of propagation of the output fiber is off-centered by a distance Δy relative to the origin, its angular distribution of plane wave, (originally described by Eq. (4.2)) is multiplied by a factor $e^{-ik_y \Delta y}$ and becomes:

$$\tilde{E}_{OutputFiber}(k, k_x, k_y, z) = -\frac{q_0}{\omega_0}\frac{2\pi i}{k}\exp\left(-i\frac{q(z)\left(k_x^2 + k_y^2\right)}{k} - ikz - ik_y \Delta y\right), \tag{4.10}$$

which we rewrite in polar coordinates to be consistent with the previously established notation:

$$\tilde{E}_{OutputFiber}(k, k_t, \theta, z) = -\frac{q_0}{\omega_0}\frac{2\pi i}{k}\exp\left(-i\frac{q(z)k_t^2}{k} - ikz - ik_t \Delta y \sin\theta\right). \tag{4.11}$$

We can therefore rewrite Eq. (4.6) as:

$$T(\lambda_0), R(\lambda_0) = \frac{\left|\left\langle \tilde{E}_{out} \middle| \tilde{E}_{fiber} e^{-ik_t \Delta y \sin\theta} \right\rangle\right|^2}{\left\langle \tilde{E}_{fiber} \middle| \tilde{E}_{fiber} \right\rangle^2}. \tag{4.12}$$

In Eq. (4.12), as in Eq. (4.6), the bracket notation denotes the scalar product of two electric fields. Because of the lateral offset (Δy) between the optical fibers, the circular symmetry of the problem is lost and this product must now be calculated in two dimensions. Eq. (4.7) is therefore rewritten as:

$$\left\langle \tilde{E}_1 \middle| \tilde{E}_2 \right\rangle = \int_0^{2\pi}\int_0^{k} \tilde{E}_1 \tilde{E}_2^* k_t \, dk_t \, d\theta. \tag{4.13}$$

Using the formalism of Eq. (4.10)-(4.13), we can predict the influence of lateral misalignment on the peak transmission at resonance and on the finesse of typical deep-etched

Fabry-Perot resonators. Using Eq. (4.9), the presence of surface roughness at the silicon-air material interfaces of these resonators can also be considered simultaneously.

The calculations are first performed for short cavity lengths (low m_{Gap}, large FSR), which are more representative of works related to tunable Fabry-Perot filters [12, 18-21]. The dimension parameters are set to (m_{Si}, m_{Air}, m_{Gap}) = (17, 5, 3), and the Gaussian beam waist is set to that of cleaved SMF-28^{TM} single mode fibers (ω_0 = 5 μm). The results are presented in Figure 4.11 and Figure 4.12, which correspond respectively to resonators having 0 and 20 nm RMS surface roughness at their material interfaces.

When no roughness is considered (Figure 4.11), fiber misalignment is found to influence more resonators based low numbers of Bragg periods (P). For example, in Figure 4.11 (a), a Δy = 5 μm misalignment causes losses of -2.3 dB for devices based on 1.5 periods mirrors but causes losses smaller than -1 dB for devices based on 2.5 or 3.5 periods mirrors. In the latter cases, light is more strongly confined in the cavities (i.e.: finesse is high), which allow the beam to diverge on a longer effective distance before coupling to the output optical fiber. The effective diameter of the output beam is therefore large compared to the lateral offset Δy, such that losses caused by fiber misalignment tend to become negligible compared with divergence losses.

Interestingly, in Figure 4.11 (b), finesse increases with the lateral offset between the fibers. As misalignment increases, the output fiber collects preferably light that is in resonance and that could consequently diverge on a longer distance to compensate for the Δy misalignment. This increase of the finesse is however relatively modest (<20% for Δy = 5 μm) unless intentionally using large Δy values that would cause important signal losses.

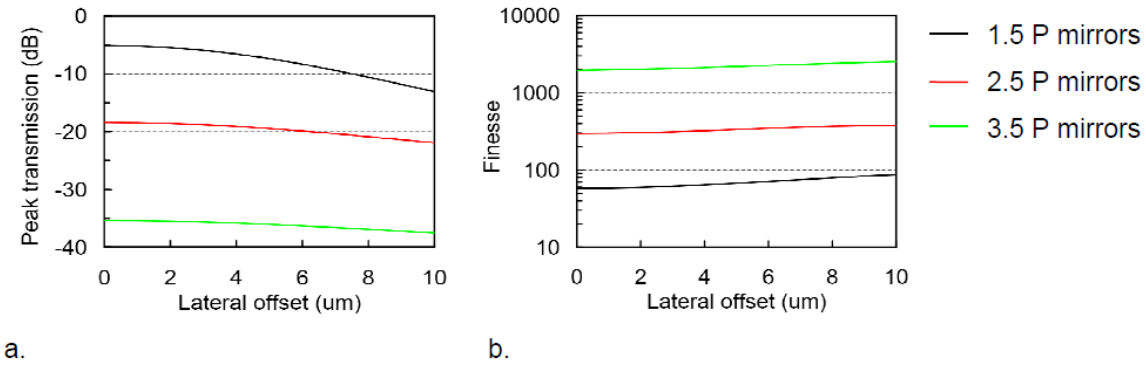

Figure 4.11: Peak transmission (a) and finesse (b) of the central (λ_c = 1550 nm) Fabry-Perot resonance peak as a function of the lateral offset (Δy) between the optical fibers, and for various numbers of silicon-air periods (P) in each mirror. The calculations are performed with (m_{Si}, m_{Air}, m_{Gap}) = (17, 5, 3) dimension parameters (i.e., short cavity), with a ω_0 = 5 μm Gaussian beam waist, and without (0 nm RMS) surface roughness at the silicon-air material interfaces.

In Figure 4.12, the effect of fiber misalignment is calculated again for short cavities (low m_{Gap}, large FSR) but now considering 20 nm RMS surface roughness at the silicon-air material interfaces. In this case, as discussed in sections 4.5-4.6, surface roughness strongly reduces the confinement of light in the cavities, regardless of the number of periods in the Bragg mirrors (i.e. all curves in Figure 4.12 (b) yield similar finesses < 35 for Δy = 0). Consequently, peak transmission at resonance (Figure 4.12 (a)) yields similar behavior for 1.5, 2.5, or 3.5 period mirrors. In particular, misalignment losses of -3 dB, for any number of Bragg periods (P), are obtained for the lateral offset (Δy = 5 μm) expected from the mismatch between the alignment grooves width (130 μm) and the fiber diameter (125 μm). For Δy = 5 μm, the finesse also increases by approximately 15%, for the same reasons as in Figure 4.11 (b).

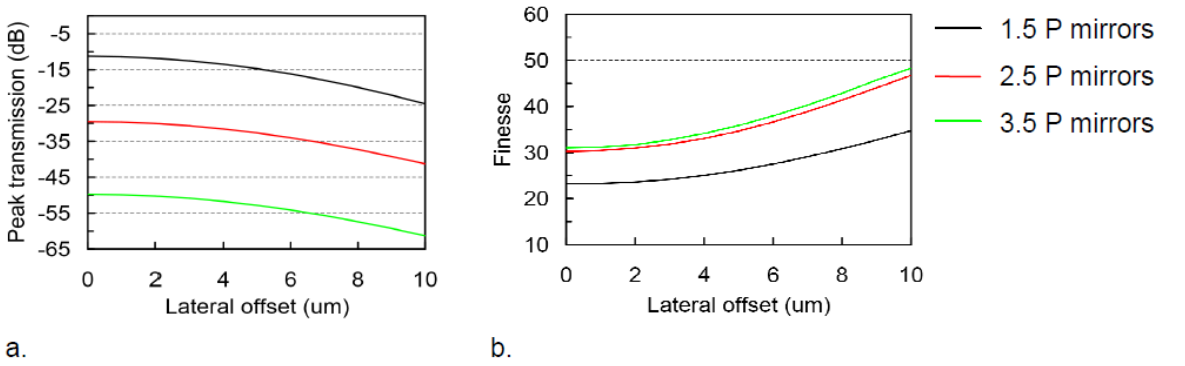

Figure 4.12: Peak transmission (a) and finesse (b) of the central (λ_c = 1550 nm) Fabry-Perot resonance peak as a function of the lateral offset (Δy) between the optical fibers. The parameters are the same as in Figure 4.11 (i.e., short cavity), except for the presence of 20 nm RMS surface roughness at the silicon-air material interfaces.

In Figure 4.13 and Figure 4.14 the influence of fiber misalignment is calculated for longer cavities (large m_{Gap}, low FSR), which are more representative of our work on deep-etched Fabry-Perot sensors [60, 79] (see next two chapters). The dimension parameters are set to (m_{Si}, m_{Air}, m_{Gap}) = (17, 5, 50), and the Gaussian beam waist is still set to ω_0 = 5 μm.

Figure 4.13 presents calculations performed without surface roughness, while Figure 4.14 considers 20 nm RMS at the silicon-air interfaces. In both cases, the general behavior is similar to the results obtained above (Figure 4.11, Figure 4.12) for shorter cavities. When no roughness (Figure 4.13) is considered, a Δy = 5 μm lateral offset causes losses at resonance between -1.1 dB (for 1.5 P mirrors) and -0.45 dB (for 3.5 P mirrors), and finesse increases between 11% (1.5 P mirrors) and 19% (3.5 P mirrors). When surface roughness is added to the model (Figure 4.14), the same Δy = 5 μm offset causes losses of -1.5 dB and finesse increases of 13%, regardless of the number of periods in the mirrors.

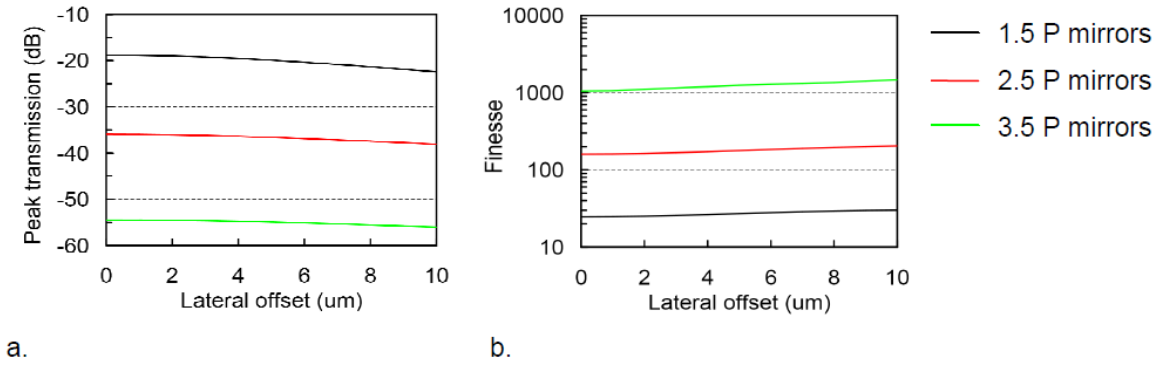

Figure 4.13: Peak transmission (a) and finesse (b) of the central (λ_c = 1550 nm) Fabry-Perot resonance peak as a function of the lateral offset (Δy) between the optical fibers, and for various numbers of silicon-air periods (P) in each mirror. The calculations are performed with (m_{Si}, m_{Air}, m_{Gap}) = (17, 5, 50) dimension parameters (i.e., long cavity), with a ω_0 = 5 μm Gaussian beam waist, and without (0 nm RMS) surface roughness at the silicon-air material interfaces.

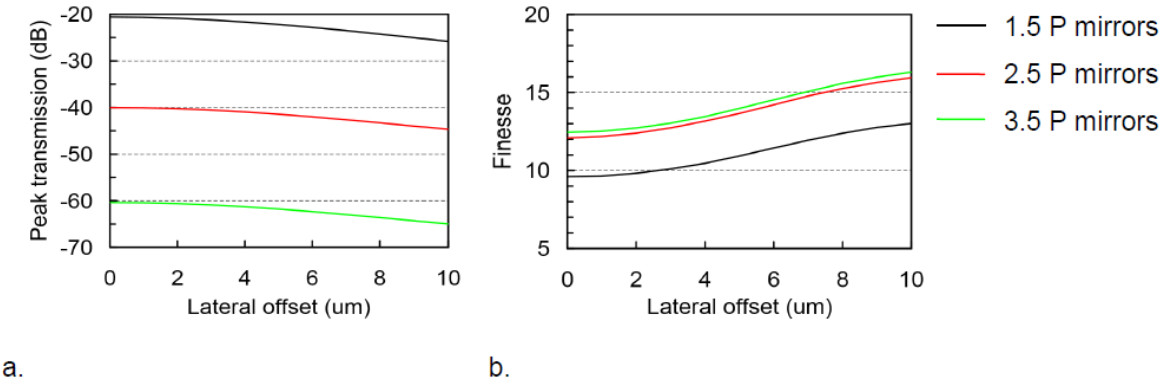

Figure 4.14: Peak transmission (a) and finesse (b) of the central (λ_c = 1550 nm) Fabry-Perot resonance peak as a function of the lateral offset (Δy) between the optical fibers. The parameters are the same as in Figure 4.13 (i.e., long cavity), except for the presence of 20 nm RMS surface roughness at the silicon-air material interfaces.

From the results presented in Figure 4.14 (long cavity with surface roughness), we can state that a typical Δy ~5 µm misalignment error should not influence significantly the performances of the free-space interferometers presented above (section 4.6.2) and in the next two chapters. For example, in Figure 4.15, the results and simulations previously reported in section 4.6.2 are now compared with simulations accounting for a 5 µm misalignment error.

Compared to the original simulations, the model including misalignment does not yield a significantly higher mismatch with the experimental results.

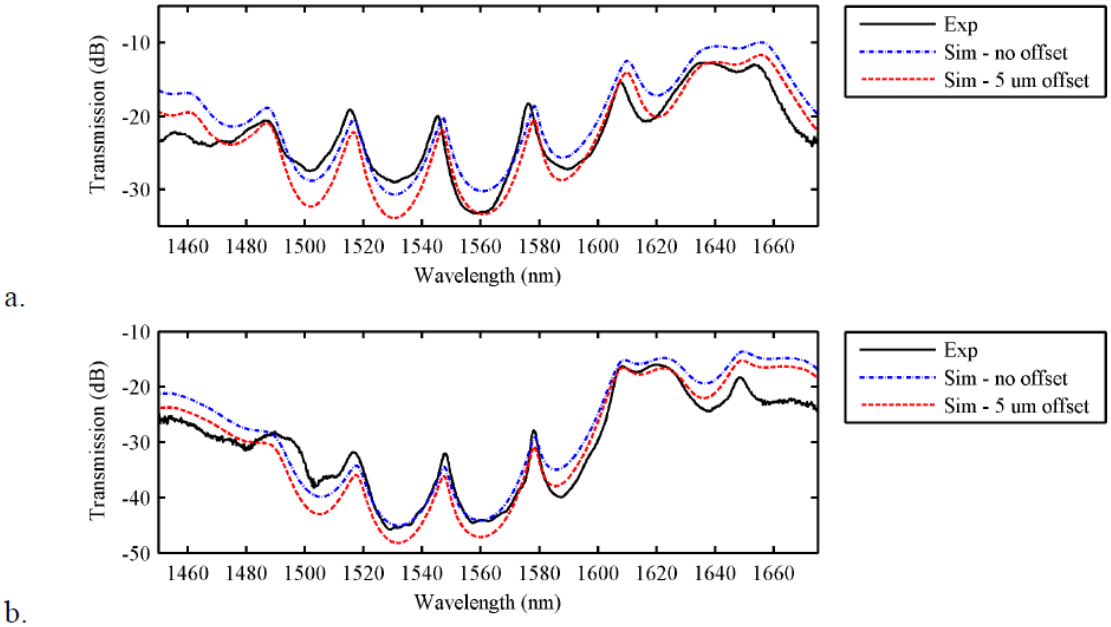

Figure 4.15: Same simulations and experimental results as reported in Figure 4.8, but now compared with simulations that accounts for a 5 μm misalignment between the incident and output optical fibers. (a) Fabry-Perot cavity based on mirrors having 1.5 silicon-air periods. (b) Fabry-Perot cavity based on mirrors having 2.5 silicon-air periods

Finally, simulations were also performed using a ω_0 = 20 μm Gaussian beam waist, for which the influence of fiber misalignment was found to be much less important than with a smaller ω_0 = 5 μm waist. For all the dimensions and the amounts of surface roughness previously used in Figure 4.11-Figure 4.14, and considering a Δy = 5 μm lateral offset, the losses at peak transmission and the finesse increases are smaller than -0.3 dB and 5%, respectively.

In summary, for free-space Fabry-Perot cavities, lateral offsets between the input and output optical fibers is predicted to yield small but measurable finesse variations and peak transmission losses at resonance. These variations are predicted to be more important for cavities that weakly confine light (i.e. cavities having low finesses caused by surface roughness, or

smaller number of Bragg periods), and for cavities coupled with optical fibers having smaller Gaussian beam waists. The case of longer cavities (large m_{Gap}, low FSR) suffering from surface roughness at their material interfaces and coupled to cleaved single mode optical fibers (ω_0 = 5 μm) is of particular interest for our work on sensors [60, 79] presented in the next two chapters. In this case—and for the typical lateral offset (Δy = 5 μm) expected from the mismatch between the alignment grooves width (130 μm) and the optical fibers diameter (125 μm)—losses at resonance of -1.5 dB and finesse increases of 13% can be expected (Figure 4.14). Misalignment losses are therefore not expected to be significant compared to the other sources of loss (Gaussian beam divergence, surface roughness) that affect our devices.

4.9.2 Verticality deviation of the etch profiles

As discussed previously in Chapter 2 (section 2.3), perfect parallelism between each material interface of multilayer silicon-air resonators can not be guaranteed by inductively coupled plasma (ICP) etching. In [24], the consequence of such verticality deviation on the optical response of deep-etched Fabry-Perot resonators is modeled by considering that imperfect parallelism occurs only between the two mirrors, while verticality deviations inside the mirrors themselves are neglected. We therefore propose, in this section, an alternate model that accounts for both effects. However, this alternate model can not consider simultaneously beam divergence with verticality deviation, which was possible in [24]. Both models are therefore of interest for the modeling of deep-etched multilayer optical resonators.

As schematized in Figure 4.16, if the silicon-air material interfaces are misaligned by an angle φ with respect to the vertical axis, the light beam will interact with layers that present inconstant thicknesses over the beam diameter ($2\omega_0$). We expect three consequences to arise from this:

1. The portions of the beams that interact with thicker silicon layers (i.e. the top portions in Figure 4.16) will accumulate more phase than the portions that interact with thinner layers, due to the higher refractive index of silicon. Fabry-Perot resonance will therefore occur at different wavelengths as a function of the y coordinate in Figure 4.16, such that the effective fiber-to-fiber response will be an average of Fabry-Perot resonance peaks

centered at different wavelengths. The measured response should therefore suffer from peak broadening (i.e. reduced finesse) and reduced peak transmission.

2. As the beam is transmitted through the multilayer assembly, its angle of propagation (relative to the z axis in Figure 4.16) should change by a magnitude proportional to the φ misalignment error. This variation of the angle of propagation should reduce the coupling efficiency of the transmitted light with the output optical fiber, as is the case, for example, for angle misalignments between optical fiber collimators [68].

3. This same variation of the angle of propagation should cause the transmitted beam to accumulate a lateral offset relative to the core of the output optical fiber.

As we deal with very small φ angles, and as we demonstrated in section 4.9.1 that lateral offsets have limited impacts of the response of deep-etched Fabry-Perot resonators, we expect the third consequence to be negligible relative to the first two. The following calculations therefore accounts only for the first two expected effects of imperfect verticality.

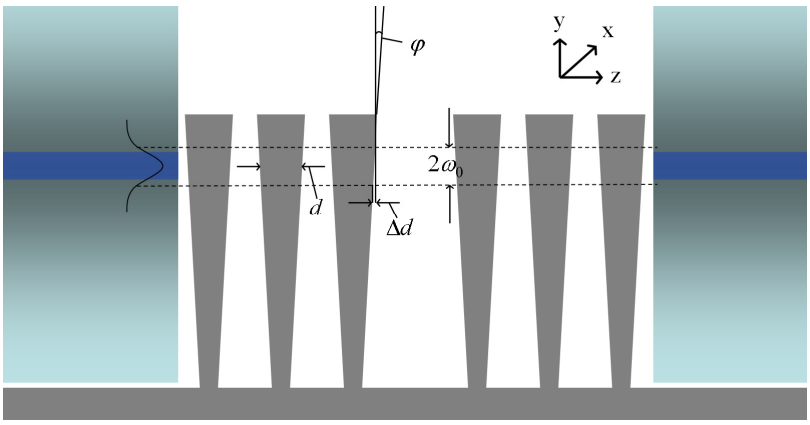

Figure 4.16: Schematic cross section view of a deep-etched Fabry-Perot interferometer in which the optical planes are misaligned by an angle φ relative to the vertical axis. This angle causes a Δd variation of the layer thicknesses, over the $2\omega_0$ beam diameter, at each material interface.

As we deal with layers of varying thicknesses as a function of their y coordinate, we choose to treat the Gaussian beam in the (x, y) space (see Eq. (4.1), repeated below), rather than using its transverse wave vector (k_x, k_y) Fourier transform. Consequently, the following

calculations can not be used to consider simultaneously the effect of Gaussian beam divergence with imperfect verticality.

$$E(k,x,y,z) = \frac{q_0}{\omega_0}\frac{1}{q(z)}\exp\left(-ik\frac{x^2+y^2}{2q(z)} - ikz\right) \tag{4.1}$$

We also choose to discuss the effect of the misalignment angle φ in term of the quantity Δd, which we define as the variation of the layers thickness, at each material interface, over the $2\omega_0$ Gaussian beam diameter (see Figure 4.16). Considering small verticality deviations, Δd is function of φ through:

$$\Delta d = 2\omega_0\varphi\,. \tag{4.14}$$

Since we do not consider divergence ($k_x = k_y = k_t = 0$), the transfer matrix formalism of Eq. (4.3) can be rewritten as:

$$\begin{bmatrix} B \\ C \end{bmatrix} = \left\{\prod_{r=1}^{p}\begin{bmatrix} \cos\delta_r & (i\sin\delta_r)/N_r \\ iN_r\sin\delta_r & \cos\delta_r \end{bmatrix}\right\}\begin{bmatrix} 1 \\ N_{out} \end{bmatrix}, \tag{4.15}$$

with $\delta_r = 2\pi N_r d_r(y)/\lambda_0$. In Eq. (4.15), the thickness of each layer (d_r) is now a y dependant parameter:

$$d_r(y) = d + J2\varphi y = d + J\frac{\Delta d}{\omega_0}y\,, \tag{4.16}$$

where J=1 for silicon layers, J=-1 for air layers, and J=0 for virtual surface roughness layers, if included in the calculations. The amplitude transmission (t) and reflection (r) coefficients, previously expressed as in Eq. (4.5), are now also y dependant parameters expressed as:

$$\begin{aligned} r(\lambda_0,y) &= \frac{N_{inc}B - C}{N_{inc}B + C}, \\ t(\lambda_0,y) &= \frac{2N_{inc}}{N_{inc}B + C}. \end{aligned} \tag{4.17}$$

Finally, as in (4.6), the fiber-to-fiber response of the interferometesr can be expressed as:

$$T(\lambda_0), R(\lambda_0) = \frac{\left|\left\langle E_{out} \middle| E_{fiber} \right\rangle\right|^2}{\left\langle E_{fiber} \middle| E_{fiber} \right\rangle^2}, \tag{4.18}$$

with:

$$E_{fiber} = E\left(\frac{2\pi}{\lambda_0}, x, y, 0\right),$$

$$E_{out}\left(\frac{2\pi}{\lambda_0}, x, y, 0\right) = E_{fiber} \cdot t(\lambda_0, y) \text{ (transmission)}$$

$$E_{out}\left(\frac{2\pi}{\lambda_0}, x, y, 0\right) = E_{fiber} \cdot r(\lambda_0, y) \text{ (reflection)}$$

In this case, the overlap integral between the electric fields (denoted by the bracket notation in Eq. (4.18)) is now performed in the (x, y) space rather than in the (k_x, k_y) space. Equation (4.7) is therefore rewritten as:

$$\left\langle E_1 \middle| E_2 \right\rangle = \int_{-\infty}^{\infty}\int_{-\infty}^{\infty} E_1 E_2^* dxdy\,. \tag{4.19}$$

In Figure 4.17, the model presented above is used to predict the influence of Δd verticality deviations on the finesse and the peak transmission of Fabry-Perot interferometers based on various numbers of silicon-air periods. The calculations are performed using (m_{Si}, m_{Air}, m_{Gap}) = (17, 5, 50) dimension constants and a ω_0 = 5 μm Gaussian beam waist. However, these parameters are found to have very little influence on the calculated results, such that the values presented in Figure 4.17 are valid for any (m_{Si}, m_{Air}, m_{Gap}) dimension constants. The calculated results are also valid for any Gaussian beam waist. However, for a given etch angle φ, the Δd value must be adjusted proportionally with beam waist (i.e., for a given etch angle φ, the Δd value increases with the Gaussian beam waist, as shown in Eq. (4.14)).

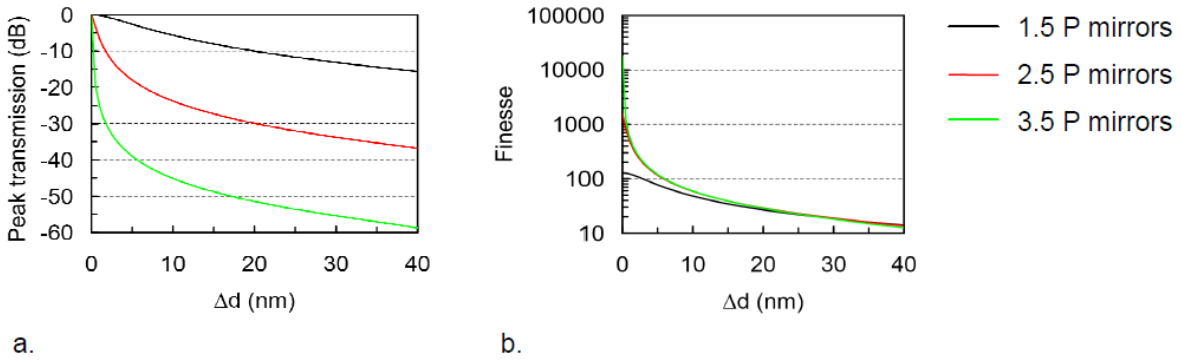

Figure 4.17: Peak transmission (a) and Finesse (b) of Fabry-Perot resonators as a function of verticality deviation (Δd), for various numbers of silicon-air periods (P) in each mirror. The results are independent of the (m_{Si}, m_{Air}, m_{Gap}) dimension constant and of the Gaussian beam waist

Verticality deviations are found to influence finesse and peak transmission in a similar way as surface roughness does (see Figure 4.9). As Δd increases, resonators based on larger number of silicon-air periods suffer from higher insertion loss and faster finesse decrease than resonators based on small number of periods. Above Δd = 1 nm (i.e. above φ = 0.005° for a ω_0 = 5 μm Gaussian beam waist), resonators based on 3.5 periods mirrors do not allow significant finesse increases compared to 2.5 period mirrors resonators. Similarly, above Δd = 20 nm (0.11° for ω_0=5 μm), resonators based on 2.5 periods mirrors do not allow finesse increases compared to 1.5 periods resonators. For applications such as tunable filters that require low insertion losses, resonators based on smaller number of silicon-air periods are therefore preferable. Peak transmission losses smaller than -3 dB require Δd < 6 nm for resonators based on 1.5 period mirrors, Δd < 0.5 nm for 2.5 P mirrors devices, and a most certainly impracticable Δd < 0.05 nm for 3.5 P mirrors.

Considering a ω_0 = 5 μm Gaussian beam waist, these Δd values (< 6 nm) correspond to misalignment angles smaller than 0.04°, which is significantly smaller than the corresponding 5.7° numerical aperture of the optical fibers. Of the three consequences of imperfect verticality listed above, the second one (shift of the propagation angle of the beam relative to the output

fiber) is therefore most likely not a significant factor compared to the first (y dependant resonance wavelength due to thickness variations of the layers).

Interestingly, for Fabry-Perot interferometers based on 2.5 periods mirrors, the values listed above for insertion loss < -3 dB and finesse decreases < 50% correspond remarkably well with the model proposed in [24]. However, as this model was not used to predict the effect of imperfect verticality for more than a few φ values, or for interferometers based on 1.5 or 3.5 periods mirrors, we cannot draw further conclusions on its correspondence with our calculations.

In Figure 4.18, the effect of Δd verticality deviations is calculated again using the same parameters as in Figure 4.17, but now including 30 nm RMS surface roughness at material interfaces (as measured by white light interferometry in Figure 4.4). Verticality deviations are found to have less influence in this case since light interacts less strongly with the cavity, due to the presence of surface roughness. For Δd < 20 nm relative peak transmission and finesse reductions of less than -3 dB and 40 %, respectively, can be expected.

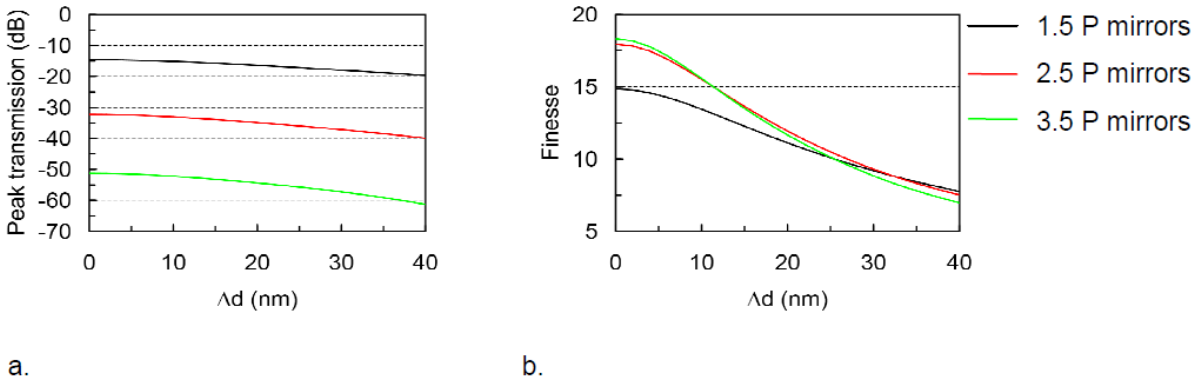

Figure 4.18: Peak transmission (a) and Finesse (b) of Fabry-Perot resonators as a function of verticality deviation (Δd), for various numbers of Bragg periods (P) in each mirror and considering 30 nm RMS roughness at the silicon-air material interfaces.

Verticality deviations in fabricated structures are found to be much more difficult to measure than surface roughness values, for which white light interferometry was successfully used above (Figure 4.4). The only available method consists of evaluating the parallelism from scanning electron microscope (SEM) pictures of cleaved test structures (Figure 4.19 a, b) that are

etched in the same conditions as the Fabry-Perot resonators. However, the precision of this technique is limited by the need to measure a few nanometers of variations of the layers thickness (Δd) on a vertical range that is several orders of magnitudes larger ($2\omega_0$ = 10 000 nm) and that consequently require operation at relatively low magnification. The exact location of the material interfaces in the SEM pictures (Figure 4.19 a, b) can also be difficult to locate since cleaving of silicon with a diamond tip tend to produce randomly non-vertical planes. The cleaved structures in Figure 4.19 (a, b) can therefore be at varying depths in the image, such that it is impossible to have a perfect focus on all the field of view of the microscope. The high depth of focus of scanning electron microscopes however mostly overcomes this limitation.

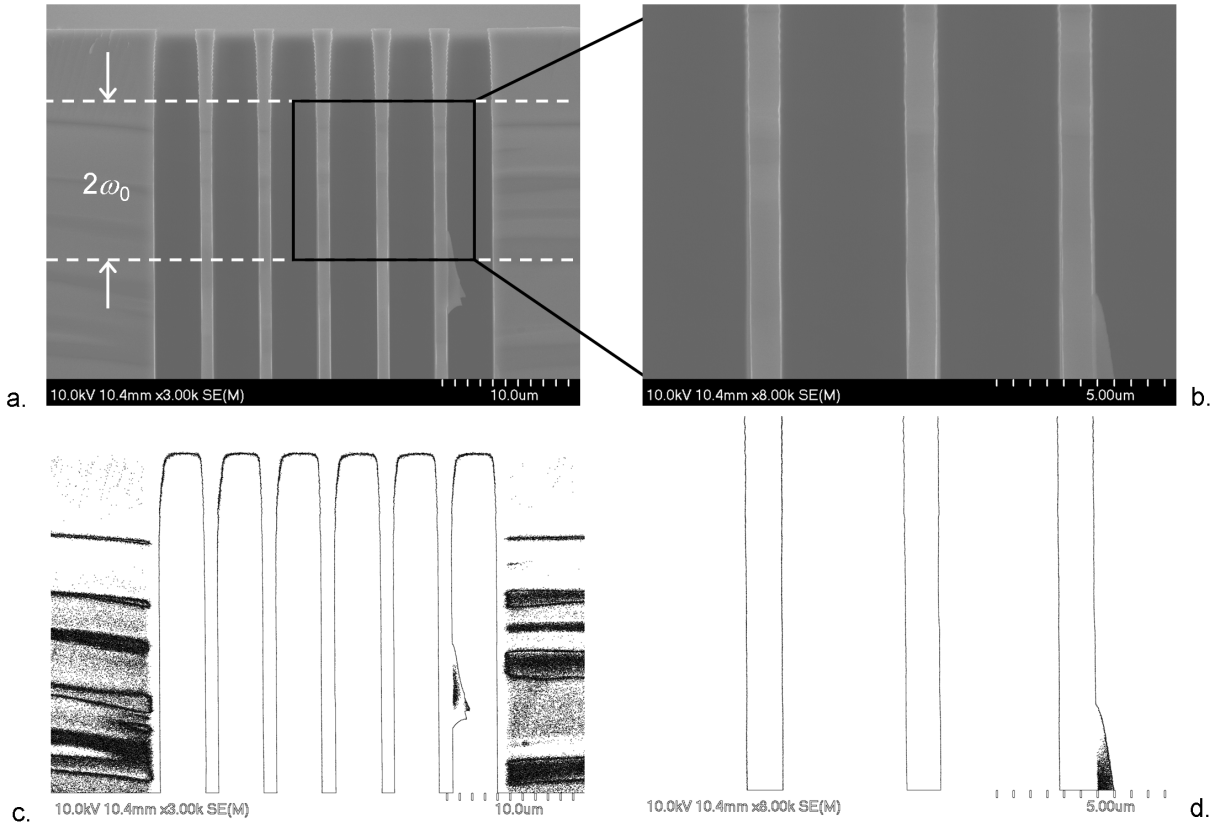

Figure 4.19: (a, b) Scanning electron microscope pictures of cleaved test structures fabricated in the same conditions as the Fabry-Perot interferometer presented in Figure 4.8. The expected width and position of the ω_0 = 5 μm Gaussian beam waist are indicated by white dashed lines. (c, d) Same SEM images processed using the "Find Edges" function of ImageJ image processing and analysis software.

In order to extract verticality deviation values from SEM pictures (Figure 4.19 a, b), the SEM image files are processed using the "Find Edges" function of ImageJ image processing and analysis software [80]. The processed images are presented in Figure 4.19 (c, d). The thickness of the silicon layers in Figure 4.19 (d) was measured at all depth by steps of 1 μm. The edge angle was subsequently determined by fitting the measured thicknesses with a 1st order polynomial. An average Δd = 7 nm verticality (φ = 0.04°) deviation was obtained for all three layers.

In this context, by comparing the effect of σ = 30 nm RMS surface roughness (Figure 4.9) with a Δd = 7 nm verticality deviation (Figure 4.17), we expect surface roughness to be the dominant cause of loss and finesse decrease. This is most likely the reason why, in Figure 4.8, simulated results that considered only surface roughness and beam divergence (i.e. that did not consider verticality deviations) corresponded very accurately with experimental results. Of course, if improvements of our fabrication process allowed a significant reduction of surface roughness, verticality deviation would most likely become a non-negligible parameter for the design and simulation of deep-etched silicon-air multilayer resonators. Moreover, as presented in Eq. (4.14), if a larger Gaussian beam waist (ω_0) was used to characterize the same fabricated structures, the Δd value would increase proportionally (for a constant etch angle φ) and losses due to verticality deviations could become more important than losses due to surface roughness.

In summary, verticality deviations of the etch profiles can strongly affect the performances of deep-etched multilayer optical resonators. As for surface roughness, reductions of peak transmission and finesse are expected to be more important for resonators based on more silicon-air periods. For a given etch angle (φ), increasing the Gaussian beam waist (ω_0) is also predicted to decrease peak transmission and finesse. For the experimental results presented in the current chapter (Figure 4.8), a Δd = 7 nm verticality deviation was measured by scanning electron microscopy on cleaved test structures, which were fabricated in the same conditions as the reported interferometers. In this context, and considering the 30 nm RMS surface roughness measured on the same test structures (Figure 4.4), peak transmission and finesse reductions are predicted to be mainly due to surface roughness. As shown in Figure 4.18, adding a Δd = 7 nm verticality deviation to a resonator that already suffers from 30 nm RMS surface roughness causes negligible losses and finesse reduction (less than -1 dB and 10%, respectively). This explains why, in Figure 4.8, a model taking into account only Gaussian beam divergence and

surface roughness (i.e.: neglecting verticality deviations) corresponded very accurately with the experimental results. As all the resonators presented in the next chapters suffer from large amounts of surface roughness, we will generally neglect verticality deviation in our calculations. However, one should always keep in mind that, upon a significant reduction of the amount of surface roughness or a significant increase of the Gaussian waist, verticality deviation could become a dominant source of loss.

CHAPTER 5 ALL-SILICON INTEGRATED FABRY-PEROT CAVITY FOR VOLUME REFRACTIVE INDEX MEASUREMENT IN MICROFLUIDIC SYSTEMS

This chapter is a reproduction of an article[6] relating the fabrication and characterization of free-space Fabry-Perot interferometers as refractive index sensor for homogenous liquids. Subtitles are not allowed in *Applied Physics Letters* but were added here for the reader's convenience. For more details on the fundamental aspects of deep-etched Fabry-Perot interferometers used as refractive index sensors, please refer also Chapter 3, section 3.1.2.

5.1 Authors and affiliations

Raphael St-Gelais, Jonathan Masson, and Yves-Alain Peter

Department of Engineering Physics, Ecole Polytechnique de Montréal, P.O. Box 6079, Station Centre-Ville, Montréal, Quebec H3C 3A7, Canada

5.2 Abstract

We report a refractive index (RI) sensor based on the use of vertically etched silicon Bragg reflectors. The device is robust and performs measurements through tens of micrometers of liquid. A sensitivity of 907 nm/RIU (RI units) and a resolution of 1.7×10^{-5} RIU are obtained and are in good agreement with optical simulations. This resolution is the highest reported for a volume RI sensor integrated with a microfluidic system. Expected applications for the sensor in the fields of single cell characterization and chip based liquid chromatography are discussed.

---

[6] R. St-Gelais, J. Masson, and Y.-A. Peter, "All-silicon integrated Fabry-Perot cavity for volume refractive index measurement in microfluidic systems," *Appl. Phys. Lett.,* vol. 94, p. 243905, 2009.

5.3 Introduction

Vertically etched silicon Bragg reflectors have been reported recently to create extrinsic tunable Fabry–Pérot filters for optical fibers. The optical path length between two silicon Bragg reflectors has been tuned using the thermooptic effect [12], the electro-optic effect [11], or electrostatic actuation [15, 18, 19, 81] in order to vary the resonance wavelength of a Fabry–Pérot filter. In this letter, we report monolithic integration of a similar silicon Fabry–Pérot resonator to a microfluidic system. In this configuration, the optical path length between the two Bragg mirrors is directly related to the refractive index (RI) of the liquid flowing in the microchannel.

RI measurement in microfluidic systems is of great interest since it is label-free and allows detection of the presence or the nature of liquids and biological samples. In order to compare the numerous available technologies, one should make a clear distinction between surface RI and volume RI measurement. Surface RI sensors are based on the interaction between a sample and an evanescent electromagnetic wave. Surface plasmon, integrated dielectric waveguides, and resonant optical microcavities are important example of this type of sensors. Their resolution can be very high [~10^{-7} RIU for Ref. [82] (RIU denotes RI units)] but the depth of interaction with the sample is typically small (less than 1 μm). This makes them sensitive to surface contamination and unsuitable for applications requiring thick surface functionalization or measurements through bigger biological samples, such as living cells.

Volume RI sensors for microfluidic systems are based on the beam deviation technique [83], on laser cavities [84] or, as for the sensor presented in Figure 5.1, on Fabry–Pérot cavities. In each case, the light propagates through the sample and the depth of interaction is greatly increased. Other microfluidic Fabry–Pérot refractometers were previously reported [85-88] but they have never been made of silicon/air Bragg reflectors fabricated simultaneously with the microfluidic system. This configuration permits a great flexibility in the design of the microfluidic system, minimizes the number of fabrication steps, and allows to reach the highest resolution reported for a volume RI sensor integrated with a microfluidic system.

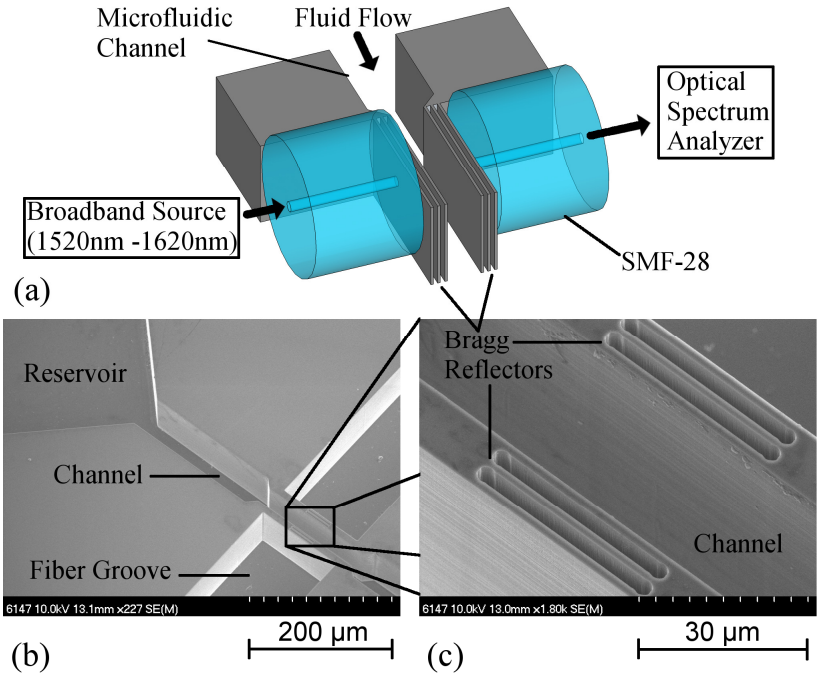

Figure 5.1: (a) Schematic view of the refractometer connected to the measurement setup through SMF-28 single mode optical fibers. (b) SEM photograph of the Fabry-Pérot refractometer integrated with optical fiber alignment grooves, microfuidic channel, and reservoir. (c) Closeup view of the Fabry–Pérot refractometer made of two silicon/air Bragg reflectors separated by the microfluidic channel.

5.4 Methodology

Figure 5.1 presents a schematic view (a) and scanning electron microscope (SEM) photographs [(b) and (c)] of the Fabry–Pérot refractometer integrated with microfluidic elements and optical fiber alignment grooves. The structure is defined by a single photolithography step (SPR220 3.0 photoresist). The silicon is then etched by deep reactive ion etching (DRIE). High verticality and low surface roughness on the optical surfaces (see a detailed discussion on the effect of these imperfections later in the article) are ensured by optimization of the Bosch process, as previously reported [81]. The etch depth is 63 μm in the narrow air layers of the Bragg reflectors and slightly more (80 μm) in the larger openings. This allows insertion of 125 μm diameter conventional SMF-28 single mode optical fibers in the alignment grooves.

Each of the Bragg reflectors is made of three layers of silicon and two layers of air that ensure a high reflectivity [81] because of the large RI contrast ($\Delta n \approx 2.45$). The photomask is

designed with 2.6 and 1.7 μm thick walls for silicon and air, respectively. These dimensions are a compromise between thinner layers, which yield a broader reflection spectrum, and thicker layers, which simplify the fabrication process. With these dimensions, and considering a typical 300 nm undercut of silicon during DRIE, the mirrors have a theoretical reflection bandwidth (R>90%) of 80 nm (see Ref. [81] for more details on the effect of walls thickness on the reflection bandwidth). The length of the cavity (24.5 μm) is chosen to be larger than the thickness of the mirrors (11.1 μm). That way, most of the electromagnetic field of the resonant optical mode is located in the liquid rather than in the mirrors, thus improving the sensitivity [82].

Measurements are performed at room temperature (~21 °C) with certified RI liquids (Cargille Laboratories, series AA) of low temperature dependence (0.0004 $°C^{-1}$). Liquids placed in the reservoir flow in the microchannel by capillary effect and reach the Fabry–Pérot cavity formed by the two Bragg reflectors. Light from a broadband light source (1520–1620 nm) is incident on the Fabry–Pérot through one of the optical fibers placed in the alignment grooves [see Figure 5.1 (a)]. The transmitted light is collected by the second optical fiber, which is connected to an Agilent 86142A optical spectrum analyzer.

5.5 Results and discussion

The experimental and simulated transmission spectrum of the Fabry–Pérot refractometer are presented in Figure 5.2. The simulations are based on the transfer matrix method for multilayered optical systems, combined with the Gaussian approximation of the optical fiber fundamental mode, as proposed in Ref. [19]. The dimensions of the walls are measured in top view with a SEM, showing an increase of about 1.1 μm of the thickness of the air layers caused by diffraction during photolithography. This is taken into account in the simulations, as well as the typical 300 nm undercut of silicon at each interface during DRIE. These values are then slightly adjusted to 1.086 μm and 312 nm, respectively, to fit with the experimental results.

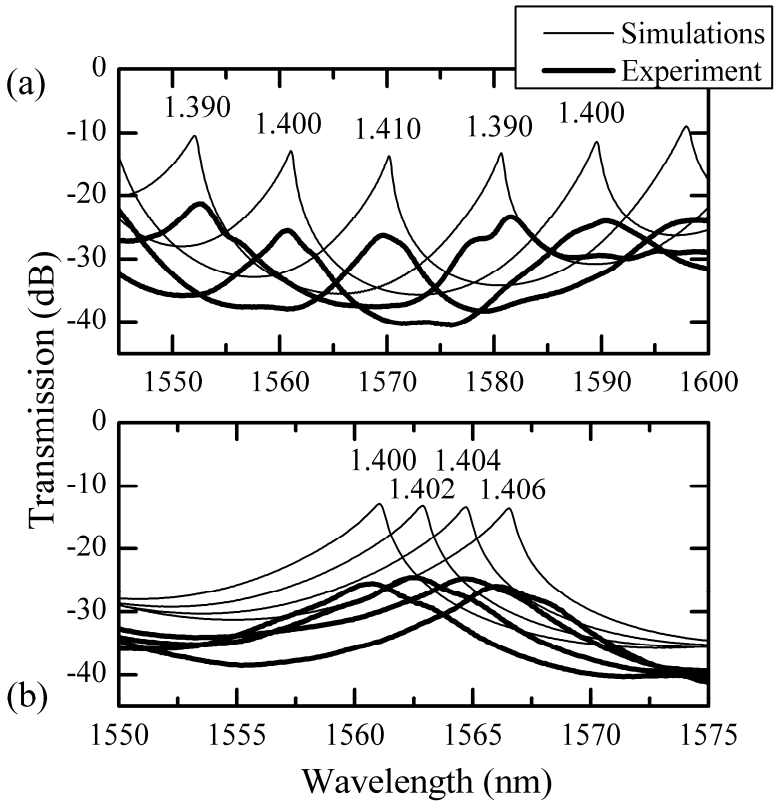

Figure 5.2: Measured (thick lines) and simulated (thin lines) transmission spectrum of the Fabry–Pérot refractometer. Curves are labeled by the RI of the liquid filling the channel. (a) Variation of the RI by Δn=0.010. (b) Variation of the RI by Δn=0.002.

As can be seen in Figure 5.2, the position and the lineshape of the measured transmission peaks for each RI are in good agreement with the optical simulations. There are however additional losses that are not taken into account by the model. The two possible causes for these losses are scattering by surface roughness and imperfect parallelism between the optical planes. Surface roughness was previously measured by atomic force microscope on the sidewalls of large trenches for devices fabricated using a similar fabrication process [81].The measured value, σ=26.2 nm RMS, was mainly a result of the periodic scalloping effect caused by the DRIE process. The spatial period of the scalloping (T=10 nm) is small compared to the wavelength of light (λ) and satisfies the relation $\ln(\lambda/T) < -\ln n_{Si}$, where n_{Si} is the RI of silicon. Consequently, surface roughness at each interface can be modeled by a thin layer of thickness 2σ and of intermediate RI between air and silicon [76]. Including this virtual layer in the transfer matrix

simulations, we found that the effect on the transmission spectrum was negligible. Therefore, with our fabrication process, surface roughness is not a limiting factor for optical multilayer applications. The variations between simulated and experimental results in Figure 5.2 are most likely caused by imperfect parallelism between the optical planes. This imperfection, common to almost any DRIE process, was measured on SEM photographs of cleaved test structures and is smaller than 0.5°.

The simulated and experimental wavelengths at maximal transmission are plotted in Figure 5.3 as a function of RI. As expected from the simulations (Figure 5.2), the curve follows an essentially linear pattern with a sensitivity of 907 nm/RIU. The experimental results match the simulations perfectly, within the uncertainty on the RI of the liquids (±0.0005 RIU around λ=1550 nm).

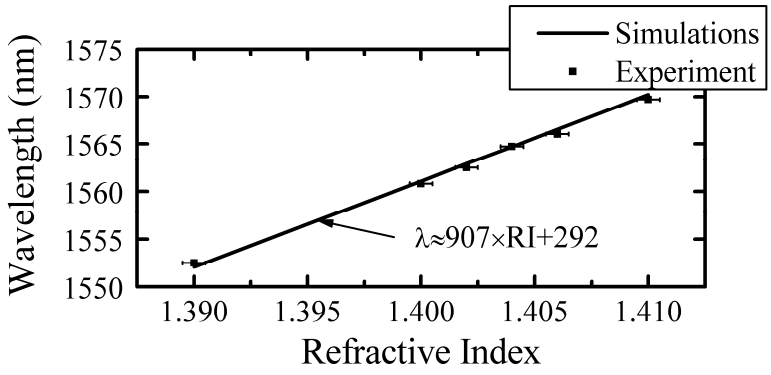

Figure 5.3: Simulated and experimental wavelength at maximal transmission between 1550 and 1570 nm, as a function of RI. The error bars represent the uncertainty on the RI of the liquids (±0.0005 around λ=1550 nm).

As for the majority of RI sensors, the resolution of the RI measurement is limited by the uncertainty on the resonance wavelength measurement. Since our optical cavity has a relatively low quality factor (Q=400 for the n=1.400 resonance spectrum of Fig. 2), it is expected that the main source of uncertainty will be the amplitude noise that is superimposed to the resonance spectrum [82]. To quantify this source of error, we recorded the transmission spectrum of the cavity, filled with the n=1.400 liquid, 20 times at 90 s intervals. To attenuate the effect of the noise, the wavelength at maximal transmission was determined by fitting a fourth order polynomial to the maximal half of the resonance peaks. The obtained values of resonance

wavelength had a standard deviation of σ=0.005 nm, which yields a detection limit of 3σ=0.015 nm. From this and from the sensitivity reported above, the resolution of our sensor is $\Delta n=1.7\times10^{-5}$.

This resolution is the highest reported for a volume RI sensor integrated with a microfluidic system. Compared to resonant optical microcavities performing evanescent wave sensing, the resolution is two order of magnitude higher than the one reached with 2D photonic crystals [89] and two orders of magnitude lower than the state of the art $\Delta n\sim10^{-7}$ resolution reached with optical ring resonators [90].

The sensor is also very robust. During characterization, no particular attention was paid to cleanliness (quick dip in acetone between each measurement, out of clean room environment) and the sensor still works perfectly. A possible explanation for this is that only one of the six interfaces of each Bragg reflector is in contact with the liquid. While this interface gets contaminated, the other five remain perfectly clean and the impact on the optical response is limited. This might be an important advantage compared to other Fabry–Pérot cavities for which the mirrors are made of a single metallic coating [86]. Fabry-Pérot refractometers made of fiber Bragg gratings [85, 87] also have the same advantage but the spatial overlap between the resonant electromagnetic field and the liquid is poor. This lowers the sensitivity and the resolution of the device by two orders or magnitude ($\Delta n=1.8\times10^{-3}$ for Ref. [85]) compared to our sensor.

The most important applications expected for the sensor are single living cells characterization and integration to chip-based liquid chromatography (LC) systems. Single-cell characterization is often performed in microfluidic systems using integrated refractometers [84, 86-88]. This field of research could benefit from the high resolution and the robustness of our sensor but also from the possibility to simultaneously fabricate several devices. Chip-based LC systems are often fabricated using processes similar to the ones used for our sensor (DRIE of high aspect ratio silicon channels and pillars [91]). The integration of our sensor to such separation systems would be simple and could allow the detection of compounds that cannot be detected by absorption or fluorescence measurements (i.e., alcohols, carbohydrates, polymers, fatty acids, etc.).

5.6 Conclusion

We reported a microfluidic Fabry–Pérot refractometer based on vertically etched silicon Bragg reflectors. The resolution (Δn=1.7×10^{-5} RIU) is the highest reported for a volume RI sensor integrated with a microfluidic system. The sensor is also very robust and should be useful for applications such as single living cell characterization and chip based LC.

CHAPTER 6 GAS SENSING USING POLYMER-FUNCTIONALIZED DEFORMABLE FABRY-PEROT INTERFEROMETERS

This chapter is a reproduction of a submitted article[7] relating the use of polymer functionalized deformable Fabry-Perot interferometers as sensors for volatile organic compounds. Sections 6.1-6.6 present the original manuscript text, while section 6.7 presents appendices submitted together with the manuscript as supplemental electronic information (to be published online only). For more details on the fundamental aspects of Fabry-Perot interferometers used as deformation sensors, please refer also to Chapter 3, section 3.1.2.

6.1 Authors and affiliations

Raphael St-Gelais,[a] Gillian Mackey,[b] John Saunders,[b] Jingjing Zhou,[b] Antoine Leblanc-Hotte,[a] Alexandre Poulin,[a] Jack A. Barnes,[b] Hans-Peter Loock,[b] R. Stephen Brown,[b] and Yves-Alain Peter*[a]

[a] *Department of Engineering Physics, Polytechnique Montréal, P.O. Box 6079, Station Centre-Ville, Montréal, QC, H3C 3A7, Canada.*

[b] *Department of Chemistry, Queen's University, Kingston, ON, K7L 3N6, Canada.*

---

[7] R. St-Gelais, G. Mackey, J. Saunders, J. Zhou, A. Leblanc-Hotte, A. Poulin, J. A. Barnes, H.-P. Loock, R. S. Brown, and Y.-A. Peter, "Gas sensing using polymer-functionalized deformable Fabry-Perot interferometers," *Sensor Actuat. B-Chem.,* 2012 (in revision)

6.2 Abstract

We report a chemical vapor sensor in which polymer swelling, upon analyte absorption, is used to deform an on-chip silicon Fabry-Perot interferometer (FPI). The magnitude of the deformation, recorded through the resonance wavelength shift, is proportional to the analyte concentration in accordance with a simplified analytical model and with finite element simulations. Conventional and phenyl-doped polydimethylsiloxane (PDMS) polymers are used to functionalize different interferometers, which are tested for the detection of two volatile organic compounds, i.e. m-xylene and cyclohexane. The detection of m-xylene concentrations down to 34 ppm—limited by our flowmeter setup—is achieved experimentally. Based on the sensitivities and the noise characteristics of the devices, limits of detection (LODs) of 1.6 ppm m-xylene and 6.3 ppm cyclohexane are expected.

Keywords—Gas sensing; Fabry-Perot interferomer; Polymer swelling; Volatile organic compound; Silicon micromachining

6.3 Introduction

Upon analyte absorption, many polymers (e.g., PDMS) are known to expand [92], which phenomenon is usually referred to as "polymer swelling". Such expansion can be used to deform optical interferometers, causing a shift of their resonance condition that can be monitored to create chemical sensors. This approach was previously used with various optical interferometers. Polymer-coated fiber Bragg gratings were shown to deform upon exposition to salt [93] hydrocarbons [94] and humidity [95]. Bragg gratings were also fabricated directly with deformable polymer layers and were found to be sensitive to the presence of acetone [96], salt [97], and volatile organic compounds [98] (VOCs). Fabry-Perot interferometers (FPI) can also be formed simply by exploiting reflections at the two material interfaces of single deformable polymer membranes. This approach was used to detect VOCs [99-101] and ionic strength [102].

The sensors reported here rely on deformable Fabry-Perot interferometers. As presented in Figure 6.1, these FPIs are implemented in-plane with the substrate by vertical plasma etching of silicon-air Bragg reflectors. The in-plane (i.e.: vertical mirrors, in-plane optical axis) rather than out-of-plane [96-102] configuration allows monolithic integration of microfluidic systems and optical fiber alignment grooves. Integrated microfluidic systems simplify the parallel

functionalization of multiple interferometers, using different polymers, to target specific classes of analytes. Fiber grooves allow the remote interrogation of the interferometers with passively aligned conventional single-mode optical fibers, rather than requiring free space alignment of light sources and photodetectors [96-102].

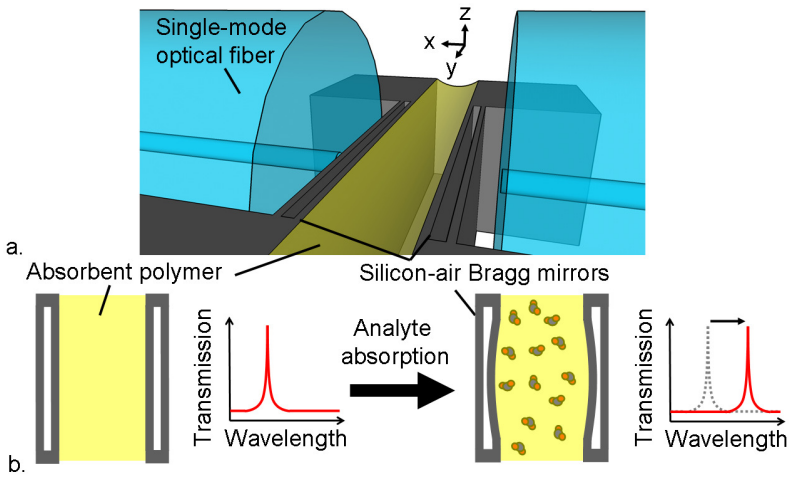

Figure 6.1: (a) Schematic representation of the deformable interferometric sensor. (b) Schematic representation of the sensor operation principle. Upon sample absorption, polymer expansion deforms the interferometer, inducing a shift of its resonance wavelength. Refractive index changes in the polymer, upon absorption, also contribute to this shift.

6.4 Methodology

6.4.1 Sensing mechanism

Upon analyte absorption, three factors can cause shifts of the interferometer ($\Delta\lambda_{Res}$) resonance wavelength. First, as depicted in Figure 6.1 (b), polymer swelling deforms the interferometer and increases (ΔL) mirror separation (L). This mechanism will later be demonstrated to be the dominant one. Secondly, if the refractive index of the analyte (n_a) and the polymer (n_p) are different, the refractive index of the polymer-analyte mixture (n) should change by a factor Δn_{Mix} upon sample absorption. Lastly, if the mirrors oppose a significant force to the polymer expansion, there should be a densification of the polymer, which should lead to a Δn_σ variation of its refractive index. All three effects change the interferometer optical pathlength (nL), and contribute to the measured resonance wavelength shift ($\Delta\lambda_{Res}$) through:

$$\frac{\Delta\lambda_{Res}}{\lambda_{Res}} = \alpha\frac{\Delta L}{L} + \beta\frac{\left(\Delta n_{Mix} + \Delta n_{\sigma}\right)}{n}, \tag{6.1}$$

where $\alpha = 0.75$ and $\beta = 0.93$ are device-specific reduction factors (≤ 1). The factor α accounts for the fact that only one layer in each Bragg mirror is displaced upon analyte absorption (see Figure 6.1 b). The factor β accounts for the fact that the resonant mode inside the cavity is not located entirely inside the polymer, but also partly inside the mirrors (i.e., the thickness of the mirrors is not negligible compared to L, the distance between the mirrors). The value of both parameters can be calculated using a previously reported optical simulation algorithm for deep-etched Fabry-Perot interferometers [103], as detailed in appendix 6.7.1.

We define the dimensionless sensitivity (Γ_{ϕ}) as the normalized ratio of the resonance wavelength shift ($\Delta\lambda_{Res}$) to the absorbed volume fraction of analyte (ϕ_a) inside the polymer:

$$\Gamma_{\phi} = \frac{1}{\lambda_{Res}}\frac{\Delta\lambda_{Res}}{\Delta\phi_a}. \tag{6.2}$$

Conveniently, ϕ_a can be related to the volume/volume (v/v) concentration of analyte in air (C_{air}), near the polymer, using the ideal gas law and the partition coefficient of the polymer for the respective analyte ($K_{p\text{-}a}$):

$$\phi_a = K_{p-a}\frac{PV_m}{RT}C_{air}, \tag{6.3}$$

where P is the pressure (1 atm in our case), T is the temperature, R is the gas constant, and V_m is the molar volume of the analyte, in liquid phase.

For all the calculations presented in this work we assume that upon absorption, the final volume of the polymer-analyte mixture equals the initial volume of the polymer, plus the absorbed volume of analyte. In other words we assume that there is no volume reduction upon absorption, except in the presence of mechanical stresses inside the polymer (calculations in section 6.4.1.1 will demonstrate these stresses lead to negligible volume reductions). In this context, the relative volume (V) expansion of the polymer upon absorption of a ϕ_a volume fraction of analyte is given by:

$$\frac{\Delta V}{V} = \Delta\phi_a \,. \tag{6.4}$$

This assumption of volume additivity is supported by reports that the absorption of a slightly lower refractive index analyte (cyclohexane) reduced the refractive index of a PDMS-based polymer [104]. This would not have been possible if significant volume reduction occurred upon absorption, since volume reduction would have led to an increase of the refractive index.

6.4.1.1 Simplified analytical model

This section details the sensitivity (Γ_ϕ) of deformable FPI sensors in the case where:

1. the mirrors are perfectly movable, such that they oppose negligible forces to the expansion of the polymer,
2. the volume increase of the polymer (i.e. swelling) is directed mainly in one direction, parallel to the optical pathlength between the mirrors (L), such that ΔL is maximized.

Interestingly, these conditions straightforwardly apply to out-of-plane deformable Fabry-Perot interferometers [99-102]. In these cases, the polymer is bonded to a rigid substrate such that swelling can only occur in the out-of-plane direction, which is parallel to the optical axis (criterion 2). There is also no force opposing the movement of the top material interface that is used as the movable mirror of the interferometer (criterion 1).

For the in-plane devices presented in the current work (Figure 6.1), compliance with the two abovementioned criteria is less trivial. The deformable layer in each Bragg mirror might oppose non-negligible force to the expansion of the polymer. The polymer might also swell upward (positive z direction in Figure 6.1 a) if the bonding strength with silicon is not strong enough. We will therefore use the simplified ideal formalism presented in this section primarily as a basis for comparison of our in-plane sensor with out-of-plane sensing mechanisms. In the next section (6.4.1.2) finite element simulations will address the limitations of the analytical model for in-plane devices.

Under the two conditions listed above, it is possible to show that the relative length increase between the mirrors, upon absorption of a ϕ_a volume fraction of analyte, is given by:

$$\left.\frac{\Delta L}{L}\right|_{Simplified} = \frac{\Delta\phi_a}{3}\frac{1+\nu}{1-\nu}, \tag{6.5}$$

where ν is the polymer Poisson's ratio. It is also possible to show that the compressive stress experienced by the polymer due to its restrained expansion in the directions perpendicular to the optical axis (*y* and *z* in Figure 6.1) is given by:

$$\sigma_{\perp} = \frac{\phi_a E}{3(1-\nu)}, \tag{6.6}$$

where *E* is the Young's modulus of the polymer. This stess will in turn lead to a volume reduction of the polymer given by:

$$\frac{\Delta V_h}{V} = \frac{\Delta\sigma_h}{B} = \frac{2}{9}\frac{\Delta\phi_a E}{B(1-\nu)}, \tag{6.7}$$

where *B* is the bulk modulus of the polymer, and $\sigma_h = 2/3\,\sigma_{\perp}$ is the hydrostatic stress inside the polymer.

Also, the addition of a ϕ_a analyte volume fraction will lead to a Δn variation of the polymer refractive index. Several rules exist to predict the refractive index of binary mixtures [105, 106]. The Lorentz-Lorenz relation is probably most frequently used. We however choose to use the simpler Gladstone-Dale relation, which yields very similar results for the typical refractive indices that we will encounter. This relation (Eq. (6.8)) is linear relative to ϕ_a, leading to a simplified expression of the sensitivity (Γ_ϕ).

$$\frac{\Delta n_{Mix} + \Delta n_{\sigma}}{n} = \Delta\phi_a \frac{\left(n_a - n_p\right)}{n_p} + \frac{\Delta V_h}{V}\frac{\left(n_p - 1\right)}{n_p} \tag{6.8}$$

Finally, combining Eqs. (6.1), (6.5)-(6.8) in Eq. (6.2) yields the sensitivity of deformable Fabry-Perot chemical sensors in the context of the simplified analytical model:

$$\left.\Gamma_{\phi}\right|_{Simplified} = \frac{\alpha}{3}\frac{1+\nu}{1-\nu} + \beta\frac{\left(n_a - n_p\right)}{n_p} + \beta\frac{2}{9}\frac{\left(n_p - 1\right)}{n_p}\frac{E/B}{1-\nu}. \tag{6.9}$$

In Eq. (6.9), the first term accounts for interferometer deformations. The second term accounts for polymer refractive index variations due to mixture with an analyte of different refractive index. The third term accounts for refractive index variations due to hydrostatic stress upon expansion.

The absorbent polymers used in the following experiments are essentially incompressible. For example, the bulk modulus [107] ($B = 10^3$ MPa) of Sylgard 184 PDMS is significantly higher than its Young's modulus [108] (E = 1.8 MPa), which yield a $\nu = 0.5 - E/2B = 0.499$ Poisson's ratio. In this context, the third term of Eq. (6.9) is almost 3 orders of magnitude smaller than the first two terms and can be neglected. Eq. (6.9) can therefore be rewritten as:

$$\Gamma_{\phi}\Big|_{Simplified} \approx \alpha + \beta \frac{\left(n_a - n_p\right)}{n_p}. \tag{6.10}$$

Furthermore, for most organic compounds, the refractive index difference in Eq. (6.10) (n_a - n_p) should be in the order of 0 - 0.15. In these cases, the term that accounts for interferometer deformations (α) should always be at least 10 times larger than the term that accounts for refractive index variations. Therefore, with $\alpha = 0.75$, the absorption of, for example, a ϕ_a = 1% volume fraction of analyte is expected to induce a $\Delta\lambda_{res}/\lambda_{res} \approx 0.75\%$ shift of the interferometer resonance wavelength.

6.4.1.2 Finite element simulations

In order to evaluate if the response of the fabricated devices can be expected to be close to the simplified analytical case, finite element simulations are performed using CoventorWare 2010. An isotropic expansion of the polymer volume filling the gap between the two mirrors (see Figure 6.1) is simulated. Upon expansion, the relative increase of the distance between the mirrors ($\Delta L/L$) and the hydrostatic pressure inside the polymer (σ_h) are evaluated. For these simulations, we use the Young's modulus (E = 1.8 MPa) [108] and Poisson's ratio ($\nu = 0.499$) values of Sylgard 184 PDMS.

The meshed model used for the simulations is presented in Figure 6.2 (a). For each of the two Bragg mirrors, only the one silicon layer that is in contact with the polymer is included in the model. The (y, z) dimensions of these layers are (130 μm, 80 μm). Their thickness (in the x

direction) is 600 nm, as determined by previous optical characterization of the interferometers [103]. The layers are attached at both *y* extremities to the edges of the microfluidic channel, which are considered to be immobile. The bottom *z* extremities of the mirror layers are fixed to the substrate (*Fix All* boundaries in Figure 6.2 a) while their upper *z* extremities are free to move.

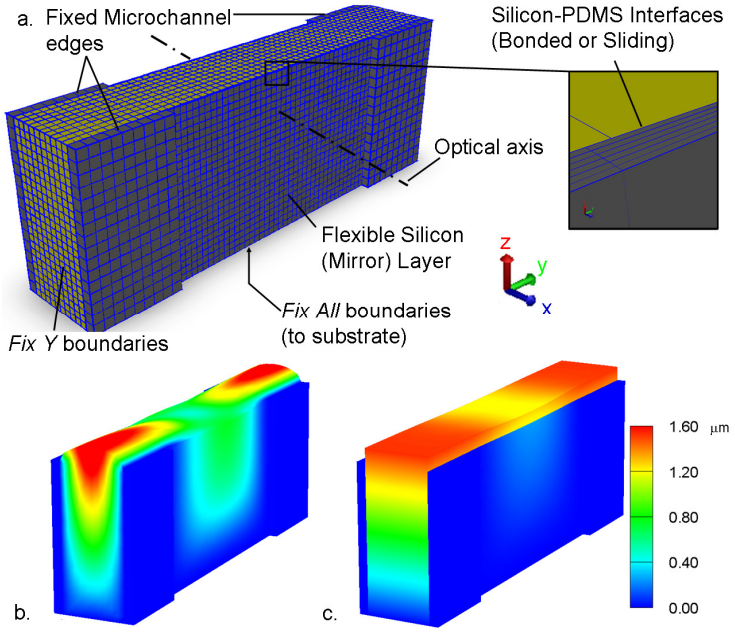

Figure 6.2: (a) Mesh model and boundary conditions for the simulations of the interferometer deformation upon polymer swelling. (b, c) Magnitude of the deformation upon a 2% polymer volume increase. The deformations (but not the color scales) are exaggerated by a factor 5. The simulations are performed for bonded (b) and sliding (c) silicon-PDMS material interfaces.

Two different types of boundary conditions are used to simulate the contact interfaces between silicon and PDMS. The first type considers the two materials to be tightly bonded together, such that no sliding can occur. The second type considers the two materials to be in contact but to be free to slide on each other without friction. We expect the experimental results to lie somewhere between these two extreme cases, which we will refer to as the "bonded" and "sliding" models.

Only a small portion of the microfluidic channel length (40 µm) is included in the mesh model on each side of the Fabry-Perot cavity. The continuation of the truncated channel must

therefore be simulated using appropriate boundary conditions. It is possible to show that, away from the deformable mirror layers, no polymer movement occurs in the directions (*x*, *y*) parallel to the substrate due to the rigid boundaries of the microfluidic system. The continuation of the channels is therefore simulated using "*Fix Y*" boundary conditions (see Figure 6.2 a).

For the two models, the response to various polymer volume increases is simulated. A linear relation is established between the absorbed volume fraction of analyte (ϕ_a) and the relative pathlength increase between the mirrors (on the optical axis of the system):

$$\begin{aligned} \left.\frac{\Delta L}{L}\right|_{Bonded} &= 1.77\Delta\phi_a, \\ \left.\frac{\Delta L}{L}\right|_{Sliding} &= 0.51\Delta\phi_a. \end{aligned} \tag{6.11}$$

A linear relation is also established between ϕ_a and the hydrostatic stress (σ_h) inside the polymer volume where light will interact with the system (around the optical axis in Figure 6.2a). As for the simplified analytical model, the hydrostatic stress (σ_h) is found to be negligible compared with the bulk modulus of PDMS based polymers. Its contribution to the sensitivity of the sensors can therefore still be neglected, as in section 6.4.1.1.

Finally, replacing Eq. (6.5) by Eq. (6.10) in the formalism of section 6.4.1.1 yields the sensitivity of the sensors (Γ_ϕ) for both the bonded and the sliding models:

$$\begin{aligned} \Gamma_\phi\Big|_{Bonded} &= 1.77\alpha + \beta\frac{\left(n_a - n_p\right)}{n_p}, \\ \Gamma_\phi\Big|_{Sliding} &= 0.51\alpha + \beta\frac{\left(n_a - n_p\right)}{n_p}. \end{aligned} \tag{6.12}$$

In Eq. (6.12) the sliding model yields a deformation sensitivity (0.51α) that is twice smaller that what was predicted (1.00α) by the simplified analytical model. This result was expected since the polymer is now free to expand in two directions (*x*, *z*) rather than only one for the analytical model (similarly, a polymer that would be free to expand in all three dimensions would yield a 0.33α sensitivity).

Surprisingly, the bonded model yields a higher deformation sensitivity (1.77α) than what is predicted by the simplified analytical model in Eq. (6.9): 1.00α. This is because, in Figure 6.2 (b), the polymer is not free to expand in the microchannel, on each side of the optical cavity. Consequently, the polymer located in these regions expands towards the optical axis of the system, where the deformation is amplified (See appendix 6.7.2). However, this behavior is found to depend strongly on the polymer Poisson's ratio. For $\nu < 0.499$, the predicted sensitivity of the bonded model quickly reduces and essentially matches the sensitivity of the analytical model when $\nu < 0.45$ (See appendix 6.7.2).

6.4.2 Experimental methodology

A scanning electron microscope (SEM) photograph of a Fabry-Perot interferometer is presented in Figure 6.3 (b). This device has 3 silicon layers per mirror, compared to only two in the schematic view of Figure 6.1. Both configurations were fabricated and tested for gas detection and, as predicted in appendix 6.7.1, were found to respond similarly to deformations and refractive index changes. The interferometers are etched in silicon wafers using an inductively coupled plasma reactor (ICP180-100, Oxford Instruments Inc.). A two-mask soft lithography process is used to fabricate successively the smaller (multilayer mirrors) and the larger (optical fiber alignment grooves, microfluidic system) features [103].

The absorbent polymer (Figure 6.3 (c)) is inserted between the two mirrors of the interferometer using a monolithically integrated microfluidic system. A drop of liquid (~15-20 μL) pre-polymer mixture is placed in the leftmost reservoir of Figure 6.3 (a). The polymer flows by capillary forces in the microfluidic channel to fill the gap in the interferometer (Figure 6.3 (c)), and is then left to cure at room temperature for several hours. We did not determine the minimum required polymer curing time. Some devices required more than 12 hours of curing for stable performance, so all devices were cured for more than a week.

Two different polymers were tested for the functionalization of the interferometers. Some devices were coated with commercial PDMS (Dow Corning® Sylgard 184), while the others were functionalized with a PDMS-polydiphenylsiloxane copolymer (PDMS-PDPS). The copolymer was prepared by a procedure similar to the one previously reported [104], but using different

mixture proportions (10% polydiphenylsiloxane (PDPS) mole fraction, 3% titanium tetraisopropoxide cross-linker mole fraction).

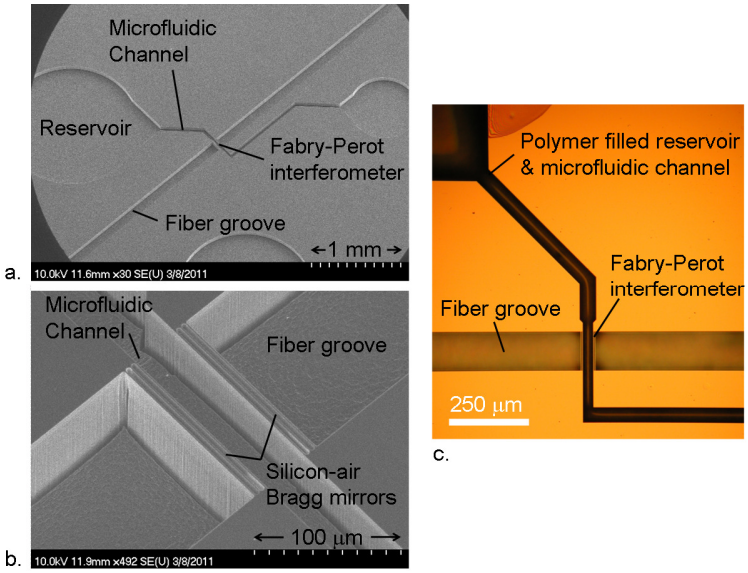

Figure 6.3: (a) Low magnification scanning electron micrograph of a sensor, prior to polymer coating, showing the monolithically integrated microfluidic system used for functionalization. (b) Higher magnification view of the Fabry-Perot interferometer and the optical fiber alignment grooves. (c) Optical micrograph of a polymer-coated device.

The functionalized devices were tested for the detection of two different vapor phase analytes at room temperature and atmospheric pressure. To produce different analyte concentrations, saturated vapor was first generated by bubbling nitrogen through a wash bottle containing the analyte in liquid phase. A two channels mixing flowmeter was then used to dilute back the saturated vapor with pure nitrogen, in order to lower analyte concentration. The flowmeter and gas bubbling assembly are shown in Figure 6.4 (a). A gas cap (Figure 6.4 (b)) was lowered over the sensor to allow analyte vapor to disperse evenly over the chip. The complete setup was housed inside a laminar flow hood. Cyclohexane and m-xylene were chosen as the analytes to allow comparison with previous work using similar polymers.[104, 109]

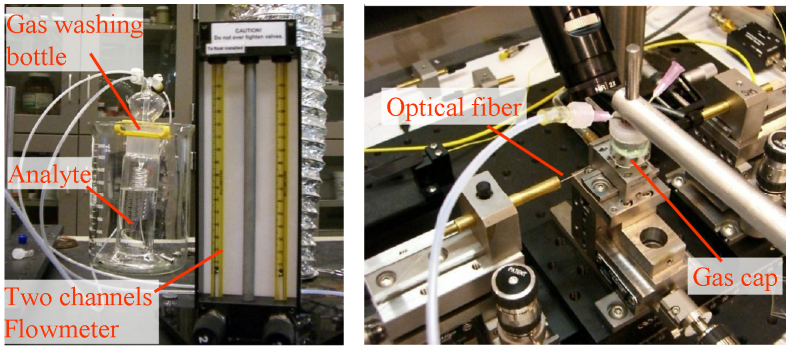

a. b.

Figure 6.4: (a) Experimental setup used for vapor phase analyte generation and concentration adjustments. (b) Experimental setup used to evenly deliver diluted analyte over the sensor chip (which will eventually be positioned under the gas cap but is not shown here).

Upon gas exposure, the interferometer resonance wavelength was tracked in real time by continuously scanning a tunable external-cavity diode laser source (Ando AQ4320D). The laser was interfaced with the interferometer through conventional single-mode optical fibers (Corning® SMF-28), which were cleaved and inserted in the optical fiber alignment grooves (Figure 6.3). The transmission spectrum was recorded at 30 second intervals using an InGaAs photodiode detector (Thorlabs D400FC) and a lock-in amplifier (Stanford Research Systems SRS844 RFCA). The voltage output of the lock-in amplifier was then collected using a 16-bit data acquisition USB device (Measurements Computing PMD 1608 FS) and custom-made LabView (National Instruments) software. Amplitude noise was minimized numerically in each recorded spectrum using a zero-phase shift, forward and reverse digital convolution filter (Matlab® "FILTFILT" function). A 1 nm wide Gaussian distribution ($\sigma = 0.2$ nm) was used as the filter. The exact resonance wavelength position was then determined for each spectrum by fitting a 4^{th} order polynomial to the top half of the filtered resonance peaks.

6.5 Results and discussion

The response of a PDMS-coated interferometer to various m-xylene and cyclohexane vapor concentrations is presented in Figure 6.5. As expected, in Figure 6.5 (a) the resonance peak position is found to increase upon exposition to m-xylene, before returning to its initial value when the gas flow is switched back to pure nitrogen. In Figure 6.5 (b, c), this shift of the

resonance wavelength is reported, as a function of time, for various concentrations of m-xylene and cyclohexane. The response to 34 ppm m-xylene, the lowest concentration reachable with our flowmeter, is clearly visible. A limit of detection below this value is therefore expected.

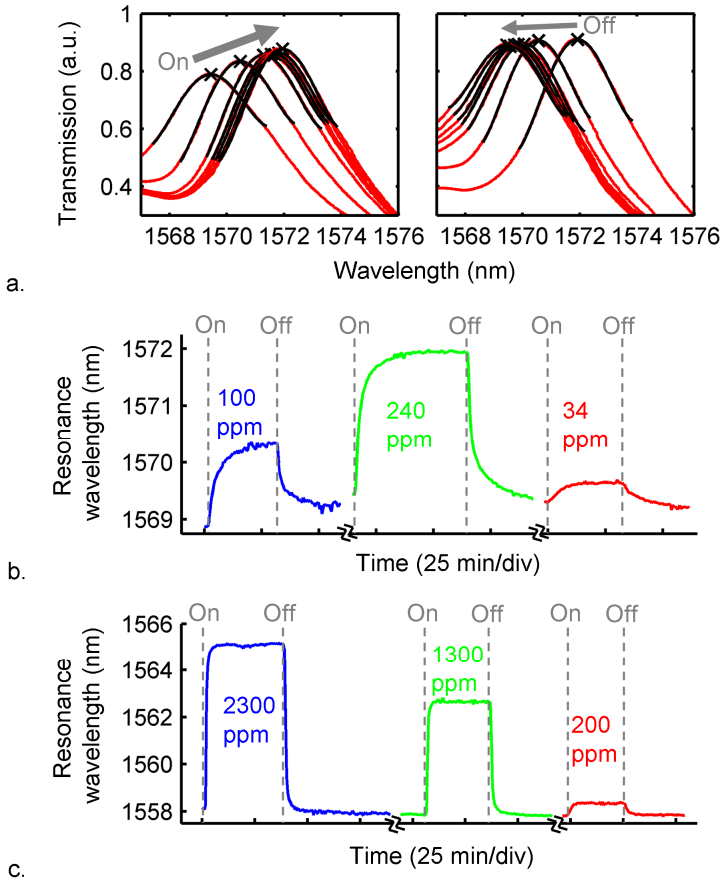

Figure 6.5: (a) Measured transmission spectra of a PDMS-coated deformable FPI sensor upon exposition to a 240 ppm m-xylene vapor concentration. The peak resonance wavelength ("X" marked) is measured by fitting a 4th order polynomial on top of the resonance peaks. Its position increases when gas flow is turned on (left) and then returns to its initial position (right) when the flow is switched back to pure nitrogen. (b, c) Resonance wavelength (λ_{Res}) of a PDMS-coated interferometer over time. The "On" and "Off" markers designate the beginning and the end of exposure to the indicated concentrations of m-xylene. (b) and cyclohexane (c).

The resonance wavelength increase ($\Delta\lambda_{Res}(t)$) follows an essentially exponential pattern (i.e.: $\Delta\lambda_{Res}(t) \propto 1\text{-}e^{-t/\tau}$) with a time constant ($\tau$) that differs for each polymer-analyte combination. In PDMS, the response time is found to be almost 4 times faster for cyclohexane ($\tau = 40$ sec) than for m-xylene ($\tau = 150$ sec). This faster response time however occurs at the expense of an approximately 4 time lower sensitivity to cyclohexane than to m-xylene.

This trade-off between sensitivity and response time is directly related to the partition coefficient ($K_{p\text{-}a}$) of each polymer-analyte combination. Higher $K_{p\text{-}a}$ values yield higher absorbed volume fractions (ϕ_a) and therefore higher sensitivities. However, higher $K_{p\text{-}a}$ also yield higher retention times [110] (i.e. lower diffusion constants), which increase the time required for the analyte to diffuse completely inside the 80 μm deep polymer-filled channel.

In Figure 6.6, the resonance wavelength shift ($\Delta\lambda_{Res}$) for the different m-xylene vapor exposures is compared with the analytical model (Eq. (6.9)), and with the finite element (Eq. (6.12)) bonded and sliding models. The expected response due only to refractive index variations is also included to highlight the influence of mechanical deformations on the sensitivity (a control experiment using undeformable mirrors was also carried to confirm the influence of refractive index variations only. See appendix 6.7.3). The absorbed volume fraction of analyte (ϕ_a) is converted (Eq. (6.3)) to v/v gas concentrations (C_{air}) in Eq. (6.9) and (6.12), using a $K_{p\text{-}a} = 2090$ partition coefficient for m-xylene between PDMS and air [110]. We also use $V_m = 0.123$ L/mol, and the reported [104] refractive indices of PDMS ($n_p = 1.3959$) and xylenes ($n_a = 1.4802$) at $\lambda = 1550$ nm.

As expected, the experimental results fall between the bonded and sliding models. The silicon-PDMS adhesion force appears to be important enough to yield a higher experimental sensitivity than the sliding model prediction. The sensitivity is, however, lower than the bonded model prediction. This could be an indication that PDMS does not bond perfectly with silicon, but is somewhat free to spatially reorganize itself upon expansion. Growing a thin layer of thermal silicon dioxide, prior to polymer coating, could be a way to increase the polymer-interferometer bonding strength and improve sensitivity. It is also possible that the bonding strength is already high enough, but that finite element bonded sensitivity was overestimated. As discussed in section 6.4.1.2 (see also appendix 6.7.2), small variations of the PDMS Poisson's

ratio tend to strongly affect the bonded model sensitivity, which rapidly reaches that of the simplified analytical model.

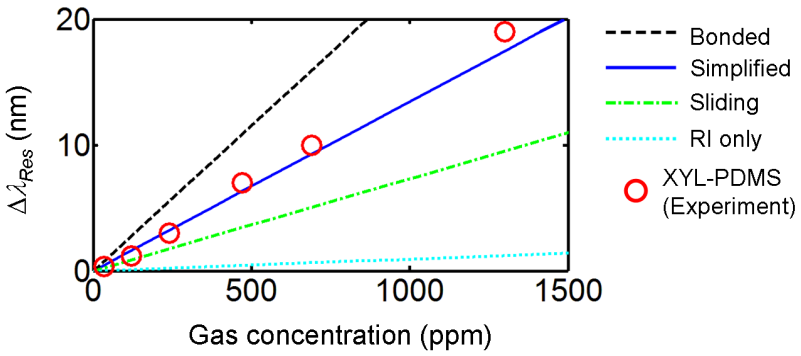

Figure 6.6: Experimental and simulated (bonded, sliding and simplified analytical models) resonance wavelength shift ($\Delta\lambda_{Res}$) as a function of m-xylene concentration. "RI only" designates the expected response due to refractive index variations only (i.e., neglecting mechanical deformations).

The simplified analytical model (section 6.4.1.1) is found to reproduce our experimental results remarkably well. A relatively good correspondence was expected since, as shown also in Eq. (6.9), (6.12), the simplified analytical model yields an intermediate sensitivity between the two extreme possible cases (i.e., the bonded and sliding finite element models). Therefore, for other polymers having different mechanical properties, this model could most likely provide a useful estimate of the sensitivity without repeating the time consuming finite element simulations. A perfect match with the experimental results, such as in Figure 6.6, is however likely to be coincidence and should not be expected in all cases.

As discussed in section 6.4.1.1, the simplified analytical model also describes the behavior of out-of-plane deformable FPI sensors [99-102]. Its correspondence with the current experimental results therefore indicates that the in-plane implementation of deformable FPI did not cause any significant sensitivity reduction compared to out-of-plane designs.

In Figure 6.7, the experimental response is reported for m-xylene-PDMS (XYL-PDMS) and also for the three other polymer-analyte combinations. The highest sensitivity (0.023 nm/ppm) is obtained for m-xylene-PDMS-PDPS. This may be due to the addition of phenyl groups within the polymer, which could increase the polymer affinity for aromatic compounds,

such as m-xylene. There are, however, other differences between the two polymers, including chain length and the type and degree of cross-linking, so other mechanical and chemical factors may also contribute to the sensitivity difference. The lowest sensitivity (0.0030 nm/ppm) is obtained for cyclohexane (CY) in PDMS, which may indicate that the partition coefficient ($K_{p\text{-}a}$) is significantly lower for cyclohexane than for m-xylene. We did not find measurements of $K_{p\text{-}a}$ for CY-PDMS in the literature, but taking the linear temperature-programmed retention index of cyclohexane [111] (LTPRI = 650) and the relations reported in ref. [110], we expect $K_{p\text{-}a} \cong 320\text{-}350$. Using these values, the CY-PDMS experimental results are within the bonded and sliding models predictions.

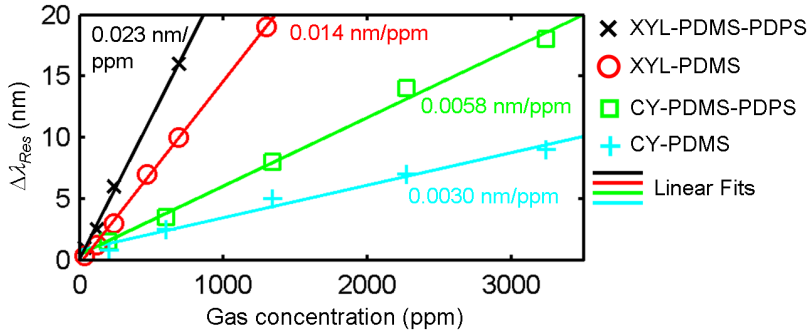

Figure 6.7: Experimental response obtained for the four analyte-polymer combinations of m-xylene (XYL), cyclohexane (CY), PDMS, and the phenyl-doped copolymer (PDMS-PDPS). The linear fits are labelled by their corresponding sensitivities.

The CY-PDMS-PDPS sensitivity (0.0058 nm/ppm) is almost two times higher than the CY-PDMS response. This was not expected initially since cyclohexane is a non-polar analyte, and since the addition of phenyl groups to PDMS tends to increase its polarity [112]. It is possible that the phenyl groups also increase the Hildebrand solubility parameter of PDMS (initially $\delta = 7.3$ cal$^{1/2}$ cm$^{-3/2}$) to a value closer to that of cyclohexane ($\delta = 8.2$ cal$^{1/2}$ cm$^{-3/2}$) [92]. This phenomenon was previously reported [112, 113] and could explain a higher $K_{p\text{-}a}$ for CY-PDMS-PDPS than for CY-PDMS. However, as noted above, there are other differences between the films that may also contribute to the observed $K_{p\text{-}a}$ difference, including chain length and degree of cross-linking. Moreover, those differences may also affect the polymer mechanical properties, which could influence the sensitivity.

In Figure 6.7, PDMS-PDPS showed a 64% increase in sensitivity to m-xylene and a 93% increase in sensitivity to cyclohexane as compared to PDMS. Having distinct sensitivity differences for each analyte could be useful for the development of artificial olfaction systems. Distinct sensitivity differences were exploited previously for artificial olfaction with other micromechanical sensors, such as cantilevered sensors [114], quartz crystal microbalances (QCM) and surface acoustic wave (SAW) sensors [115, 116].

For micromechanical sensors, the sensor limit of detection (LOD) is usually defined as the analyte concentration that produces a response corresponding to 3 times the standard deviation (*std*) of the background noise signal [114, 117]. We calculated a *std* = 0.012 nm amplitude noise from the traces of Figure 6.5 (b, c), and also from the trace of a PDMS-PDPS coated device. Using the sensitivities of Figure 6.7, we therefore expect LODs of 1.6 ppm m-xylene and 6.3 ppm cyclohexane. For comparison, previously reported LODs of QCM [117] and SAW [118] devices to xylenes vapors are on the same order of magnitude, at respectively 1.2 ppm and 3.5 ppm. The reported devices could therefore potentially compete with these technologies, which already find applications in artificial olfaction systems [115, 116].

The reported LOD is however more than one order of magnitude larger than what was reported using out-of-plane FPIs [101]. However, as discussed above, the resonance wavelength sensitivity of the reported devices, and of out-of-plane FPIs, are similar (see discussion related to Figure 6.6). The significantly better LOD of out-of-plane devices is indeed not achieved through higher device sensitivities, but through optimization of a free-space optical interrogation setup [101] (as opposed, in our case, to passively aligned optical fibers). The reported in-plane devices, although less precise in term of LOD, could therefore still be advantageous in situations that would prevent on-site free-space alignment (e.g. field deployment for industrial artificial olfaction).

6.6 Conclusion

We reported a chemical sensor based on in-plane silicon Fabry-Perot interferometers functionalized with PDMS-based polymers. Upon analyte absorption, polymer swelling and refractive index variations were shown to induce strong shifts of the interferometer resonance wavelengths. Mechanical deformations were demonstrated to be the dominant sensing

mechanism, in accordance with analytical and finite element models. The proposed analytical model is also expected to describe accurately the behavior of out-of-plane FPIs [99-102], and could therefore be useful for sensors relying on such optical configuration.

Fabry-Perot interferometers were functionalized with two different polymers (PDMS and PDMS-PDPS) and were used to detect and quantify two volatile organic compounds (m-xylene and cyclohexane). PDMS-PDPS devices were found to be 64% more sensitive to m-xylene and 93% more sensitive to cyclohexane than PDMS devices. Such distinct sensitivity differences, between sensor coatings, are promising for the development of artificial olfaction systems. Moreover, the expected limits of detection of the current proof-of-concept devices (1.6 ppm m-xylene, 6.3 ppm cyclohexane) are already on the same order of magnitude as achieved with micromechanical sensing technologies used for artificial olfaction.

Compared with other types of micromechanical sensors, a possible advantage of deformable in-plane FPI sensors is their potential for field deployment and remote interrogation. The proposed sensor does not need any local source of energy to operate. Sensor heads could be deployed in industrial workplaces or for environmental monitoring, and would be linked to an interrogation system only through passively aligned single mode optical fibers. Using a 1×N optical switch would also allow the readout of multiple sensors (for various locations and/or for various polymers) using a single tunable laser and photodetector.

Compared with previously reported out-of-plane FPIs [99-102], the main distinctive feature of the proposed in-plane sensors is integrability. The in-plane configuration allowed monolithic integration of microfluidic systems, which simplified parallel functionalization of multiple interferometers with different polymers. Integrated fiber alignment grooves also allowed passive alignment of optical fibers, facilitating remote interrogation by avoiding the need for on-site free-space alignment. Finally, successful interfacing of swellable polymers with a silicon optical microsystem is, by itself, an interesting achievement. Such hybrid integration could allow great flexibility in the design of other interferometric, micromechanical, or even electromechanical systems that could be used to maximize sensitivity to polymer swelling.

6.7 Appendices

6.7.1 Optical properties of deformable silicon-air Fabry-Perot interferometers

As depicted in Figure 6.1, only one silicon layer in each Bragg mirror is expected to move upon polymer swelling. Therefore, as the polymer expands, the distance L between the two mirrors increases, but the mirrors themselves are also deformed, which affects their optical properties. We can predict the consequences of this using our previously reported model [103] for deep-etched multilayer optical resonators. This model was demonstrated to correspond closely with the transmission spectra of the interferometers that are used for gas detection in this work.

Figure 6.8 presents simulated transmission spectra of a Fabry-Perot cavity that has the same dimensions as in this work and in ref. [103]. This cavity has two silicon layers per mirror, as in Figure 6.1. The gap between the mirrors (i.e. the polymer) is considered to have a fixed (n = 1.4) refractive index. Each transmission spectrum corresponds to a different relative increase of the distance between the mirrors ($\Delta L/L$). As expected, increasing L shifts the resonance peaks towards longer wavelengths. At the same time, as the mirrors are compressed, their reflection band moves towards shorter wavelengths. The two effects counteract each other and as a consequence the dynamic range of the sensor has an upper limit when the cavity resonance peaks no longer fall within the reflection band of the mirrors. For example, the resonance peak that is initially centered at $\lambda = 1500$ nm is lost when $\Delta L/L$ reaches 2%. For this deformation, the resonance would be located around λ=1520 nm, but the reflection band of the mirrors (the wavelength range where resonance can occur) is now located below 1500 nm.

Within the dynamic range, the response of the resonance wavelength position is essentially linear, and can be described by Eq. (6.1) using a reduction factor $\alpha = 0.75$. This value was calculated from the simulations of Figure 6.8, which were performed for cavities having only two silicon layers per mirror. It is possible to show that the range of $\Delta L/L$ and the α factor are essentially the same for cavities having three silicon layers per mirror (as in Figure 6.4). The only differences between the two configurations are slightly narrower resonance peaks for three-layer devices, and lower signal loss for two-layer devices [103].

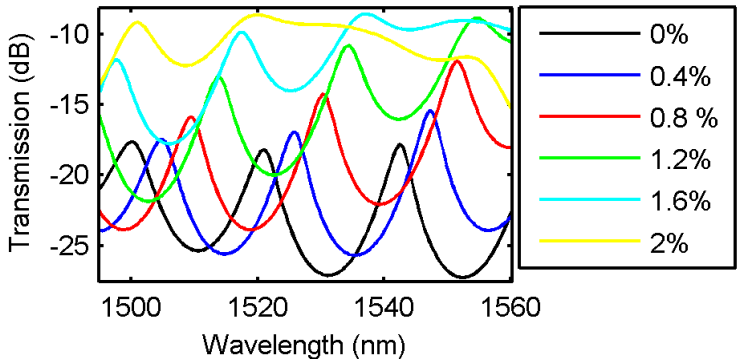

Figure 6.8: Simulated transmission spectra of a Fabry-Perot cavity, similar to the one presented in Figure 6.1. Each spectrum is calculated for a different relative increase ($\Delta L/L$), of the distance between the mirrors (L). As the deformation increases, the resonance peaks shift linearly towards longer wavelengths, as described by Eq. (6.1) with α=0.75. When $\Delta L/L$ reaches 2%, the deformation of the mirrors is too important and the resonance is lost.

We can use the same optical simulation algorithm [103] to define the β reduction factor (Eq. (6.1)). A 907 nm/RIU (refractive index units) sensitivity to changes in refractive index was previously reported using similar Fabry-Perot cavities [A1.1]. Since the current devices were slightly optimized (longer distance between the mirrors, thinner mirrors), we now expect a 1010 nm/RIU sensitivity. This corresponds to a factor β = 0.93 in Eq. (6.1), which is essentially the same for cavities having two or three silicon layers per mirror.

Finally, as shown in Figure 6.2, the expansion of the polymer tends to affect the parallelism between the mirror layers. However, for length increases ($\Delta L/L$) smaller than 2%, the verticality deviation of each deformed layer is expected to be less than 0.25°. This deviation is on the same order of magnitude than what is achievable using our fabrication process [103]. Its consequence on the optical properties of the interferometer should therefore not be significant. Similarly, curvature of the movable Bragg mirror layer (see schematic representation in Figure 6.1 (b)) should yield even smaller layer thickness variations that will also have negligible consequences.

6.7.2 Influence of the Poisson's ratio on the finite element simulation (bonded model)

As discussed in section 6.4.1.2, for an essentially incompressible polymer such as PDMS ($\nu = 0.499$), the predicted mechanical sensitivity (1.77α) of the finite element bonded model is significantly higher than what is predicted using the simplified analytical model (1.00α). This behavior is relatively surprising since the analytical model is based on two assumptions (see section 2.1.1) that represent the ideal case of a deformable FPI (negligible force opposed by the mirrors, polymer volume expansion exclusively parallel with the optical axis). The cause of this higher sensitivity is illustrated in Figure 6.9. The polymer that is confined in the microchannel (on each side of the deformable interferometer) tend to expand in the *y* direction toward the center of the deformable layer, where the optical axis is located. This induces an amplification of the displacement in the *x* direction (parallel with the optical axis) that leads to an increase of the sensitivity.

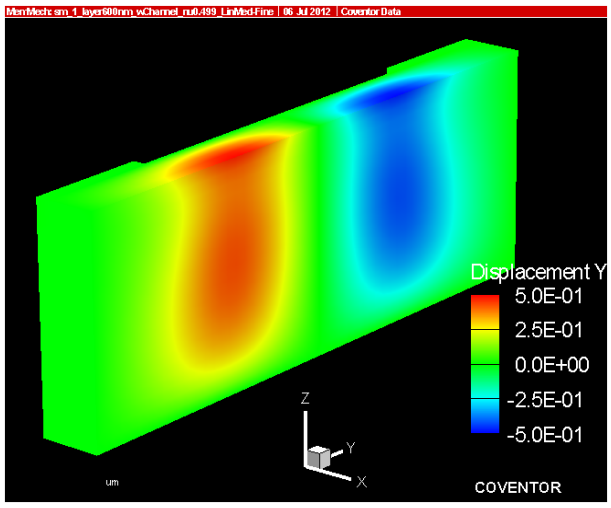

Figure 6.9: X-Sliced view of the finite element bonded model deformation (in the y direction only) upon a 2% polymer volume increase. This important polymer y displacement amplifies the cavity deformation (in the x direction) near the optical axis of the system.

This amplified deformation phenomenon is very sensitive to the Poisson's ratio of the polymer, as illustrated in Figure 6.10. When the Poisson's ratio decreases, the bonded model sensitivity quickly reduces to essentially match the simplified analytical model for $\nu < 0.45$.

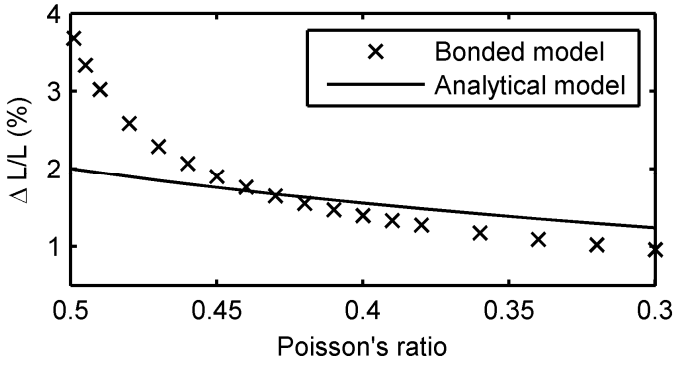

Figure 6.10: Relative cavity length increase as a function of the polymer Poisson's ratio, upon absorption of a ϕ_a = 2% volume fraction of analyte. The bonded model prediction essentially matched the simplified analytical model when $\nu < 0.45$.

6.7.3 Control experiment using undeformable interferometers

In order to confirm that the sensitivity of the reported interferometers is due mainly to mechanical deformations, experiments were carried with Fabry-Perot interferometers having rigid, undeformable mirrors (Figure 6.11). In this case, the resonance wavelength shift is expected to be due only to refractive index variations upon absorption of analyte inside the polymer.

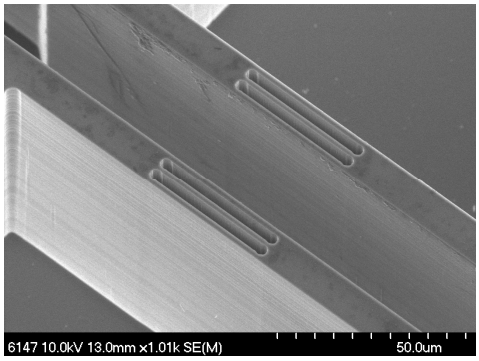

Figure 6.11: A Fabry-Perot interferometer, prior to polymer coating, in which the mirrors layer are shorter and thicker in order to be undeformable upon polymer expansion.

The interferometer presented in Figure 6.11was coated with PDMS, using the procedure described in section 6.4.2, and was exposed to various concentrations of m-xylene. The results are presented in Figure 6.12 and yield a 0.00048 nm/ppm sensitivity. This is more than one order of magnitude smaller than what is obtained using deformable interferometers (0.014 nm/ppm, see Figure 6.7), and is in agreement with the theoretical models (see Figure 6.6).

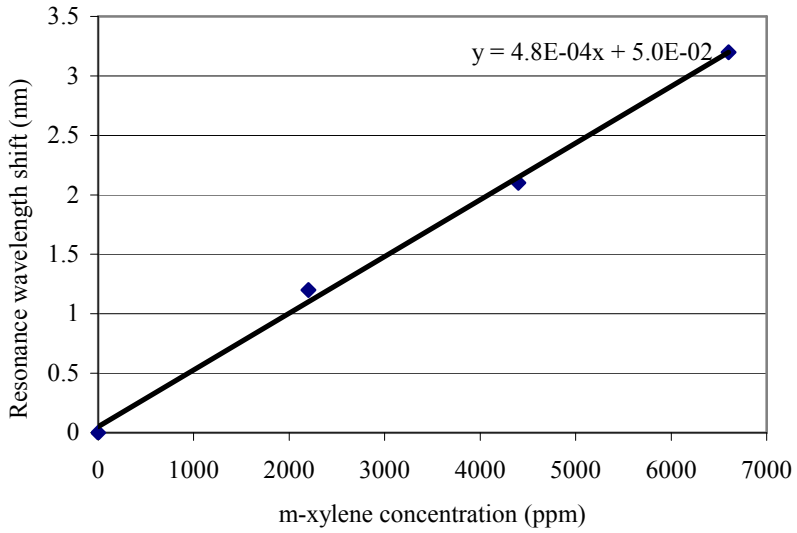

Figure 6.12: Resonance wavelength shift as a function of m-xylene concentration for the device of Figure 6.11 coated with PDMS. A 0.00048 nm/ppm sensitivity is obtained.

CHAPTER 7 SILICON-ON-INSULATOR IN-PLANE GIRES-TOURNOIS INTERFEROMETERS

This chapter is a reproduction of an article[8] relating the fabrication and characterization of in-plane waveguided Gires-Tournois interferometers for applications in optical fiber telecommunication networks. For more details on the basic ideal properties of such interferometers and on potential applications, please refer also to Chapter 3, section 3.2.

7.1 Authors and affiliation

Raphael St-Gelais, Thomas Kerrien, Hubert Camirand, Alexandre Poulin, and Yves-Alain Peter

Department of Engineering Physics, Ecole Polytechnique de Montréal, P.O. Box 6079, Station Centre-Ville, Montréal, Quebec H3C 3A7, Canada

7.2 Abstract

Gires-Tournois interferometers (GTIs) based on deep-etched silicon-air Bragg mirrors and on optical quality dicing of silicon are reported. Broadband reflectivity of the deep-etched Bragg mirrors allows operation on a wavelength range exceeding the C Band window. The waveguided in-plane configuration of the devices allows interferometers lengths that are not typically achievable on chip using out-of-plane designs (e.g., $L > 1$ mm for a 25 GHz free spectral range). Optical characterization of GTIs having two different free spectral ranges (i.e., 25 and 100 GHz) yield off-resonance insertion losses below 2 dB and polarization dependant losses (PDL) below 1 dB. Insertion losses and PDL are however more important near the resonance wavelengths, reaching respectively 15 dB and 5 dB. Calculations show that the reported devices could be useful for Michelson-GTI bandpass filters, such as optical interleavers.

Index Terms—Integrated optics, Interferometers, Optical waveguides, Silicon on insulator technology.

---

[8] R. St-Gelais, T. Kerrien, H. Camirand, A. Poulin, and Y.-A. Peter, "Silicon-on-insulator in-plane Gires-Tournois interferometers," *IEEE Photonics Technol. Lett.,* vol. 24, pp. 2272-2275, 2012.

7.3 Introduction

Deep-etched silicon-air Bragg reflectors were previously integrated with waveguides to form tunable in-plane Fabry-Perot cavities [11, 14]. In the current work, we investigate similar devices, in which the two silicon-air mirrors now have different reflectivities in order to form on-chip Gires-Tournois interferometers (GTIs). GTIs are mainly used for optical fiber dispersion compensation [119, 120] and in Michelson-GTI band-pass filters [59] such as optical interleavers [121-124]. Previous on-chip integrations of GTIs relied on out-of-plane configurations [56, 125] (optical axis perpendicular to the substrate surface). The devices presented in the current work are based on an in-plane configuration, which could be advantageous, in some contexts, compared to out-of-plane devices. For example, in this configuration, the length (L) of the interferometer is not limited, as in [56], by the thickness of the substrate. Its free spectral range (FSR) can therefore be designed with great flexibility, from a 25 GHz DWDM (dense wavelength-division multiplexing) channel spacing (L > 1 mm), to FSR > 100 nm (L < 5 μm). The waveguided in-plane configuration could also permits, through design and fabrication process modifications, monolithic integration with other on-chip components such as couplers, signal modulators, and electrical circuits for spectral tuning (e.g., thermo-optic effect, carrier injection).

7.4 Design and Fabrication

An in-plane GTI is presented in Figure 7.1. The high reflectivity mirror (at the back of the cavity) is formed by plasma etching of a 3 μm period silicon-air Bragg mirror down to the buried oxide layer of a silicon on insulator wafer (11.5 μm thick silicon device layer). The waveguide cladding is then fabricated through a second photolithography and plasma etching step. The low reflectivity mirror is finally formed by dicing the waveguide entrance facet using an ADT 7100 provectus dicing saw equipped with a small diamond grit, resinoid matrix blade (ADT Part number 00777-8003-006-QKP). A protective photoresist coating is applied prior to dicing to ensure sample cleanliness. The sawing parameters are optimized (36,500 RPM, 1 mm/s feed speed) to ensure optical surface quality and low edge chipping.

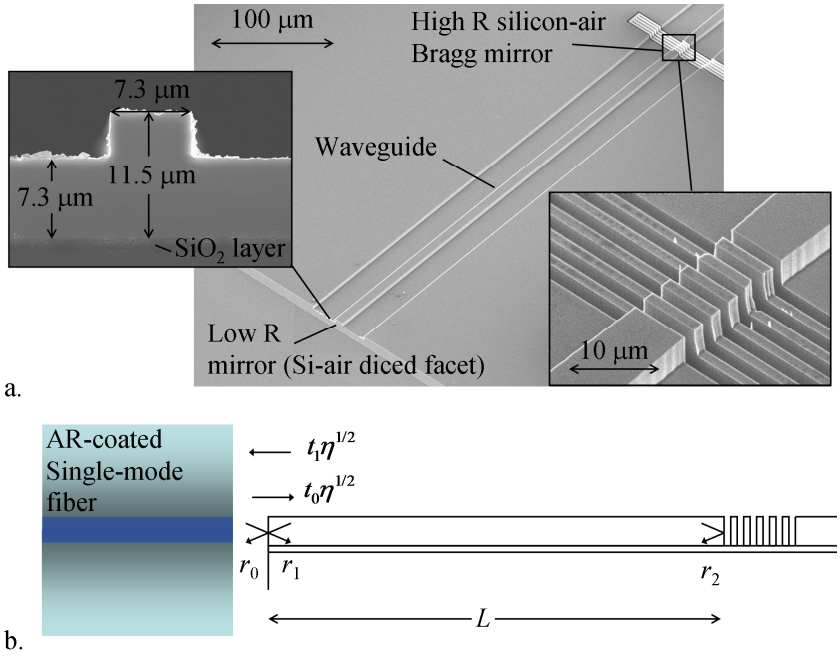

Figure 7.1: Scanning electron microscopy pictures (a) and schematic cross-section view (b) of a silicon-on-insulator Gires-Tournois interferometer.

The amplitude reflection (r) and transmission (t) coefficients at each mirror are defined in Figure 7.1 (b). The parameter η designates the intensity coupling coefficient between the anti-reflection coated single-mode fiber (Oz optics) and the waveguide. Using this notation, the amplitude reflection coefficient of the interferometer is given by Eq. (7.1), where $\beta = 2\pi n_{eff}/\lambda$ and L are the propagation constant and the length of the waveguide, respectively.

$$r_{GT} = r_0 + \frac{\eta t_0 t_1 r_2 e^{-2i\beta L}}{1 - r_1 r_2 e^{-2i\beta L}} \tag{7.1}$$

As the waveguide cross section is relatively large, we expect the effective index to be determined essentially by silicon material dispersion, which yield $n_{eff} \approx 3.60$ at $\lambda = 1500$ nm. An imaginary part can also be added to n_{eff} to account for propagation losses. These are however found to have little influence on the calculated response and are therefore roughly approximated to a realistic 2 dB/cm value.

The nominal thicknesses of the silicon and air layers (1.5 μm each) that constitute the back mirror are as small as possible, to yield the highest possible reflection bandwidth, but are

large enough to remain easily definable by contact lithography. Upon photolithography (e.g. diffraction) and plasma etching (e.g. mask undercut), the thickness of the air layers typically increases to 1.8 μm, while the silicon layers thicknesses decrease, proportionally, to 1.2 μm (i.e. the 3 μm silicon-air period is invariant). Using these dimensions, the amplitude reflection coefficient of the back mirror (r_2) is calculated with the model presented in [103]. This model accounts for losses due to Gaussian beam divergence and surface roughness at the plasma-etched material interfaces. As shown in Figure 7.2, when no surface roughness is considered, the mirror is expected to yield broadband (>100 nm) high reflectivity (>99.9 %) over the S and C telecommunication bands. However, when surface roughness is considered, the reflectivity is expected to decrease strongly, due to scattering losses.

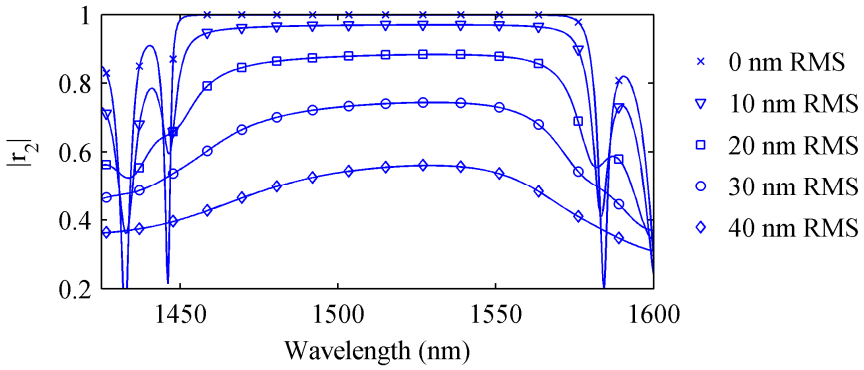

Figure 7.2: Simulated amplitude reflection spectra of the Gires-Tournois back mirror (r_2), for various amounts of surface roughness at the silicon-air material interfaces. In the ideal case (no surface roughness), reflectivity exceeds 99,9% over the S and C telecommunication wavelength bands.

The same model [103] can be used to predict the (r_0, r_1, t_0, t_1) coefficients of the entrance reflective facet. However, as we deal with large cross section modes, and as surface roughness on the diced facet is very low (5 nm RMS measured by white light interferometry in Figure 7.3 (b)), their value can be approximated as the normal incidence silicon-air Fresnel coefficients (within an error < 2%). Finally, the fiber-waveguide intensity coupling coefficient (η = 0.862) is

calculated from the waveguide mode profile (Figure 7.3 (a)), simulated using the dimensions presented in Figure 7.1 (a) (beam propagation method, RSoft Photonics CAD Suite).

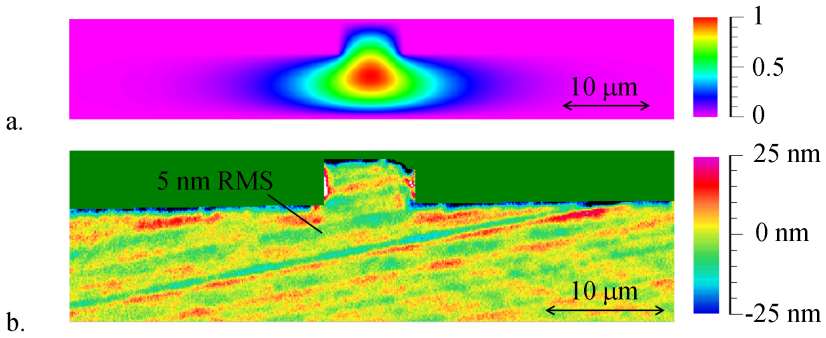

Figure 7.3: (a) Simulated amplitude mode profile (arbitrary units) of the fabricated waveguide. (b) Measured roughness (5 nm RMS) of a diced silicon-air waveguide facet, which forms the low reflectivity (R = 30.6%) entrance mirror of the GTIs. The diced surface quality is significantly better than what is obtained (35 nm RMS) inside the plasma etched silicon-air Bragg mirrors (see plasma etched roughness profiles in [103]).

7.5 Results and Discussion

Gires-Tournois interferometers having two different FSR (100 GHz and 25 GHz) were fabricated and characterized. The measurements were performed with an Agilent 86038B photonic dispersion and loss analyzer and are presented in Figure 7.4, together with the simulated response obtained using Eq. (7.1).

Figure 7.4 (a) presents the measured reflectivity of a 100 GHz device over the C Band wavelength range, outlining the broadband operation of the device. In Figure 7.4 (b), the same device is characterized on a narrower range, showing two resonance peaks near λ = 1549.7 and λ = 1550.5 nm. The off-resonance parts of the spectrum yield interestingly low insertion losses (< 2dB). The losses are however more important near the resonance peaks (15 dB). Figure 7.4 (c) presents the characterization of a longer, 25 GHz FSR, Gires-Tournois interferometer, which is found to behave similarly as the 100 GHz device. The off-resonance losses are slightly higher in this case (~2.5 dB), most likely due to the longer propagation length in the waveguide or to fabrication variations.

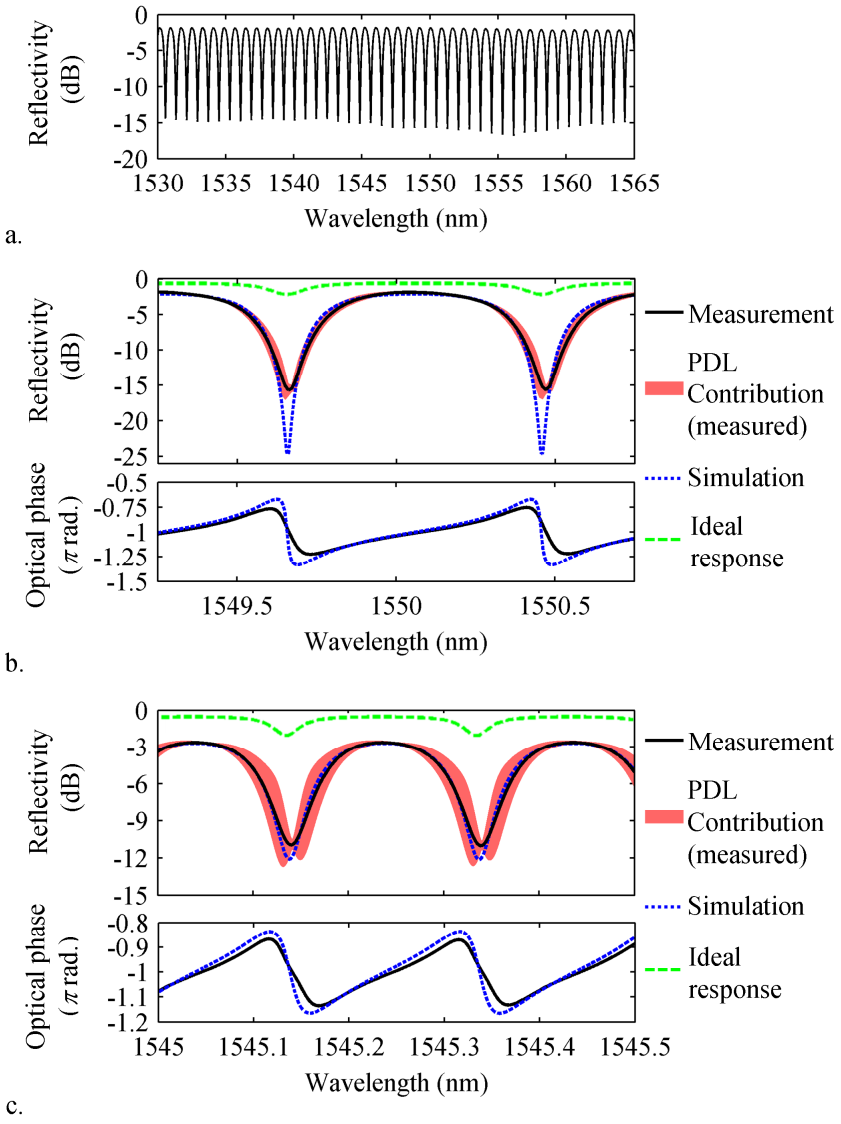

Figure 7.4: (a) Measured reflectivity of a 100 GHz FSR interferometer over the C band wavelength range. (b, c) Measurement of the magnitude and phase response, and comparison with the theoretical model, for (b) 100 GHz and (c) 25 GHz FSR Gires-Tournois interferometers. The PDL contribution area indicates the measured range of values for all possible polarization states.

In Figure 7.4 (b, c), the best fit between the simulations (Eq. (7.1)) and the experimental results is obtained by reducing the fiber-waveguide coupling coefficient by 20% (η = 0.7), to account for misalignment errors, and by considering 35 nm RMS surface roughness in the plasma-etched multilayer mirror. Such amount of surface roughness is consistent with previously reported measurements of surface roughness in deep-etched trenches [103]. Using these roughness and coupling values in Eq. (7.1), surface roughness in the deep-etched back mirror is found to be the main source of wavelength-dependant losses. Fiber-waveguide coupling losses (η) also contribute, in a smaller extent (~3 dB), to wavelength-dependant losses, while the contribution of waveguide propagation losses is expected to be negligible (< 1 dB when considering a 2 dB/cm propagation loss coefficient).

Important reductions of the device insertion losses would therefore be achievable mainly through improvement of our etching process, rather than by design optimization. The most promising possibility would be to replace our room temperature plasma etching process by a cryogenic etching recipe. Cryogenic etching previously allowed fabrication of high finesse Fabry-Perot resonators based on deep-etched silicon-air Bragg mirrors [14], which is possible only with very low amounts of surface roughness. In the ideal case (i.e. without roughness or waveguide propagation losses, and with η = 0.862), the reflectivity of the proposed GTIs could reach -0.5 dB off-resonance with 1.5 dB wavelength-dependant losses (see the "Ideal response" traces in Figure 7.4 (b, c)).

For the 100 GHz FSR device (Figure 7.4 (b)), polarization dependant losses (PDL) are low at off-resonance wavelengths (< 1 dB on more than 50 % of each FSR). PDL however reach 5 dB near each resonance peak. The waveguide most likely has two slightly different effective indices for each of its two principal polarization axis. The resonance peak positions are therefore slightly shifted as a function of the input polarization, which cause important PDL near resonance. For the reported devices, decreasing wavelength-dependant losses would therefore also proportionally decrease PDL.

PDL is more important for the 25 GHz FSR device (Figure 7.4 c) than with the 100 GHz interferometer, most likely due to the longer waveguide that causes a larger phase shift between the two polarization axes. However, at off resonance wavelengths, PDL below 1 dB is still obtained on wavelength bands corresponding to 40% of each FSR. In Figure 7.4 (c), near each

resonance wavelength, the PDL trace yields two clearly distinguishable resonance peaks, which allow us to determine the waveguide birefringence (Δn_{eff}). The measured value ($\Delta n_{eff} = 4.1 \times 10^{-5}$) is consistent with what is expected ($\Delta n_{eff} = 2.4 \times 10^{-5}$) from the beam propagation method simulations presented in Figure 7.3 (a).

As both GTIs characterized in Figure 7.4 yield important signal losses (>10 dB) and PDL (>5 dB) at resonance, their use in optical fiber dispersion compensation devices appears unrealistic. Such devices typically exploit several cascaded GTIs [119], which would each cause >10 dB wavelength-dependant losses. Moreover, due to important signal losses, negative phase shifts occur at the resonance wavelengths (Figure 7.4 (b, c)). These negative shifts translate in a negative group delay regime that is typically unsuited for dispersion compensation.

However, the proposed interferometers could find interesting applications in Michelson-GTI (MGTI) bandpass filters such as optical interleavers. These devices typically exploit the off-resonance parts of the GTI spectrum which, in the present case, yield low insertion losses and PDL. The input mirror reflectivity ($r = 0.55$), for the reported GTIs, is also close to the value that is optimal ($r = 0.4$) for flat-top interleaving [59]. As an example, in Figure 7.5, the interleaving capability of a 100 GHz FSR GTI is simulated using Eq. (7.1) (with the parameters that allowed the best fit with the experimental results in Figure 7.4) and the formalism described in [59]. The reference mirror (in the second arm of the Michelson) is considered to have an R = 60 % ideal reflectivity. Such MGTI could be implemented, as in [124], using a 50/50 optical fiber coupler and by adjusting the reference arm length with a fiber stretcher.

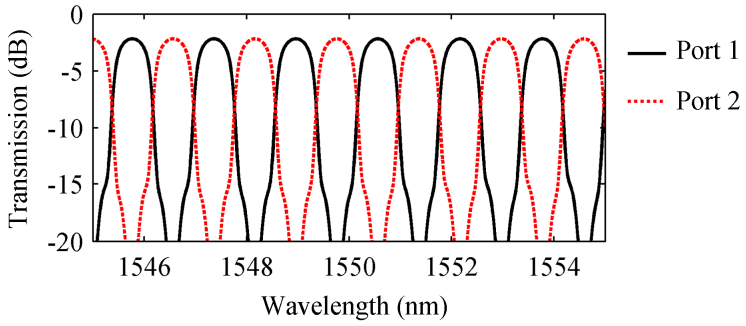

Figure 7.5: Simulated interleaving capability of the reported Gire-Tournois when integrated within a Michelson interferometer. The interferometer presented in Figure 7.4 (b) is considered as the mirror in one arm of the Michelson, while the other arm has an R = 60% ideal mirror.

The simulated response of the MGTI interleaver yields 2 dB insertion losses, channel isolation in the order of 20 dB, and 50 GHz passband width (at -0.5 dB). These parameters are mostly limited by surface roughness in the deep-etched silicon-air Bragg mirror. Improving our etching process could therefore considerably improve the expected insertion losses, channel isolation, and flat-top response. Using an index matching fluid between the optical fiber and the waveguide could also improve the flat-top response by bringing the entrance mirror reflectivity closer to the ideal value ($r = 0.4$).

Tuning by thermo-optic effect or by carrier injection could compensate for drifts due to ambient temperature variations. Electromechanical tuning was previously achieved in similar devices [78]. However, this mechanism changes the dimensions of some of the air layers inside the silicon-air Bragg mirror, which was found to induce important signal losses. Tuning by mechanisms that do not involve deformations of the Bragg mirror (e.g., thermo-optic effect, carrier injection) therefore appears preferable.

As for other waveguided planar lightwave circuit, packaging of the proposed GTIs would require high precision optical alignment (~ 1 μm tolerance). Such tight tolerance could be achieved through the integration of passive optical fiber alignment grooves. These grooves could be monolithically integrated on same wafer as the GTIs, and would be exposed to the waveguide facet through the optical quality dicing step.

7.6 Conclusion

We reported what is, to our knowledge, the first in-plane implementation of a silicon-on-insulator Gires-Tournois interferometer. A simple analytical model of the device response is also proposed and is found to correspond well with the experimental results. The devices yield low loss and low PDL at off-resonance wavelengths. However, high loss and PDL were observed at resonance. These losses are caused mostly by surface roughness in the deep-etched silicon-air Bragg mirror, and could therefore be reduced by improving our plasma etching process. Without major improvements, the use of the proposed GTIs in dispersion compensating devices appears unrealistic. However, calculations show that the current devices responses could yield useful performances in Michelson-GTI bandpass filters such as optical interleavers.

CHAPTER 8 DISCUSSION - POSSIBILITIES AND LIMITATIONS OF DEEP-ETCHED SILILION-AIR MULTILAYER INTERFEROMETERS

The models and experimental results provided in this work allow, in the author's opinion, the formulation of clear boundaries on the possibilities and limitations of on-chip interferometers based on deep-etched multilayer reflectors.

8.1 Low loss filtering and signal processing - a challenging goal

8.1.1 Insights on tunable filtering applications

Considering the models provided in Chapter 4 and current silicon processing technologies, it appears that targeting simultaneously low insertion losses and strong light confinement (i.e. high finesse) in deep-etched silicon-air multilayer resonators is an extremely challenging, if not unrealistic, goal. Let us consider, for example, free-space tunable Fabry-Perot filters such as those presented in [12, 18-22]. In order to compete with commercially available devices [23], these filters would need to reach finesses above 1000 and insertion losses below -3 dB. For such finesse, a silicon-air Fabry-Perot filter would require at least 2.5 silicon-air periods per mirror (Chapter 2, Table 2.1). In turn, for this amount of silicon-air periods, limiting divergence losses below -3 dB would require a Gaussian beam waist larger than 20 μm (Chapter 4, Figure 4.3), which is not yet too problematic if lensed optical fibers are used.

The main limitations arise from the required surface quality and verticality in the etched multilayer structures. Surface roughness below 3 nm RMS (Chapter 4, Figure 4.9), and verticality deviations below 0.5 nm (Chapter 4, Figure 4.17) would be required to meet the targeted performances. The latter requirement appears particularly unrealistic. Indeed, a 0.5 nm thickness deviation, over a 40 μm beam diameter, would require a 0.001° precision on the etch angle. For comparison, a 40 times larger uncertainty (0.04°) was achieved in the current work (see Chapter 4, Figure 4.19). The required surface quality (3 nm RMS) is also one order of magnitude larger than what was achieved in this work (30 nm RMS, see Chapter 4, Figure 4.4). It is possible that a post-etching surface treatment method, such as preferential etching along crystallographic planes [24, 72-75], could improve surface quality enough to meet the targeted roughness value.

However, this post-etching treatment typically etches uncontrollably any feature that is not precisely aligned with silicon crystallographic planes, yielding unpredictable fabrication results. This method therefore greatly restricts design flexibility which, as discussed in introduction, is probably the main advantage of deep-etched silicon interferometers.

The above-listed requirements for low loss operation can be substantially relaxed if waveguided, rather than free-space, optical cavities are designed. In this case, beam divergence losses are limited by the waveguided cavity, allowing the use of a much smaller beam diameter. Smaller beam diameters reduce the required precision on the etch angle. For example, if a 5 μm thick silicon waveguide is used (i.e. beam diameter ~ 4 μm), such as in [14], a 0.5 nm maximal thickness deviation due to imperfect verticality requires a 0.01° precision on the etch angle (i.e. an order of magnitude larger than with free-space interferometers and not too far from the 0.04° precision achieved in this work). Reducing the etch depth by designing thin waveguides can also improve surface quality. With a 5 μm thick waveguide, and considering a 1:30 maximum aspect ratio during plasma etching, trenches width as small as 200 nm can be designed. As previously reported [49], surface roughness typically decreases with trench width.

The improvements on verticality and surface roughness allowed by waveguided optical cavities are most likely the reason why the only demonstration of high finesse in a deep-etched Fabry-Perot was achieved with a waveguided cavity [14]. In that case, electron beam lithography was used to define very narrow trenches (< 400 nm), which most likely improved surface quality compared with other reports (including the current work) that are based on conventional optical lithography (trench width > 1 μm). Silicon was also etched using a cryogenic temperature ICP etching process. As discussed in Chapter 2, section 2.2.4, low temperature etching improves the etch mask resistance to ion bombardment, allowing operation at a particularly low pressure (7 mtorr [13]). In turn, this low pressure most likely allowed a better control on the etch angle by reducing the etch ions angular distribution (IAD, see Chapter 2, section 2.2.2).

The fabrication technologies (e-beam lithography, cryogenic etching) used in Pruessner et al. work [13, 14] are a good illustration of the technological challenges associated with applications (e.g. narrow band tunable filters) requiring strong light confinement. E-beam lithography and cryogenic etching are indeed employed mostly in research contexts, while their more reliable counterparts (optical lithography and room temperature plasma etching) are the

methods of choice of most microfabrication industries. As discussed extensively in the current work, the latter technologies did not so far allow deep-etched interferometers to reach high finesses and low insertion losses. Moreover, while e-beam lithography and cryogenic etching allowed relatively high finesses in waveguided Fabry-Perot interferometers [13, 14], insertion losses are still important. These insertion losses are caused by the necessity to couple a relatively wide optical fiber mode ($2\omega_0$ ~ 10 μm) into a 5 μm height waveguide (10 dB coupling losses), and by intrinsic cavity losses (~ 6 dB) [15].

Therefore, considering currently available fabrication technologies, the probability of witnessing the development of deep-etched multilayer interferometers presenting simultaneously low insertion loss and high light confinement abilities (e.g. high finesse) is, in the author's opinion, very low. Research on tunable filters should therefore focus on applications in which other competitive advantages of deep-etched devices overcome the limitations of high insertion losses and passband broadening. For example, in [22], a deep-etched filter is integrated into a tunable laser for optical coherence tomography applications. The in plane implementation of the filter allows its monolithic integration with a push-pull micromechanical actuator. This actuator allows linear laser wavelength scans as a function of the input voltage, which is of great importance for spectrally encoded imaging applications. Such actuator is based on two interdigitated comb drives and three electrodes, and is therefore virtually impossible to implement in an out-of-plane configuration.

8.1.2 Gires-Tournois interferometers

Rather than targeting applications that require, at the same time, low insertion losses and strong light confinement (e.g. tunable filters), a potentially viable direction for deep-etched interferometers would be applications that intrinsically require weak light confinement. We hypothesized in introduction (section 1.2) that such interferometers could lead to less strong interaction of light with fabrication imperfections, leading to an important reduction of insertion losses. This hypothesis led, in Chapter 7, to the development of a deep-etched waveguided Gires-Tournois interferometer.

In that case, our objective of reaching low insertion loss was partially achieved. It was demonstrated that operating deep-etched interferometers in reflection, rather than in transmission, allowed low insertion losses (< 2 dB) at off resonance wavelengths. In this case, light did not

have to be transmitted through several silicon-air interfaces, each suffering from important surface roughness, before coupling back into the incident optical fibers. The achieved off resonance losses could allow useful applications, as discussed in Chapter 7 (section 7.5), in Michelson-GTI band pass filters such as interleavers for optical fiber telecommunication networks.

On the other hand, at resonance wavelengths, the device still suffered from important insertion losses (> 10 dB). These losses were caused by a still too strong interaction of light with surface roughness in the multilayer cavity back mirror. It therefore appears that using a waveguided cavity, as in [14], but avoiding the use of highly specialized fabrication technologies (e-beam lithography, cryogenic etching) was not sufficient to reach high enough mirror quality upon etching. Indeed, conventional lithography limited us to air layers widths larger than 1 μm, while e-beam lithography would have allowed significantly thinner air layers (e.g. 400 nm in [14]). The aspect ratio (1:7) in our fabricated mirrors was therefore significantly lower than in [14] (1:13) which, as discussed above in section 8.1.1 and in ref. [49], most likely resulted in more surface roughness at the silicon-air interfaces. It is also possible that cryogenic etching, a continuous passivation process, would have reduced surface roughness compared with our room temperature time-multiplexed etching. Indeed, as discussed in Chapter 2 (see Figure 2.8), time-multiplexed processes usually result in important surface scalloping, especially in low aspect ratio trenches [49].

In summary, weakly confining interferometers allowed acceptable insertion losses at off-resonance wavelengths, which is a significant improvement compared with other previously reported deep-etched interferometers, such as tunable filters. Insertion losses however remain high at resonance wavelengths due to a still too strong interaction of light with surface roughness in the cavity back mirror. The proposed device could therefore find useful applications but only in specific devices, such as Michelson-GTI band pass filters, that exploit the off-resonance parts of the interferometer spectrum. For other applications, such as tunable dispersion compensation, significant improvement of surface quality in deep-etched trenches would still be required. These improvements would most likely require fabrication technologies (i.e. e-beam lithography, cryogenic plasma etching) that are less widely employed in microfabrication industries.

8.2 On-chip sensors - a promising direction

While tunable filtering and signal processing applications are still limited by important insertion losses, sensing applications, on the other hand, readily yield performances that advantageously compare with other sensor technologies.

8.2.1 Refractive index sensing

In Chapter 5, a deep-etched free-space Fabry-Perot was used to measure the refractive index (RI) of liquids in a monolithically integrated microfluidic system. The resonance wavelength sensitivity to refractive index changes reached 907 nm/RIU. In comparison, we showed, in Chapter 3 (see Figure 3.5), that the fundamental upper sensitivity limit of Fabry-Perot RI sensors is the ratio of the operation wavelength (~ 1550 nm our case) over the refractive index of the analyte (~ 1.3 - 1.5 for most liquid samples). The sensitivity reached experimentally is therefore only 20 % inferior to the 1100 nm/RIU theoretical limit. This result outlines a very important property of Fabry-Perot sensors:

1. Resonance wavelength sensitivity to RI changes is not a function of finesse and insertion losses, but only of the overlap between the resonant mode and the targeted analyte.

In our case, the very high refractive index contrast between silicon and air allowed the use of relatively thin (i.e. few silicon-air periods) mirrors. Thin mirrors allowed much better light-analyte overlap compared, for example, with Fabry-Perot sensors based on fiber Bragg grating reflectors [85, 126], which yield orders of magnitude lower sensitivities.

Insertion losses and low finesses do, however, affect the limit of detection (LOD) of Fabry-Perot RI sensors [82]. For example, a 1 nm resonance wavelength shift would be easier to detect with, e.g., a 0.1 nm wide, high finesse resonance than with a broad (4 nm), low finesse peak such as in Chapter 5. The low finesse of our sensor was however found not to be a competitive disadvantage compared with all other microfluidic Fabry-Perot sensors that were reported either prior [85-88] or following [126, 127] our work. In all these cases, finesses never significantly exceed what was reported in Chapter 5. In the best case [127], a twofold finesse increase allowed a modest 35% improvement of the detection limit (1.1×10^{-5} RIU) compared with our work (1.7×10^{-5} RIU). Moreover, the sensor presented in Chapter 5 presents the important advantage of being fabricated simultaneously with the microfluidic system and with

passive fiber alignment grooves, while other Fabry-Perot sensors, such as [127], rely on more fabrication steps (i.e. thin film deposition following plasma etching) and require free-space alignment of out-of-plane interrogation optical fibers.

On-chip refractive index sensing devices are, of course, not limited to Fabry-Perot interferometers. Several other types of sensors exist (see dedicated reviews, e.g. [82, 90, 128, 129]), among which surface plasmon resonance (SPR) sensors [130] are probably the most widely acknowledged for their high resolution (10^{-7} RIU) and simple fabrication. A fundamental difference between Fabry-Perot and most other sensors is the depth of interaction of light inside the analyte. Most other sensors (e.g.: SPR, ring microcavities, long period fiber Bragg gratings) rely on evanescent light waves, which typically yield interaction depths smaller than 1 μm. While such interaction depth allows high resolutions for the detection of surface adsorbed, nanometer-sized bio samples, it is largely insufficient for the characterization of bigger species, such as living cells (diameter ~ 10 μm). For such larger bodies, sensors with penetration depths of several microns are required. We refer to these sensors as being "volumetric", as opposed to evanescent wave sensors that perform "surface" measurements. Volumetric sensing is, in the author's opinion, the second important property of deep-etched Fabry-Perot RI sensors:

2. In deep-etched Fabry-Perot RI sensors, the interaction depth of light inside the sample is several microns, making these sensors ideal for the characterization of relatively large biological samples such as cells.

Interferometric characterization of living cells was previously investigated using other types of Fabry-Perot sensors, which were based on metal-coated optical fibers [86] and on out-of-plane mirrors [88]. In all these cases, however, cells needed to be immobilized before being characterized individually; resulting in largely insufficient cell counts (~ 10 cells) compared with commercially available flow cytometers and hematology analyzers that perform several thousand counts per second [131]. In our case, the great design flexibility of deep-etched sensors permits the integration of microfluidic and optical features that will allow cells to be characterized in flow (i.e. avoiding the need for individual cells immobilization). Preliminary results were already obtained [132] and proved the differentiation, in-flow, of two glass beads sub populations based on their diameters. The device used in this report [132], is essentially the same as in Chapter 5, except for the use of waveguides that carry the incident and transmitted light, and of a more

sophisticated microfluidic system that allows single cells injection [132] into the interferometer (see Figure 8.1). Results demonstrating in-flow differentiation of living cells subpopulations were also recently obtained and should be reported shortly.

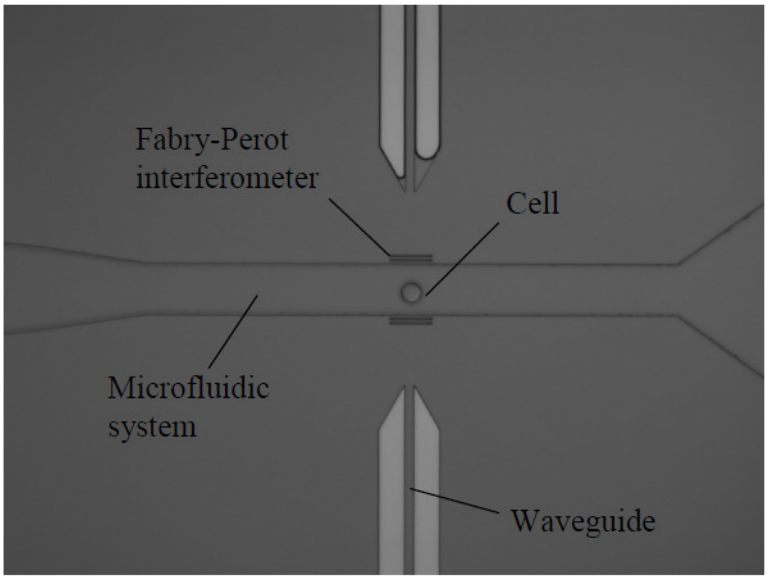

Figure 8.1: Optical microscope view of a cell (EL4 mouse lymphoma line) flowing through a deep-etched Fabry-Perot sensor. The same sensor allowed differentiation of glass bead subpopulations in [132]. Picture courtesy of Antoine Leblanc-Hotte.

8.2.2 Gas sensing

In Chapter 6, deep-etched multilayer interferometers, similar to those used for refractive index sensing in Chapter 5, were functionalized with PDMS-based gas absorbent polymers. Upon gas absorption, refractive index variations in these polymers were found to induce measurable shifts of the interferometer resonance wavelength, as in Chapter 5. The polymers were also found to expand (swell) proportionally with the absorbed analyte volume, deforming the interferometers, and participating to the resonance wavelength shift. In fact, polymer swelling-induced deformations were found to be the dominant sensing mechanism, yielding a 10 times higher sensitivity than refractive index variations.

The highest sensitivity (0.023 nm/ppm) was reached when detecting meta-xylene (m-xylene) vapors with a phenyl-doped PDMS polymer (PDMS-PDPS). As discussed in Chapter 6

(section 6.5), this sensitivity is similar to what was obtained, for a similar analyte (toluene), using out-of-plane deformable Fabry-Perot interferometers [101]. Such correspondence indicates that the in-plane implementation of deformable Fabry-Perot sensors—while greatly improving sensor integrability—did not cause sensitivity reductions compared with out-of-plane designs.

In-plane implementation allowed monolithic integration of alignment grooves for remote interrogation with optical fibers, while out-of-plane devices typically rely on on-site free-space alignment of light sources and detectors [100, 101]. It also allowed monolithic integration of microfluidic systems. These microfluidic systems facilitated coating of arrayed interferometers with different polymers. Comparatively, parallel polymer functionalization, in out-of-plane devices, typically requires complex assembly of silicon sub-parts [101].

While our in-plane sensor yield similar sensitivities than out-of-plane devices, our reported limit of detection (1.6 ppm m-xylene) is almost two orders of magnitude larger than in [101] (0.028 ppm toluene). This significantly better LOD of out-of-plane devices was however not achieved through better sensitivities or better optical properties (e.g. finesse), but by optimizing a free-space optical interrogation setup for low concentration measurements. The angle of incidence of the interrogation laser was adjusted to maximize interferometric response at a fixed wavelength of operation. Real-time referencing of the laser power was also used to minimize noise. Although this approach allowed better LODs (which is very relevant for applications such as gas chromatography [101]), its dynamic range is limited unless constantly adjusting the incidence and collection angles of the laser and photodetector. It is therefore less suited, compared to the proposed in-plane devices, for applications that would require larger dynamic range, field deployment and passive remote interrogation (e.g., industrial artificial olfaction).

It is interesting to push further the comparison of our sensor by including other types of well established micromechanical sensing technologies. This comparison is presented in Table 8.1. We also include, in Table 8.1, the only other report of a gas sensor based on a deep-etched silicon-air Fabry-Perot [16] interferometer. When possible, the comparison is carried for the same analyte as in our work (xylene) or for toluene (TOL), a BTEX of similar molecular structure, polarity and solubility parameter [92]. For Pruessner et. al. work, however, the comparison is carried for water vapor; the only analyte reported in [16].

Table 8.1: Limit of detection (LOD) compared with other micromechanical sensors

Sensor type[a]	Analyte[b]	Absorbent Polymer	LOD (ppm)	Ref.
In-plane FPI	XYL	PDMS-PDPS	1.6	Current work
FPI readout resonant MEMS	H_2O	Polyethyleneimine	68	[16]
Cantilever	TOL	Polyetherurethane	0.38	[133]
SAW	XYL	PDMS-PDPS	3.5	[118]
QCM	XYL	PDMS	1.2	[117]

[a] FPI - Fabry-Perot interferometer; QCM - quartz crystal microbalance; MEMS - microelectromechanical system; SAW - surface acoustic wave. [b] XYL - xylene; TOL - toluene.

Table 8.1 indicates that the m-xylene LOD, for the first proof-of-concept devices reported in the current work, is on the same order of magnitude as with sensors based on more mature micromechanical sensors technologies (Cantilever, SAW, QCM). Our device could therefore potentially compete with micromechanical sensors (SAW, QCM) that already find commercial applications in artificial olfaction systems [115, 116]. Moreover, as discussed also in Chapter 6, a possible advantage of deformable Fabry-Perot sensors is their potential for field deployment and remote interrogation. As opposed to all the sensors presented in Table 8.1, deformable Fabry-Perot interferometers do not necessitate any local source of energy to operate. Sensor heads could therefore be deployed in industrial work places and would be linked to an interrogation unit only through conventional optical fibers. These optical fibers would allow negligible signal loss over distances of several kilometers.

Compared to the only other report of a gas sensor based on a deep-etched silicon-air Fabry-Perot [16], our sensor allows an almost two orders of magnitude improvement of the limit of detection (Table 8.1). Moreover, the limit of detection reported in [16] was obtained with water vapor as the analyte. Commercially available water absorbent polymers typically have partitioning coefficient ($K_{p\text{-}a} = 1.3 \times 10^5$ in [16]) that are significantly higher than for volatile organic compounds in PMDS-based polymers ($K_{p\text{-}a}$ = 300 - 3000 in Chapter 6). Our sensor could therefore outperform even more the device reported in [16] if the same analytes were targeted. Our proposed sensor is also simpler to fabricate (no e-beam lithography, no cryogenic temperature etching) and potentially simpler to package due to the integration of optical fiber alignment grooves.

Finally, it should be noted that the sensors reported in Chapter 6 were fabricated using the contour lithography fabrication method presented in Chapter 4. This method allowed fabrication of deep-etched Fabry-Perot interferometers with predictable optical layer dimensions. This result should facilitate the development of new applications by avoiding the need to characterize each interferometer individually prior to polymer functionalization.

In summary—due to their competitive performances (Table 8.1), their simple and predictable fabrication process, and their potential for field deployment and remote interrogation—deep-etched deformable Fabry-Perot gas sensors are the most promising devices presented in this work for applications in the short-term. For example, collaborations with industrial partners are currently being initiated for the development of gas sensors dedicated to underground mining environments.

CONCLUSIONS AND RECOMMENDATIONS

The first objective of this work—provide theoretical models for deep-etched silicon-air multilayer interferometers—was, in the author's opinion, successfully achieved. We demonstrated that Gaussian beam divergence and surface roughness are dominant sources of losses in deep-etched multilayer interferometers. Imperfect verticality of the etch profiles was also demonstrated to be, in general, a potentially important source of loss and finesse reduction. However, for the devices presented in this thesis, imperfect verticality was found to be negligible compared with the measured contribution of surface roughness. Finally, we saw that, for free-space interferometers working in transmission, lateral misalignment between incident and output optical fibers can generally be neglected.

These models evidenced why, to date, no previous interferometer based on deep-etched multilayer reflectors yielded simultaneously strong light confinement (i.e. high finesse) and low insertion losses. For example, in Chapter 8 (section 8.1.1), fabrications tolerances within which free-space tunable Fabry-Perot filters—one of the main topics investigated using deep-etched multilayer reflectors [12, 18-21]—could compete with commercially available filters were identified. These tolerances (surface roughness < 3 nm RMS, and verticality deviation < 0.001° over a Gaussian beam diameter > 40 μm) were found to be much stricter than what is achievable using current silicon fabrication techniques. We therefore conclude that unless major advances occur in silicon processing technologies, fabrication of deep-etched multilayer interferometers yielding, at the same time, strong light confinement and low insertion loss, is a highly challenging if not unrealistic goal. We consequently recommend that the development of new applications based on deep-etched silicon-air multilayers focuses on:

1. Devices which intrinsically require weak light confinement
2. Devices which primary function is not affected by insertion losses
3. Devices for which competitive advantages of in-plane integration overcome the limitations of high insertion losses and resonance peaks broadening.

The first recommendation led, in Chapter 7, to the development of a deep-etched Gires-Tournois interferometer (GTI) for optical telecommunication applications. As GTIs are all-pass cavities based on a low reflectivity mirror, we hypothesized (see introduction, section 1.2) that

weak light confinement would lead to less interactions of light with fabrication imperfections and, consequently, to less important insertion losses. This hypothesis was partially confirmed experimentally. At off-resonance wavelengths, insertion losses below 2 dB were obtained. This is, for example, significantly better than what was reached in all previous reports on deep-etched Fabry-Perot interferometers (> 10 dB). At resonance wavelengths, however, insertion losses remain important (10 - 15 dB), and are caused by to a still too strong interaction of light with surface roughness in the cavity back mirror. The reported GTIs could consequently be used in optical fiber telecommunications network, but only in applications, such as Michelson-GTI bandpass filters, that exploit primarily the off-resonance parts of the GTI spectra. These bandpass filters are typically used to create interleavers for dense wavelength multiplexing (DWDM) applications. Our proposed GTIs could be particularly useful for this application since their in-plane implementation allow longer interferometers than out-of-plane designs, which are limited by the silicon substrate thickness (~ 500 - 600 μm). Longer interferometers (> 800 μm) allow free-spectral ranges to match the 25 or 50 GHz channel spacing of DWDM networks. Thermal or electro-optic tuning of the cavity effective length could also allow compensation of environmental variations, as proposed in Chapter 3 (section 3.2.1.1).

The second recommendation (of the three listed above) led to the development of two different types of sensors in Chapter 5 and Chapter 6. In Chapter 5, a deep-etched free-space Fabry-Perot interferometer was monolithically integrated with a silicon microfluidic system and was used as a refractive index sensor for homogenous liquids. The sensitivity of this sensor reached 907 nm/RIU (Refractive index units), which is only 20% inferior to the theoretical limit ($\lambda/n \sim 1100$ nm/RIU) of Fabry-Perot interferometers operating around $\lambda = 1550$ nm and targeting liquid phase analytes ($n \sim 1.4$). As discussed in Chapter 8 (section 8.2.1), this result outlines a very important property of Fabry-Perot sensors: refractive index sensitivity is not a function of losses within the interferometer, but only of the overlap between the sample and the resonant light mode. In the present case, the very high refractive index contrast between the multilayer materials (silicon and air) allowed relatively thin mirrors and, consequently, very good light-sample overlaps. The resulting high sensitivity allowed, in turn, a high detection resolution (1.7×10^{-5} RIU), even if the measured shifting resonance peak was relatively broad (> 4 nm) and lossy (25 dB). Improving the finesse of our sensor could, of course, improve its resolution by making the spectral position of the resonance peak easier to locate. However, at the time of

publication, the resolution of our sensor was already found to be the highest achieved by a refractive index sensor that performs volumetric measurements in a microfluidic systems [60]. This resolution was later modestly outperformed (1.1×10^{-5} RIU resolution) using a different Fabry-Perot of slightly higher finesse [127]. We however believe that, perhaps more than its high resolution, two other particularities of our sensor offers competitive advantages over other technologies. Firstly, Fabry-Perot sensors perform volumetric refractive index measurements, which is ideal for samples (e.g.: cells) that are too large to be characterized using evanescent wave surface sensors (e.g. surface plasmon based sensor). Secondly, compared to most other Fabry-Perot sensors, our device is monolithically integrated with a silicon microfluidic system and with optical fiber alignment grooves. Such monolithic integration allows, in few microfabrication steps, parallelized fabrication of several devices on a single wafer, in addition to simplify packaging by enabling passive optical fiber alignment. It also allows great flexibility in the design of integrated microfludic systems. Such microfluidic systems can by used to inject, at a controlled rate, single cells towards the interferometer for in-flow characterization. Interferometric cells characterization therefore appears to be the most promising application of our reported Fabry-Perot refractive index sensor. As mentioned in Chapter 8, preliminary results with glass beads were recently reported [132], while differentiation of living cells subpopulations was very recently achieved and should be reported shortly.

In Chapter 6, Fabry-Perot interferometers, similar to those presented in Chapter 5, were functionalized with polydimethylsiloxane (PDMS) based polymers and were used to detect two different volatile organic compounds (VOCs), i.e. m-xylene and cyclohexane. Upon VOC absorption, polymer swelling (i.e. expansion) was found to mechanically deform the interferometers. These deformations translated in measurable shifts of the interferometer resonance wavelengths. Refractive index variations inside the polymers also contributed to these shifts, but more modestly, yielding an approximately 10 times lower sensitivity than mechanical deformations. These gas sensors benefited from the same advantages, in terms of integrability, than the refractive index sensors proposed in Chapter 5. Monolithically integrated microfluidic systems facilitated functionalization of arrayed interferometers with different polymers. Alignment grooves also allowed remote sensor interrogation with passively aligned optical fibers. In comparison, previous out-of-plane implementation of deformable Fabry-Perot sensors required complex assembly of silicon sub-parts for polymer parallelization, while optical interrogation

required on-site alignment of light sources and detectors. The limits of detection of our sensor are on the same order of magnitude as with mature micromechanical sensing technologies (surface acoustic wave, quartz crystal microbalance) that are used in commercial artificial olfaction systems (see Chapter 8, section 8.2.2). Our sensor could therefore potentially compete with these technologies. One of their main competitive advantages would be the possibility to interrogate several sensors—which could be deployed on several kilometres large areas—using only optical fibers, while other technologies require on-site electrical power supply for each sensor heads. It should also be noted that the sensors reported in Chapter 6 were fabricated using the contour lithography fabrication method described in Chapter 4. This fabrication method prevented unpredictable layer dimensions to occur upon fabrication (see problem statement in Chapter 2, section 2.3.2), avoiding the need for individual optical characterization prior to polymer functionalization. The reported gas sensors are consequently compatible with an eventual mass production of several dozens of devices per wafer. The fabrication process, for such mass production, would be relatively simple (two photolithography steps) and would require only conventional silicon fabrication techniques (room-temperature deep plasma etching, UV lithography).

The last recommendation of the three listed above was not applied directly in this thesis, but is well illustrated by the development of tunable lasers for optical coherence tomography applications[9] [22]. Although the deep-etched filters used in these lasers still suffered from low finesses and high insertion losses, their in-plane implementation allowed monolithic integration with a push-pull electromechanical actuator. Push-pull actuators allow linear spectral tuning as a function of the applied actuation voltage, which is of critical importance for spectrally encoded imaging applications. These actuators require two interdigitated comb drives, and are therefore virtually impossible to implement in an out-of-plane configuration. This work [22] is therefore a good example of a situation in which important advantages of deep-etched multilayer interferometers, in terms of integrability, overcome the limitations of high insertion losses and low finesses.

---

[9] The author contributed only sporadically to this work, which is therefore not included in the present thesis. Our aim here is to provide an example of a research direction that follows the third recommendation of the three listed at the beginning of the current section.

In summary, the first important contribution of this work was to provide a complete set of theoretical models for deep-etched silicon-air multilayer interferometers. These models allowed, considering current silicon fabrication technologies, formulation of clear boundaries on the possibilities and limitations of deep-etched silicon-air multilayer interferometers. Within these boundaries, we proposed three original devices with potential applications as biomedical sensors, chemical sensors and as passive components for optical fiber telecommunications. In Chapter 7, Gires-Tournois interferometers were, for the first time, implemented on-chip in an in-plane waveguided configuration. Weaker light confinement within these interferometers, compared with previous works that mostly focused on deep-etched Fabry-Perot cavities, allowed important reductions of insertion losses. Losses were decreased enough to envision telecommunication applications in specific devices, such as Michelson-GTI bandpass filters, that exploit the off-resonance part of GTI spectra. However, at resonance wavelengths, insertion losses are still too high for applications, such as dispersion compensation, that requires several cascaded interferometers. We therefore conclude that a significant step was taken towards practical applications in optical fiber telecommunications, but that important limitations due to insertion losses remain. For this reason, optical telecommunication applications of deep-etched multilayer interferometers appear to be less promising than sensing applications, for which insertion losses are not a critical limitation. In Chapter 5, deep-etched silicon-air Fabry-Perot refractive index sensors were proposed for the first time and were demonstrated to reach high refractive index resolutions (~10^{-5} RIU), despite relatively high insertion losses and low finesses. This resolution is among the highest reported for on-chip sensors that perform volumetric measurements in sample volumes (~ 1 picoliter) similar to those of single living cells. This achievement, combined with monolithic integration of the sensor with a silicon microfluidic system, makes the reported device very promising for characterization of cells population in flow. Preliminary results in this direction were already reported with glass beads [132]. Measurements on living cells were also very recently obtained and should be reported shortly. Finally, in Chapter 6, deformable Fabry-Perot chemical sensors were, for the first time, implemented in an in-plane configuration using deep-etched silicon-air multilayer reflectors. These sensors—because of their competitive limits of detection, their simple and predictable fabrication process, their potentially simple packaging, and their compatibility with field deployment and passive remote interrogation—are, of all devices presented in this thesis, seemingly the most promising for practical applications in the

short-term. An industrial collaboration is, indeed, currently being initiated for the development of gas sensors dedicated to underground mining environments.

BIBLIOGRAPHY

[1] R. Soref, "Mid-infrared photonics in silicon and germanium," *Nat. Photon.,* vol. 4, pp. 495-497, 2010.

[2] M. Bass, C. DeCusatis, J. M. Enoch, V. Lakshminarayanan, G. Li, C. MacDonald, V. N. Mahajan, and E. Van Stryland, *Handbook of Optics, Third Edition Volume IV: Optical Properties of Materials, Nonlinear Optics, Quantum Optics* McGraw-Hill, 2009.

[3] P. E. Ciddor, "Refractive index of air: new equations for the visible and near infrared," *Appl. Opt.,* vol. 35, pp. 1566-1573, 1996.

[4] A. Yariv and M. Nakamura, "Periodic structures for integrated optics," *IEEE Journal of Quantum Electronics,* vol. 13, pp. 233-253, 1977.

[5] T. Baba, M. Hamasaki, N. Watanabe, P. Matsutani, nbsp, A. Kaewplung, T. Mukaihara, F. Koyama, and K. Iga, "A Novel Short-Cavity Laser with Deep-Grating Distributed Bragg Reflectors," *Japanese Journal of Applied Physics,* vol. 35, p. 1390, 1996.

[6] Y. Yuan, T. Brock, P. Bhattacharya, C. Caneau, and R. Bhat, "Edge-emitting lasers with short-period semiconductor/air distributed Bragg reflector mirrors," *Photonics Technology Letters, IEEE,* vol. 9, pp. 881-883, 1997.

[7] M. Naydenkov and B. Jalali, "Advances in silicon-on-insulator photonic integrated circuit (SOIPIC) technology," in *Proceedings of the 1999 IEEE International SOI Conference* 1999, pp. 56-66.

[8] M. N. Naydenkov and B. Jalali, "Fabrication of high-aspect ratio photonic bandgap structures on silicon-on-insulator," in *Proc. SPIE, Integrated Optics Devices IV*, San Jose, CA, 2000, pp. 33-39.

[9] F. Laermer and A. Urban, "Milestones in deep reactive ion etching," in *TRANSDUCERS '05. The 13th International Conference on Solid-State Sensors, Actuators and Microsystems. Digest of Technical Papers.* , Seoul, Korea, 2005, pp. 1118-1121.

[10] C. A. Barrios, V. R. d. Almeida, and M. Lipson, "Low-Power-Consumption Short-Length and High-Modulation-Depth Silicon Electrooptic Modulator," *J. Lightwave Technol.,* vol. 21, p. 1089, 2003.

[11] C. A. Barrios, V. R. Almeida, R. R. Panepucci, B. S. Schmidt, and M. Lipson, "Compact silicon tunable Fabry-Perot resonator with low power consumption," *IEEE Photonics Technol. Lett.,* vol. 16, pp. 506-508, 2004.

[12] S. S. Yun and J. H. Lee, "A micromachined in-plane tunable optical filter using the thermo-optic effect of crystalline silicon," *J. Micromech. Microeng.,* vol. 13, pp. 721-725, 2003.

[13] M. W. Pruessner, W. S. Rabinovich, T. H. Stievater, D. Park, and J. W. Baldwin, "Cryogenic etch process development for profile control of high aspect-ratio submicron silicon trenches," *J. Vac. Sci. Technol., B,* vol. 25, pp. 21-28, 2007.

[14] M. W. Pruessner, T. H. Stievater, and W. S. Rabinovich, "Integrated waveguide Fabry-Perot microcavities with silicon/air Bragg mirrors," *Opt. Lett. ,* vol. 32, pp. 533--535, 2007.

[15] M. W. Pruessner, T. H. Stievater, and W. S. Rabinovich, "In-plane microelectromechanical resonator with integrated Fabry-Perot cavity," *Appl. Phys. Lett.,* vol. 92, p. 081101, 2008.

[16] M. W. Pruessner, T. H. Stievater, M. S. Ferraro, W. S. Rabinovich, J. L. Stepnowski, and R. A. McGill, "Waveguide micro-opto-electro-mechanical resonant chemical sensors," *Lab Chip,* vol. 10, pp. 762-768, 2010.

[17] M. W. Pruessner, T. H. Stievater, J. B. Khurgin, and W. S. Rabinovich, "Integrated waveguide-DBR microcavity opto-mechanical system," *Opt. Express,* vol. 19, pp. 21904-21918, 2011.

[18] B. Saadany, M. Malak, M. Kubota, F. Marty, Y. Mita, D. Khalil, and T. Bourouina, "Free-space tunable and drop optical filters using vertical Bragg mirrors on silicon," *IEEE J. Sel. Top. Quantum Electron.,* vol. 12, pp. 1480-1487, 2006.

[19] A. Lipson and E. M. Yeatman, "A 1-D photonic band gap tunable optical filter in (110) silicon," *J. Microelectromech. Syst.,* vol. 16, pp. 521-527, 2007.

[20] R. Mudachathi and P. Nair, "Low-Voltage Widely Tunable Photonic Crystal Channel Drop Filter in SOI Wafer," *J. Microelectromech. Syst.,* vol. 21, pp. 190-197, 2012.

[21] J. Masson, R. St-Gelais, A. Poulin, and Y.-A. Peter, "Tunable Fiber Laser Using a MEMS-Based In Plane Fabry-Pérot Filter," *IEEE J. Quantum Electron.,* vol. 46, pp. 1313-1319, 2010.

[22] A. Poulin, R. St-Gelais, N. Goulamhoussen, G. Zhu, C. Boudoux, and Y.-A. Peter, "In-plane MEMS-based Fabry-Perot filter for high-speed wavelength-swept semiconductor laser " in *Proceedings of the Solid-State Sensors, Actuators and Microsystems Workshop*, Hilton Head Island, South Carolina, 2012, pp. 401-404.

[23] (Accessed on October 17 2012). *Micron Optics, Inc.* . Available: http://www.micronoptics.com/

[24] A. Lipson and E. M. Yeatman, "Low-loss one-dimensional photonic bandgap filter in (110) silicon," *Opt. Lett.,* vol. 31, pp. 395-7, 2006.

[25] K. Zandi, J. A. Bélanger, and Y.-A. Peter, "Design and Demonstration of an In-Plane Silicon-on-Insulator Optical MEMS Fabry-Perot-Based Accelerometer Integrated With Channel Waveguides," *Journal of Microelectromechanical Systems,* vol. PP, pp. 1-7, 2012.

[26] A. Poulin, R. St-Gelais, and Y. Peter, "Coupled electro-mechanical transducers for vertical to horizontal motion translation," in *2012 Symposium on Design, Test, Integration and Packaging of MEMS/MOEMS (DTIP)*, 2012, pp. 240-243.

[27] M. Malak, F. Marty, N. Pavy, Y.-A. Peter, A.-Q. Liu, and T. Bourouina, "Cylindrical Surfaces Enable Wavelength-Selective Extinction and Sub-0.2 nm Linewidth in 250 μm-Gap Silicon Fabry-Pérot Cavities," *J. Microelectromech. Syst.,* vol. 21, pp. 171-180, 2012.

[28] V. A. Tolmachev, T. S. Perova, E. V. Astrova, B. Z. Volchek, and J. K. Vij, "Vertically etched silicon as 1D photonic crystal," *Phys. Status Solidi A,* vol. 197, pp. 544-548, 2003.

[29] G. Barillaro, A. Diligenti, M. Benedetti, and S. Merlo, "Silicon micromachined periodic structures for optical applications at λ = 1.55 μm," *Applied Physics Letters,* vol. 89, pp. 151110-151110-3, 2006.

[30] G. Barillaro, L. M. Strambini, V. Annovazzi-Lodi, and S. Merlo, "Optical Characterization of High-Order 1-D Silicon Photonic Crystals," *IEEE J. Sel. Top. Quantum Electron.,* vol. 15, p. 1359, 2009.

[31] S. Surdo, S. Merlo, F. Carpignano, L. M. Strambini, C. Trono, A. Giannetti, F. Baldini, and G. Barillaro, "Optofluidic microsystems with integrated vertical one-dimensional photonic crystals for chemical analysis," *Lab Chip,* vol. 12, pp. 4403-4415, 2012.

[32] V. A. Tolmachev, T. S. Perova, S. A. Grudinkin, V. A. Melnikov, E. V. Astrova, and Y. A. Zharova, "Electrotunable in-plane one-dimensional photonic structure based on silicon and liquid crystal," *Applied Physics Letters,* vol. 90, pp. 011908-011908-3, 2007.

[33] K. J. Vahala, "Optical microcavities," *Nature,* vol. 424, pp. 839-846, 2003.

[34] H. A. Macleod, *Thin-film optical filters*: Institute of Physics Publishing, 2001.

[35] A. A. Ayón, R. Braff, C. C. Lin, H. H. Sawin, and M. A. Schmidt, "Characterization of a Time Multiplexed Inductively Coupled Plasma Etcher," *Journal of The Electrochemical Society,* vol. 146, pp. 339-349, January 1, 1999 1999.

[36] M. Chabloz, Y. Sakai, T. Matsuura, and K. Tsutsumi, "Improvement of sidewall roughness in deep silicon etching," *Microsyst. Technol.,* vol. 6, pp. 86-89, 2000.

[37] F. Marty, L. Rousseau, B. Saadany, B. Mercier, O. Francais, Y. Mita, and T. Bourouina, "Advanced etching of silicon based on deep reactive ion etching for silicon high aspect ratio microstructures and three-dimensional micro- and nanostructures," *Microelectron. J.,* vol. 36, pp. 673-677, 2005.

[38] F. Gao, Y. Wang, G. Cao, X. Jia, and F. Zhang, "Improvement of sidewall surface roughness in silicon-on-insulator rib waveguides," *Applied Physics B: Lasers and Optics,* vol. 81, pp. 691-694, 2005.

[39] A. M. Hynes, H. Ashraf, J. K. Bhardwaj, J. Hopkins, I. Johnston, and J. N. Shepherd, "Recent advances in silicon etching for MEMS using the ASE™ process," *Sensors and Actuators A: Physical,* vol. 74, pp. 13-17, 1999.

[40] F. Laermer and A. Urban, "Challenges, developments and applications of silicon deep reactive ion etching," *Microelectronic Engineering,* vol. 67–68, pp. 349-355, 2003.

[41] H. C. Liu, Y. H. Lin, and W. Hsu, "Sidewall roughness control in advanced silicon etch process," *Microsyst. Technol.,* vol. 10, pp. 29-34, 2003.

[42] W. J. Park, J. H. Kim, S. M. Cho, S. G. Yoon, S. J. Suh, and D. H. Yoon, "High aspect ratio via etching conditions for deep trench of silicon," *Surface and Coatings Technology,* vol. 171, pp. 290-295, 2002.

[43] I. W. Rangelow, "Critical tasks in high aspect ratio silicon dry etching for microelectromechanical systems," Denver, Colorado (USA), 2003, pp. 1550-1562.

[44] K. Solehmainen, T. Aalto, J. Dekker, M. Kapulainen, M. Harjanne, and P. Heimala, "Development of multi-step processing in silicon on insulator for optical waveguide applications," *J. Opt. A: Pure Appl. Opt.,* vol. 8, pp. S455-S460, 2006.

[45] B. Volland, F. Shi, P. Hudek, H. Heerlein, and I. W. Rangelow, "Dry etching with gas chopping without rippled sidewalls," *J. Vac. Sci. Technol., B,* vol. 17, p. 2768, 1999.

[46] M. J. Walker, "Comparison of Bosch and cryogenic processes for patterning high-aspect-ratio features in silicon," 2001, pp. 89-99.

[47] C. C. Welch, A. L. Goodyear, T. Wahlbrink, M. C. Lemme, and T. Mollenhauer, "Silicon etch process options for micro-and nanotechnology using inductively coupled plasmas," *Microelectron. Eng.,* vol. 83, pp. 1170-1173, 2006.

[48] H. V. Jansen, M. J. d. Boer, S. Unnikrishnan, M. C. Louwerse, and M. C. Elwenspoek, "Black silicon method X: a review on high speed and selective plasma etching of silicon with profile control: an in-depth comparison between Bosch and cryostat DRIE processes as a roadmap to next generation equipment," *Journal of Micromechanics and Microengineering,* vol. 19, p. 033001, 2009.

[49] Y. Mita, M. Sugiyama, M. Kubota, F. Marty, T. Bourouina, and T. Shibata, "Aspect Ratio Dependent Scalloping Attenuation in Drie and an Application to Low-Loss Fiber-Optical Switches," in *Proceeding of the 19th IEEE International Conference on Micro Electro Mechanical Systems*, Istanbul, Turkey 2006, pp. 114-117.

[50] K. R. Williams, K. Gupta, and M. Wasilik, "Etch rates for micromachining processing-Part II," *J. Microelectromech. Syst.,* vol. 12, pp. 761-778, 2003.

[51] P. D. Atherton, N. K. Reay, J. Ring, and T. R. Hicks, "Tunable Fabry-Perot filters," *Opt. Eng.,* vol. 20, pp. 806-814, 1981.

[52] A. Muller, E. B. Flagg, J. R. Lawall, and G. S. Solomon, "Ultrahigh-finesse, low-mode-volume Fabry-Perot microcavity," *Opt. Lett.,* vol. 35, pp. 2293-2295, 2010.

[53] S. P. Pogossian, L. Vescan, and A. Vonsovici, "The single-mode condition for semiconductor rib waveguides with large cross section," *Journal of Lightwave Technology,* vol. 16, pp. 1851-1853, 1998.

[54] (Accessed on April 4th 2012). *Corning SMF-28 product information*. Available: http://www.corning.com/opticalfiber/products/

[55] M. W. Pruessner, T. H. Stievater, M. S. Ferraro, and W. S. Rabinovich, "Thermo-optic tuning and switching in SOI waveguide Fabry-Perot microcavities," *Opt. Express,* vol. 15, pp. 7557-7563, 2007.

[56] C. K. Madsen, J. A. Walker, J. E. Ford, K. W. Goossen, T. N. Nielsen, and G. Lenz, "A tunable dispersion compensating MEMS all-pass filter," *IEEE Photonics Technol. Lett.,* vol. 12, pp. 651-653, 2000.

[57] (Accessed on September 20th 2012). *Teraxion optical communication products* Available: http://www.teraxion.com/en/products/optical-communications

[58] B. J. Vakoc, W. V. Sorin, and B. Y. Kim, "A tunable dispersion compensator comprised of cascaded single-cavity etalons," *IEEE Photonics Technol. Lett.,* vol. 17, pp. 1043-1045, 2005.

[59] B. B. Dingel and M. Izutsu, "Multifunction optical filter with a Michelson-Gires-Tournois interferometer for wavelength-division-multiplexed network system applications," *Opt. Lett.,* vol. 23, pp. 1099-1101, 1998.

[60] R. St-Gelais, J. Masson, and Y.-A. Peter, "All-silicon integrated Fabry-Perot cavity for volume refractive index measurement in microfluidic systems," *Appl. Phys. Lett.,* vol. 94, p. 243905, 2009.

[61] C. K. Carniglia and D. G. Jensen, "Single-layer model for surface roughness," *Appl. Opt.,* vol. 41, pp. 3167-3171, 2002.

[62] Y. Mita, M. Kubota, T. Harada, F. Marty, B. Saadany, T. Bourouina, and T. Shibata, "Contour lithography methods for DRIE fabrication of nanometre–millimetre-scale coexisting microsystems," *J. Micromech. Microeng.,* vol. 16, pp. S135-S141, 2006.

[63] A. E. Siegman, *Lasers*: University Science Books, 1986.

[64] G. D. Landry and T. A. Maldonado, "Gaussian beam transmission and reflection from a general anisotropic multilayer structure," *Appl. Opt.,* vol. 35, pp. 5870-5879, 1996.

[65] J. W. Goodman, *Introduction to Fourier optics*: Roberts & Company Publishers, 2005.

[66] E.-G. Neumann, *Single-mode fibers*: Springer-Verlag, 1988.

[67] G. B. Arfken and H. J. Weber, *Mathematical methods for physicists*: Harcourt Academic Press, 1968.

[68] S. Yuan and N. A. Riza, "General formula for coupling-loss characterization of single-mode fiber collimators by use of gradient-index rod lenses," *Appl. Opt.,* vol. 38, pp. 3214-3222, 1999.

[69] M. J. de Boer, J. G. E. Gardeniers, H. V. Jansen, E. Smulders, M. J. Gilde, G. Roelofs, J. N. Sasserath, and M. Elwenspoek, "Guidelines for etching silicon MEMS structures using fluorine high-density plasmas at cryogenic temperatures," *J. Microelectromech. Syst.,* vol. 11, pp. 385-401, 2002.

[70] G. Barillaro, A. Nannini, and M. Piotto, "Electrochemical etching in HF solution for silicon micromachining," *Sensors and Actuators A: Physical,* vol. 102, pp. 195-201, 2002.

[71] D. Lee, K. Yu, U. Krishnamoorthy, and O. Solgaard, "Vertical Mirror Fabrication Combining KOH Etch and DRIE of (110) Silicon," *J. Microelectromech. Syst.,* vol. 18, pp. 217-227, 2009.

[72] W. H. Juan and S. W. Pang, "Controlling sidewall smoothness for micromachined Si mirrors and lenses," *J. Vac. Sci. Technol., B,* vol. 14, pp. 4080-4084, 1996.

[73] S. S. Yun, S. K. You, and J. H. Lee, "Fabrication of vertical optical plane using DRIE and KOH crystalline etching of (110) silicon wafer," *Sensors and Actuators A: Physical,* vol. 128, pp. 387-394, 2006.

[74] R. Agarwal, S. Samson, and S. Bhansali, "Fabrication of vertical mirrors using plasma etch and KOH:IPA polishing," *J. Micromech. Microeng.,* vol. 17, pp. 26-35, 2007.

[75] M. Shikida, N. Inagaki, H. Sasaki, H. Amakawa, K. Fukuzawa, and K. Sato, "The mechanism of selective corrugation removal by KOH anisotropic wet etching," *J. Micromech. Microeng.,* vol. 20, p. 015038, 2010.

[76] A. V. Tikhonravov, M. K. Trubetskov, A. A. Tikhonravov, and A. Duparré, "Effects of interface roughness on the spectral properties of thin films and multilayers," *Appl. Opt.,* vol. 42, pp. 5140-5148, 2003.

[77] A. Duparré, J. Ferre-Borrull, S. Gliech, G. Notni, J. Steinert, and J. M. Bennett, "Surface Characterization Techniques for Determining the Root-Mean-Square Roughness and Power Spectral Densities of Optical Components," *Appl. Opt.,* vol. 41, pp. 154-171, 2002.

[78] R. St-Gelais, T. Kerrien, A. Poulin, and Y.-A. Peter, "In-plane MEMS tunable Gires-Tournois interferometers," in *Conference on Lasers and Electro-Optics (CLEO) and Quantum Electronics and Laser Science (QELS)*, San Jose, 2010, p. CTuW2.

[79] R. St-Gelais, G. Mackey, J. Saunders, J. Zhou, A. Leblanc-Hotte, A. Poulin, J. A. Barnes, H.-P. Loock, R. S. Brown, and Y.-A. Peter, "Gas sensing using polymer-functionalized deformable Fabry-Perot interferometers," *Sensor Actuat. B-Chem.,* 2012 (submitted).

[80] M. D. Abramoff, P. J. Magelhaes, and S. J. Ram, "Image Processing with ImageJ," *Biophotonics International,* vol. 11, pp. 36-42, 2004.

[81] J. Masson, F. Koné, and Y.-A. Peter, "MEMS tunable silicon Fabry-Perot cavity," in *Proceedings of SPIE*, 2007, p. 671705.

[82] I. M. White and X. Fan, "On the performance quantification of resonant refractive index sensors," *Optics Express,* vol. 16, p. 1020, 2008.

[83] A. Llobera, R. Wilke, and S. Buttgenbach, "Poly(dimethylsiloxane) hollow Abbe prism with microlenses for detection based on absorption and refractive index shift," *Lab Chip,* vol. 4, pp. 24-27, 2004.

[84] X. J. Liang, A. Q. Liu, C. S. Lim, T. C. Ayi, and P. H. Yap, "Determining refractive index of single living cell using an integrated microchip," *Sensors and Actuators A: Physical,* vol. 133, pp. 349-354, 2007.

[85] P. Domachuk, I. C. M. Littler, M. Cronin-Golomb, and B. J. Eggleton, "Compact resonant integrated microfluidic refractometer," *Appl. Phys. Lett.,* vol. 88, p. 093513, 2006.

[86] W. Z. Song, X. M. Zhang, A. Q. Liu, C. S. Lim, P. H. Yap, and H. M. M. Hosseini, "Refractive index measurement of single living cells using on-chip Fabry-Pérot cavity," *Applied Physics Letters,* vol. 89, 2006.

[87] L. K. Chin, A. Q. Liu, C. S. Lim, X. M. Zhang, J. H. Ng, J. Z. Hao, and S. Takahashi, "Differential single living cell refractometry using grating resonant cavity with optical trap," *Applied Physics Letters,* vol. 91, p. 243901, 2007.

[88] H. Shao, W. Wang, S. E. Lana, and K. L. Lear, "Optofluidic Intracavity Spectroscopy of Canine Lymphoma and Lymphocytes," *Photonics Technology Letters, IEEE,* vol. 20, pp. 493-495, 2008.

[89] E. Chow, A. Grot, L. W. Mirkarimi, M. Sigalas, and G. Girolami, "Ultracompact biochemical sensor built with two-dimensional photoniccrystal microcavity," *Opt. Lett.,* vol. 29, pp. 1093-1095, 2004.

[90] I. M. White, H. Zhu, J. D. Suter, N. M. Hanumegowda, H. Oveys, M. Zourob, and X. Fan, "Refractometric Sensors for Lab-on-a-Chip Based on Optical Ring Resonators," *IEEE Sens. J. ,* vol. 7, pp. 28-35, 2007.

[91] J. C. T. Eijkel, "Chip-based HPLC: the quest for the perfect column," *Lab Chip,* vol. 7, pp. 815-817, 2007.

[92] J. N. Lee, C. Park, and G. M. Whitesides, "Solvent Compatibility of Poly(dimethylsiloxane)-Based Microfluidic Devices," *Anal. Chem.,* vol. 75, pp. 6544-6554, 2003/12/01 2003.

[93] X. Liu, X. Zhang, J. Cong, J. Xu, and K. Chen, "Demonstration of etched cladding fiber Bragg grating-based sensors with hydrogel coating," *Sensor Actuat. B-Chem.,* vol. 96, pp. 468-472, 2003.

[94] R. M. López, V. V. Spirin, M. G. Shlyagin, S. V. Miridonov, G. Beltrán, E. A. Kuzin, and A. Márquez Lucero, "Coherent optical frequency domain reflectometry for interrogation of bend-based fiber optic hydrocarbon sensors," *Opt. Fiber Technol.,* vol. 10, pp. 79-90, 2004.

[95] T. L. Yeo, T. Sun, K. T. V. Grattan, D. Parry, R. Lade, and B. D. Powell, "Characterisation of a polymer-coated fibre Bragg grating sensor for relative humidity sensing," *Sensor Actuat. B-Chem.,* vol. 110, pp. 148-156, 2005.

[96] A. Convertino, A. Capobianchi, A. Valentini, and E. N. M. Cirillo, "A New Approach to Organic Solvent Detection: High-Reflectivity Bragg Reflectors Based on a Gold Nanoparticle/Teflon-like Composite Material," *Adv. Mater.,* vol. 15, pp. 1103-1105, 2003.

[97] Y. Kang, J. J. Walish, T. Gorishnyy, and E. L. Thomas, "Broad-wavelength-range chemically tunable block-copolymer photonic gels," *Nat. Mater.,* vol. 6, pp. 957-960, 2007.

[98] J. L. Martínez-Hurtado, C. A. B. Davidson, J. Blyth, and C. R. Lowe, "Holographic Detection of Hydrocarbon Gases and Other Volatile Organic Compounds," *Langmuir,* vol. 26, pp. 15694-15699, 2010/10/05 2010.

[99] G. Gauglitz, A. Brecht, G. Kraus, and W. Mahm, "Chemical and biochemical sensors based on interferometry at thin (multi-) layers," *Sensor Actuat. B-Chem.,* vol. 11, pp. 21-27, 1993.

[100] C. Martínez-Hipatl, S. Muñoz-Aguirre, G. Beltrán-Pérez, J. Castillo-Mixcóatl, and J. Rivera-De la Rosa, "Detection of volatile organic compounds by an interferometric sensor," *Sensor Actuat. B-Chem.,* vol. 147, pp. 37-42, 2010.

[101] K. Reddy, Y. Guo, J. Liu, W. Lee, M. K. Khaing Oo, and X. Fan, "Rapid, sensitive, and multiplexed on-chip optical sensors for micro-gas chromatography," *Lab Chip,* vol. 12, pp. 901-905, 2012.

[102] F. R. Aussenegg, H. Brunner, A. Leitner, C. Lobmaier, T. Schalkhammer, and F. Pittner, "The metal island coated swelling polymer over mirror system (MICSPOMS): a new

principle for measuring ionic strength," *Sensor Actuat. B-Chem.,* vol. 29, pp. 204-209, 1995.

[103] R. St-Gelais, A. Poulin, and Y.-A. Peter, "Advances in modeling, design, and fabrication of deep-etched multilayer resonators," *Journal of Lightwave Technology,* vol. 30, pp. 1900-1908, 2012.

[104] J. Barnes, M. Dreher, K. Plett, R. S. Brown, C. M. Crudden, and H.-P. Loock, "Chemical sensor based on a long-period fibre grating modified by a functionalized polydimethylsiloxane coating," *Analyst,* vol. 133, pp. 1541-1549, 2008.

[105] T. M. Aminabhavi, "Use of mixing rules in the analysis of data for binary liquid mixtures," *J. Chem. Eng. Data,* vol. 29, pp. 54-55, 1984/01/01 1984.

[106] P. Brocos, A. Pineiro, R. Bravo, and A. Amigo, "Refractive indices, molar volumes and molar refractions of binary liquid mixtures: concepts and correlations," *Phys. Chem. Chem. Phys.,* vol. 5, pp. 550-557, 2003.

[107] J. E. Mark, *Polymer data handbook*: Oxford University Press New York, 1999.

[108] F. Schneider, T. Fellner, J. Wilde, and U. Wallrabe, "Mechanical properties of silicones for MEMS," *J. Micromech. Microeng.,* vol. 18, p. 065008, 2008.

[109] J. A. Barnes, R. S. Brown, A. H. Cheung, M. A. Dreher, G. Mackey, and H.-P. Loock, "Chemical sensing using a polymer coated long-period fiber grating interrogated by ring-down spectroscopy," *Sensor Actuat. B-Chem.,* vol. 148, pp. 221-226, 2010.

[110] P. A. Martos, A. Saraullo, and J. Pawliszyn, "Estimation of Air/Coating Distribution Coefficients for Solid Phase Microextraction Using Retention Indexes from Linear Temperature-Programmed Capillary Gas Chromatography. Application to the Sampling and Analysis of Total Petroleum Hydrocarbons in Air," *Anal. Chem.,* vol. 69, pp. 402-408, 1997/02/01 1997.

[111] Y. Guan, J. Kiraly, and J. A. Rijks, "Interactive retention index database for compound identification in temperature-programmed capillary gas chromatography," *J. Chromatogr.,* vol. 472, pp. 129-143, 1989.

[112] İ. Yilgör and J. McGrath, "Polysiloxane containing copolymers: A survey of recent developments," in *Advances in Polymer Science*. vol. 86, ed: Springer Berlin / Heidelberg, 1988, pp. 1-87.

[113] J.-C. Huang, "Probe dependency of segmental interaction parameters in copolymers by inverse gas chromatography," *J. of Appl. Polym. Sci.,* vol. 119, pp. 719-725, 2011.

[114] D. Lange, C. Hagleitner, A. Hierlemann, O. Brand, and H. Baltes, "Complementary Metal Oxide Semiconductor Cantilever Arrays on a Single Chip: Mass-Sensitive Detection of Volatile Organic Compounds," *Anal. Chem.,* vol. 74, pp. 3084-3095, 2002/07/01 2002.

[115] K. Arshak, E. Moore, G. M. Lyons, J. Harris, and S. Clifford, "A review of gas sensors employed in electronic nose applications," *Sensor Rev.,* vol. 24, pp. 181-198, 2004.

[116] A. Wilson and M. Baietto, "Applications and Advances in Electronic-Nose Technologies," *Sensors,* vol. 9, pp. 5099-5148, 2009.

[117] A. Mirmohseni and V. Hassanzadeh, "Application of polymer-coated quartz crystal microbalance (QCM) as a sensor for BTEX compounds vapors," *J. of Appl. Polym. Sci.,* vol. 79, pp. 1062-1066, 2001.

[118] N. Barié, M. Rapp, and H. J. Ache, "UV crosslinked polysiloxanes as new coating materials for SAW devices with high long-term stability," *Sensor Actuat. B-Chem.,* vol. 46, pp. 97-103, 1998.

[119] D. J. Moss, M. Lamont, S. McLaughlin, G. Randall, P. Colbourne, S. Kiran, and C. A. Hulse, "Tunable dispersion and dispersion slope compensators for 10 Gb/s using all-pass multicavity etalons," *IEEE Photonics Technol. Lett.,* vol. 15, pp. 730-732, 2003.

[120] S. Doucet, R. Slavik, and S. LaRochelle, "Tunable dispersion and dispersion slope compensator using novel Gires-Tournois Bragg grating coupled-cavities," *IEEE Photonics Technol. Lett.,* vol. 16, pp. 2529-2531, 2004.

[121] S. Cao, C. Lin, C. Yang, E. Ning, J. Zhao, and G. Barbarossa, "Birefringent Gires-Tournois interferometer (BGTI) for DWDM interleaving," in *Optical Fiber Communication Conference*, Anaheim, CA, 2002, pp. 395-396.

[122] W.-Z. Li, Q.-D. Guo, and S. Gu, "Interleaver technology review," in *Proc. SPIE*, 2002, pp. 73-79.

[123] H. Chao-Hsing, W. Ruibo, Z. J. Wen, I. McMichael, P. Yeh, L. Chao-Wei, and C. Wood-Hi, "Flat-top interleavers using two Gires-Tournois etalons as phase-dispersive mirrors in a Michelson interferometer," *IEEE Photonics Technol. Lett.,* vol. 15, pp. 242-244, 2003.

[124] X. Shu, K. Sugden, and I. Bennion, "Novel multipassband optical filter using all-fiber Michelson-Gires-Tournois structure," *IEEE Photonics Technol. Lett.,* vol. 17, pp. 384-386, 2005.

[125] K. Yu and O. Solgaard, "Tunable optical transversal filters based on a Gires-Tournois interferometer with MEMS phase shifters," *IEEE J. Sel. Top. Quantum Electron.,* vol. 10, pp. 588-597, 2004.

[126] W. Zhou, X. Dong, L.-Y. Shao, C. C. Chan, C.-L. Zhao, and P. Shum, "Compact refractometer based on extrinsic-phase-shift fiber Bragg grating," *Sensors and Actuators A: Physical,* vol. 168, pp. 46-50, 2011.

[127] P. Liu, H. Huang, T. Cao, Z. Tang, X. Liu, Z. Qi, M. Ren, and H. Wu, "An optofluidics biosensor consisted of high-finesse Fabry-Perot resonator and micro-fluidic channel," *Applied Physics Letters,* vol. 100, pp. 233705-233705-4, 2012.

[128] H. Hunt and J. Wilkinson, "Optofluidic integration for microanalysis," *Microfluidics and Nanofluidics,* vol. 4, pp. 53-79, 2008.

[129] X. Fan and I. M. White, "Optofluidic microsystems for chemical and biological analysis," *Nature photonics,* vol. 5, pp. 591-597, 2011.

[130] J. Homola, S. S. Yee, and G. Gauglitz, "Surface plasmon resonance sensors: review," *Sensors and Actuators B: Chemical,* vol. 54, pp. 3-15, 1999.

[131] H. M. Shapiro and R. C. Leif, *Practical flow cytometry*: Wiley Online Library, 2003.

[132] A. Leblanc-Hotte, R. St-Gelais, and Y.-A. Peter, "Optofluidic Device for High Resolution Volume Refractivce Index Measurement of Single Cell," in *16th International Conference on Miniaturized Systems for Chemistry and Life Science* Okinawa, Japan 2012, pp. 1330-1332.

[133] D. Then, A. Vidic, and C. Ziegler, "A highly sensitive self-oscillating cantilever array for the quantitative and qualitative analysis of organic vapor mixtures," *Sensor Actuat. B-Chem.,* vol. 117, pp. 1-9, 2006.

ANNEX 1 – List of scientific contributions

Refereed journals

- A. Poulin, **R. St-Gelais**, A. L. Eichenberger, L. Thévenas, and Y.-A. Peter, "MEMS tunable asymmetric Fabry-Perot cavity for high precision weighing of macro samples," *J. Microelectromech. Syst.,* 2012 (in revision)

- **R. St-Gelais**, T. Kerrien, H. Camirand, A. Poulin, and Y.-A. Peter, "Silicon-on-insulator in-plane Gires-Tournois interferometers," *IEEE Photonics Technol. Lett.,* vol. 24, pp. 2272-2275, 2012

- **R. St-Gelais**, G. Mackey, J. Saunders, J. Zhou, A. Leblanc-Hotte, A. Poulin, J. A. Barnes, H.-P. Loock, R. S. Brown, and Y.-A. Peter, "Gas sensing using polymer-functionalized deformable Fabry-Perot interferometers," *Sensor Actuat. B-Chem,* 2012 (in revision).

- **R. St-Gelais**, A. Poulin, and Y.-A. Peter, "Advances in modeling, design, and fabrication of deep-etched multilayer resonators," *Journal of Lightwave Technology,* vol. 30, pp. 1900-1908, 2012

- J. Masson, **R. St-Gelais**, A. Poulin and Y-.A. Peter, "Tunable Fiber Laser Using a MEMS-Based in-plane Fabry-Pérot Filter", *IEEE Journal of Quantum Electronics,* vol. 46, no. 9, pp. 1313-1319, 2010

- **R. St-Gelais**, J. Masson, and Y.-A. Peter, "All-silicon integrated Fabry–Pérot cavity for volume refractive index measurement in microfluidic systems," *Applied Physics Letters*, vol. 94, p. 243905, 2009
  (Selected paper in *Virtual Journal of Biological Physics Research,* vol. 18, no. 1, 2009)

Refereed conferences

- A. Leblanc-Hotte[†], **R. St-Gelais**, and Y.-A. Peter, "Optofluidic device for high resolution volume refractive index measurement of single cell", *International Conference on Miniaturized Systems for Chemistry and Life Sciences (MicroTAS)*, Okinawa, Japan, pp. 1330-1332, 2012

- A. Poulin[†], **R. St-Gelais**, N. Goulamhoussen, G. Zhu, C. Boudoux and Y.-A. Peter, "In-plane MEMS-based Fabry-Perot filter for high-speed wavelength-swept semiconductor laser," in *Hilton Head solid-state sensors, Actuators and Microsystems Workshop*, SC, USA, pp. 401-404, 2012

- A. Poulin[†], **R. St-Gelais**, and Y.-A. Peter, “Coupled electro-mechanical transducers for vertical to horizontal motion translation,” in *Symposium on Design, Test, Integration and Packaging of MEMS/MOEMS*, Cannes, France, pp. 240-243, 2012.

- **R. St-Gelais***, G. Mackey, J. Saunders, J. Zhou, A. Leblanc-Hotte, A. Poulin, J.A. Barnes, H.-P. Loock, R. S. Brown, Y.-A. Peter, "A Fabry-Perot refractometer for chemical vapor sensing by solid-phase microextraction", *International Conference on Optical MEMS & Nanophotonics*, Istanbul, Turkey, pp. 85-86, 2011

- **R. St-Gelais*,** G. Mackey, J. Saunders, J. Zhou, A. Leblanc-Hotte, J.A. Barnes, H.-P. Loock, Y.-A. Peter, R. S. Brown, "Functionalized silicon Fabry-Perot microcavities for chemical vapor sensing", *User Meeting and Summer School on cavity enhanced spectroscopy*, Kingston, Canada, p. 19, 2011

- **R. St-Gelais***, T. Kerrien, A. Poulin and Y.-A. Peter, “In-plane MEMS tunable Gires-Tournois Interferometers”, *CLEO/QELS Laser Science to Photonic Applications,* San Jose, CA, CTuW2, 2010

- **R. St-Gelais***, T. Kerrien, A. Poulin and Y.-A. Peter, “Interféromètre de Gires-Tournois accordable sur Silicim”, *78e congrès de l'ACFAS, Colloque Optique Guidée et Photonique IX,* Montréal, Canada, 2010

- **R. St-Gelais**[†], J. Masson, and Y.-A. Peter, “High resolution microfluidic refractometer for biomedical applications,” *The 5th International Conference on Microtechnologies in Medecine and Biology*, Quebec, Canada, W3P.14, 2009

- **R. St-Gelais***, J. Masson, and Y.-A. Peter, “High resolution integrated microfluidic Fabry-Perot refractometer in silicon,” *IEEE/LEOS International Conference on Optical MEMS and Nanophotonics*, Freiburg, Germany, pp. 17-18, 2008.

*Oral presentation, [†]Poster presentation

Patents

- Y.-A. Peter and **R. St-Gelais**, “Deformable interferometric sensor”, US Patent application n. 61/734,634 (2012)

- Y.-A. Peter, J. Masson, and **R. St-Gelais**, “MEMS tunable silicon fabry-perot cavity and applications thereof”, US Patent 8,174,698 B2, 2012.